Rain Attenuation and Depolarization Along 10 to 30 GHz Earth Space Links Predicted From S-Band Dual-Polarized Radar Measurements

by

Michael Allan Starr

Thesis submitted to the Faculty of the

Virginia Polytechnic Institute and State University

in partial fulfillment of the requirements for the degree of

Master of Science

in

Electrical Engineering

APPROVED:

Warren L. Stutzman, Chairman

Charles W. Bostian

Timothy Pratt

November 1986

Blacksburg, Virginia

Rain Attenuation and Depolarization Along 10 to 30 GHz Earth Space Links Predicted From S-Band Dual-Polarized Radar Measurements

by

Michael Allan Starr

Warren L. Stutzman, Chairman

Electrical Engineering

(ABSTRACT)

This thesis presents the computer model FORWP that is capable of predicting attenuation and cross polarization at 10-30 GHz from dual-polarization radar data with a high degree of accuracy. FORWP uses a rigorous backscattering computer model BSCAT to infer rain drop size distribution along the slant path from radar measured reflectivity and differential reflectivity data collected along the path.

Then, two semi-empirical models are developed which predict attenuation from radar measured reflectivity and differential reflectivity. These two semi-empirical models are used to evaluate FORWP.

Finally, attenuation predictions of FORWP are compared to the two semi-empirical prediction models and measured link attenuation at 11.4 GHz for a rain event in southwest Virginia.

Acknowledgements

I would like to express my deep appreciation to my thesis chairman, Dr. Warren L. Stutzman who not only provided immeasurable help in completing my Master of Science but also taught me indispensable principles of life. Thank are also due to Dr. Tim Pratt for his help and encouragement, and to Dr. Charles W. Bostian for guiding me through the completion of my thesis.

Many thanks are also due Wendy Maroney for her skill and help as typist. I would also like to thank Dennis Sweeney, Claudia Stutzman, Robert Porter, Kathyrn Wood, and Kimberley Leach for sharing the experience of graduate school and for the friendships gained during that time.

A special thanks to my fiancee, Karen Laroie, for understanding and always being an encouragement.

Also, I must thank the Lord for His abundant love and grace.

Table of Contents

Chapter 1 Review of Research Effort

1.0 Review of Research Effort

1.1 Introduction

The first major commercial satellite systems began with the INTELSAT series in 1965, operating on a 6 GHz uplink frequency and a 4 GHz downlink frequency. Since then satellites have become an increasingly attractive communication medium. This increase is due in part to the ability of satellites to interconnect a large number of user terminals separated by large distances. The viability of satellites has prompted applications beyond the traditional voice and TV uses, such as electronic mail, electronic fund transfer, computer interconnections, video teleconferencing, and even mobile services.

The demand for a greater number of satellite communication systems has promoted the development and use of satellite systems in the higher frequency bands of 12-14 GHz and 20-30 GHz. The major incentive for using these higher frequencies is the spectrum crowding that exists in the frequencies below 8 GHz. Also, higher frequencies offer larger bandwidths

and therefore more information capacity. For example, the bandwidth allocated in the 4-6 GHz and 7-8 GHz bands is 500 MHz, while the bandwidth allocated at the 20-30 GHz band is 3.5 GHz. The higher frequency bands also make possible the reduction in size and weight of satellite and earth terminal hardware. The higher frequency bands not only provide relief from congestion in the lower frequency spectrum, but they also serve to alleviate the problem of crowding in the geosynchronous orbit. Satellites operating at higher frequencies can be placed in relatively close proximity to lower frequency satellites without signal interference.

The increased use and development of satellite systems in the 12-14 GHz and 20-30 GHz bands has been hampered by the relatively large rain attenuation at these frequencies. Satellite system designers can compensate for rain attenuation by transmitting at higher signal levels and using larger dynamic range receivers. To implement these system changes, the satellite designer must often increase the size , weight and complexity of the satellite which can significantly increase cost. Therefore to minimize cost, the system designer needs an accurate assessment of attenuation to determine the lowest acceptable gain margin.

A variety of methods are presently used to estimate rain attenuation including: direct link attenuation measurements, theoretical and empirical prediction models that use both annual and link measurement statistics, and weather radar measurements. The direct measurement of link attenuation is somewhat limited in its usefulness. Even though a large data base of link measurements exists, it is not sufficient to provide link measurements for all possible earth station locations, frequencies, and elevation angles. Numerous models exist which estimate attenuation statistics from annual rain rate statistics. Two such models were developed by Dishman and Stutzman [1982] and Runyon and Stutzman [1983]. These models have the flexibility of accounting for frequency, elevation angle, and to some extent earth station location, but they can not account for the particular micro-climate of all intended earth station locations. Therefore, these models lack the accuracy sought by many satellite system designers.

However, accurate attenuation predictions can be made using weather radars. These predictions can be made prior to the design of an intended satellite link for a variety of earth

station locations, slant path orientations, and frequencies. Also, the weather radar can assess the link performance for a variety of proposed satellite link paths within its scanning range. The flexibility and the potential accuracy of weather radar makes it a very attractive tool for predicting link attenuation.

The original contribution of this work is the development and analysis of the FORWP prediction model capable of predicting attenuation (A) and cross polarization discrimination (XPD) at 10-30 GHz from dual-polarized radar data with a high degree of accuracy.

FORWP is composed of two sub-programs, BSCAT and MULTI. BSCAT was derived from backscattering theory developed by Stapor and Pratt [1982] and is used by FORWP to infer the rain drop size distribution (DSD) along the earth space communication path from radar measured horizontal reflectivity (Z_H) and differential reflectivity (ZDR). This drop size distribution information is then applied to a rigorous forward multiple scattering model (MULTI) that predicts attenuation and cross polarization. The forward multiple scattering theory incorporated into MULTI was developed by Tsolakis and Stutzman [1982].

This report also briefly discusses the INTELSAT experiment for which the FORWP prediction model was developed. The experiment was conducted for one year and primarily involved the use of the INTELSAT V satellite 11.4 GHz beacon with two earth terminals and the VPI & SU 2.8 GHz Octopod radar. The experiment uses the computer model FORWP to predict link attenuation and cross polarization from radar data. These predicted attenuation and cross polarization values are amassed into a data base and compared with measure link data over a year.

The report also reviews the backscattering and multiple scattering theory used in the computer models BSCAT and MULTI and the methods used to incorporate BSCAT and MULTI into FORWP.

Next this work develops two semi-empirical prediction models and uses them to assess FORWP. Then a study of the parameters used by FORWP is conducted. Finally FORWP and the two semi-empirical models are compared with measured link attenuation values.

1.2 Explanation of Experiment

INTELSAT in 1984 awarded a contract (number INTEL-433) to the Satellite Communications Group at Virginia Polytechnic Institute and State University for a two year propagation experiment. In the first year of the contract, the experiment was designed and built. Through the second year, the experiment was operated nearly 24 hours a day and a data base of measured and radar predicted attenuation values was amassed.

1.2.1 System Configuration

In this work, we review the INTELSAT experiment, emphasizing the aspects of the experiment which relate to the FORWP prediction model. We discuss briefly the hardware configuration, data collection, data processing, and data analysis. A more detailed description of the experiment hardware is provided by Sweeney [1986]. Additional information on the data processing and data analysis is given by the "Processing Analysis Plan for the INTELSAT Contract" INTEL-433 [May 1985].

Figure 1.2.1-1 is an overview of the experiment's configuration. The two earth station terminals indicated in Figure 1.1 measure attenuation and cross polarization at 11.452 GHz along two slant paths from the INTELSAT V beacon (elevation angle $\varepsilon = 18.5°$). The local (01) receiving earth station terminal is located at the Virginia Tech Satellite Tracking Station. The diversity (02) receiving earth station is located at a site 7.3 km from the local receiving terminal site. The VPI & SU Octopod radar is located at the Tracking Station, alongside the local receiving terminal site. The Tracking Station equipment also includes a temperature probe, three rain gauges, a barometer, a wind gauge, an S-100 data collection computer, and an X-band surveillance radar. The diversity site incorporates, in addition to the receiving

terminal, a temperature probe, two rain gauges and a distrometer. A telephone line modem data link connects the two sites.

1.2.2 Hardware Operation

During the operation of the experiment, an S-100 computer at the local site collects data from the 01 and 02 link receivers, the radar, the distrometer, the rain gauges, and the temperature probes. The S-100 then stores these data on the raw data tapes. Later a Harris 800E computer reads, processes and analyzes the data on the tape using the FORWP computer program to predict attenuation and cross polarization. The Harris 800E then uses the statistical analysis program to generate exceedance statistics and scatter plots.

The experimental set up is fairly complex containing a network of five computers that interface with several complex hardware items. In addition, thousands of man hours were required to develop the software for the various computers.

The major pieces of hardware developed for the experiment are the Octopod radar, the radar antenna positioning system, the radar data acquisition system (DAS), the X-band surveillance radar, and the earth station receiving terminals.

1.2.2.1 Octopod Radar

The Octopod radar is an eight polarization, S-band, pulsed, non-coherent system. The frequency of operation is 2.8 GHz and the transmitter output power is 250 kW (peak). The pulse width is approximately 800 ns and the antenna beamwidth is about 2.4 degrees. The radar operates with eight equally spaced linear polarizations.

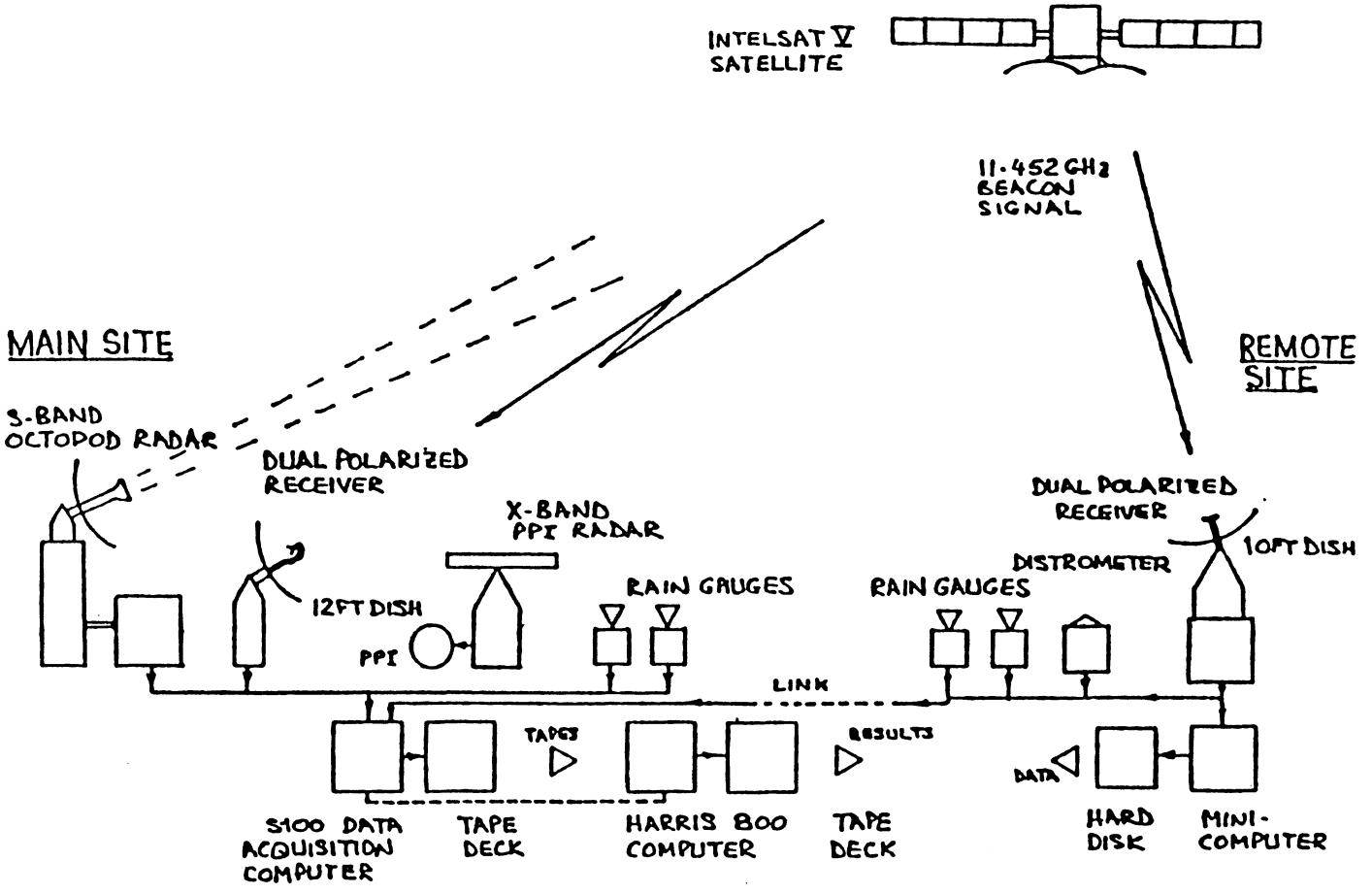

Figure 1.2.1-1 System Configuration of Experiment

1.2.2.2 Data Acquisition System

The Antenna Positioning System uses a velocity feedback control loop to position the antenna. This control system uses 1:1 and 36:1 synchros on both axes of the antenna pedestal to provide pointing information. D.C. motors drive each axis of the antenna pedestal. Amplidynes, controlled by position velocity control systems, power the two D. C. axis drive motors.

Through the use of synchro-to-digital converters the antenna pointing is controlled by an IBM-PC. This microcomputer controls the scanning sequence of the antenna and also passes position and timing information to the S-100 computer.

The Data Acquisition System (DAS) digitizes and averages the radar data before it is collected by the S-100 computer. The DAS also controls the radar transmit and receive timing. The radar timing for a given polarization starts with the radar transmitting a 250 kW (peak), 800 ns pulse. Then approximately every 1.6 μs after the transmit pulse, for a total of about 200 μs, the DAS samples the received signal. The signal is collected by the radar antenna configured in the same polarization as the transmitted pulse. Each 1.6 μs receiver sample provides information for consecutive 255 m range gates along the axis of the radar antenna beam. The radar probes the spatial volume within its antenna beam by transmitting sequentially on all eight linear polarizations in a 16.7 ms period. After each transmission, 127 range gate samples are collected for that particular polarization. The transmit and receive sequence is repeated 64 times at all eight polarization. This provides a set of 64 receiver samples of each range gate in each polarization. The DAS then averages each set of 64 receiver samples to provide an averaged radar reflectivity value for every range gate in each polarization. It should be noted, that for most of the work performed in the experiment, only the vertical and horizontal radar data was used. These two polarizations provide Z_H and ZDR data values (see Section 2.5).

The DAS is composed of two main units: the Radar Interface Unit (RIU) and the DAS Controller. The RIU is a specialized digital processing unit built primarily from VLSI and LSI

integrated chips. The RIU samples, digitizes, and averages the radar receiver signal. It also generates the timing signal to control the radar transmitter. The DAS Controller is composed of primarily a Standard-Bus Z-80 based microcomputer. Custom logic boards are used to interface the Standard-Bus computer with the RIU and the S-100 computer. The DAS Controller also interfaces the RIU and the radar antenna controller with the S-100 computer.

1.2.2.3 X-Band Surveillance Radar

The X-band surveillance radar contains a large PPI display that indicates precipitation activity within a 25-50 mile range of the two link receiving terminals. Since radar data are only collected when rain is threatening to cross either of the two slant paths, the X-band radar is used to determine when to collect radar data.

1.2.2.4 Earth Station Receivers

There are a total of three earth station receivers used in the experiment. Two of the receivers are located at the local site with one of the two acting as a back-up system. The third receiver is located at the diversity site. The receivers continuously measure the A and XPD of the two satellite links. The output of the receivers are digitized, sampled, and collected by computers.

1.2.3 Radar Antenna Scanning

During the operation of the experiment, the radar antenna probes two satellite link paths (01 and 02), makes two range height scans (RH1 and RH2), and observes a space volume above the distrometer at the diversity site. Figure 1.2.3-1 illustrates the antenna scanning

configuration used for the various paths. This figure shows the first range height scans (RHI-1) along the 01 path and the second range height scans over the 02 earth station. Table 1.2.3-1 summarizes the sequence of the scanning process and provides the following information for each section of the scan: the scanning time of each section, the name of each scanning section, the action of the antenna during each scanning section, and the number of radar probe samples (N) collected during each scanning section.

The scanning of the local path and the two range height paths is straightforward. For the local path scan, the antenna is fixed in position such that the axis of its beam nearly aligns with the local path. Therefore, the radar range gate samples produce consecutive data samples along the 01 path. During the range height scans, the antenna is fixed in azimuth and moved in elevation.

The radar probes the 02 path by moving the antenna in azimuth and elevation along the path. Figure 1.2.3-2 illustrates this scanning of the 02 path. The radar probes the path at consecutive range intervals along its slant length. Each range interval is determined from where consecutive 2.4° antenna beamwidths cross the slant path. Within the 2.4° antenna beamwidth used to scan each range interval along the 02 path, a group of between 1 and 29 range gates intersect the path (see Figure 1.2.3).

1.2.4 Data Collection, Processing and Analysis

The operational portion of the experiment is divided into the following three phases: data collection, data processing, and data analysis. Figure 1.2.4-1 summarizes these three phases.

The data collection phase involves the collection of link receiver data, radar data, and weather data by the S-100 data collection computer. The weather data includes data from the two temperature probes and the wind gauge. The S-100 stores this data on either the raw data tapes or the continuous data tapes. During times when no rain is in the slant paths, radar data is not collected, but the link receiver data and weather data is collected and stored on the

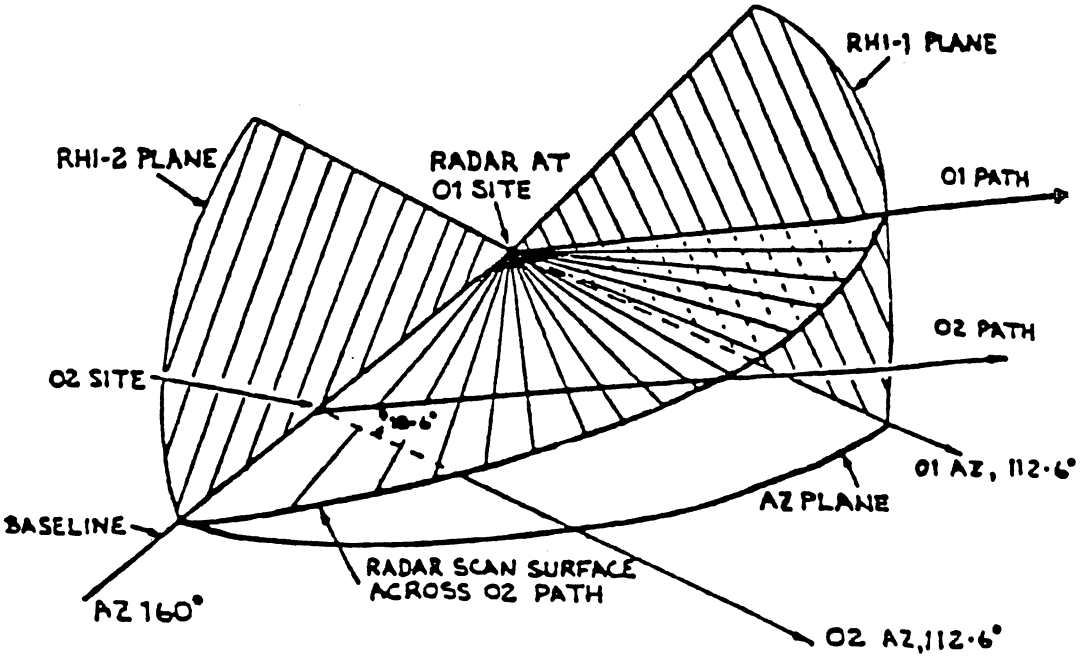

Figure 1.2.3-1. RHI and slant path scans.

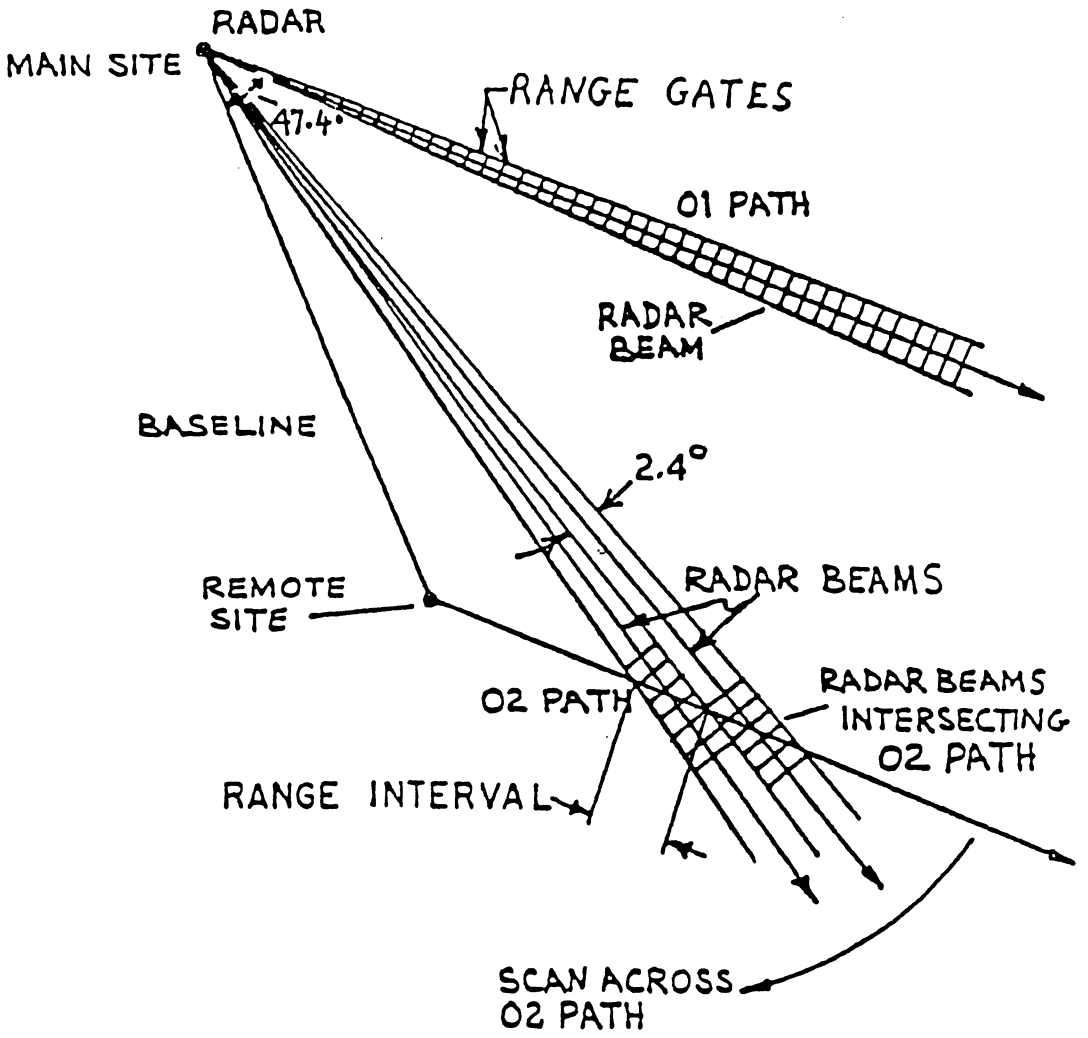

Figure 1.2.3-2. Illustration of radar scans along 01 and across 02 path.

Table 1.2.3-1 RADAR SCAN SEQUENCE

Time (seconds)	Code	Action	Bound on N
0-30	DIV	Stationary over diversity site at 1.2 degrees elevation angle.	<15
35-80	RHI2	RHI from 0 to 40 degrees at diversity site azimuth, 1.2 degrees/sec.	<25
80-85	RESET2	Reset antenna to 0 degrees elevation.	
85-125	SCAN1	Inclined plane scan across diversity site path to satellite at 1.2 degrees/sec.	<25
130-150	PATH1	Stationary on main site path to satellite, 18 degrees elevation angle.	<10
150-160	RESET1	Reset antenna to 0 degrees elevation.	
160-205	RHI1	RHI from 0 to 40 degrees at main site slant path azimuth at 1.2 degrees/sec.	<25
205-210	RESET3	Reset antenna to 18 degrees elevation angle.	
210-230	PATH2	Stationary on main site path to satellite, 18 degrees elevation angle.	<10
230-270	SCAN2	Inclined plane scan across diversity site path to satellite, at 1.2 degrees/sec.	<25

END OF SEQUENCE: REPEAT

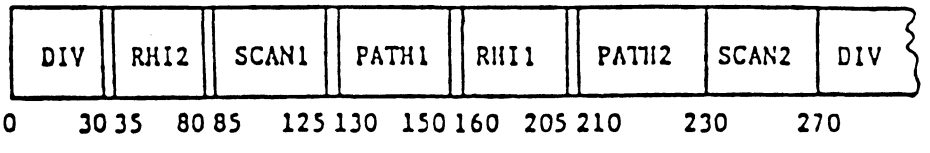

continuous data tapes. These tapes provide a base line calibration for clear weather conditions. When radar data is collected, the radar data, the link receiver data, and the weather data are stored on the raw data tapes.

The data processing phase is illustrated in Figure 1.2.4-1. The front end processor programs read the raw data tapes and sort radar data by type into temporary disk files. The pre-processor programs, using calibration data, then convert the data in the temporary files into usable values. The pre-processor programs also correlate the various data type by time and event. Next this data enters the FIRST LOOK program and is also stored on the archive data tapes.

The data analysis phase is divided into two major sub-phases: the pre-analysis, and statistical analysis. The pre-analysis phase reads the archive data tapes and generates comparative prediction files of measured and radar predicted attenuation and cross polarization values. These files are combined into a one year data base. Next, the statistical analysis program is used to generate attenuation exceedance statistics and scatter plots from the one year data base. A full description of the statistical analysis program is given in [INTELSAT Monthly Report, Contract INTEL-433, May 1985, Appendix I].

The pre-analysis phase is illustrated in Figure 1.2.4-2. This phase begins with the PATHGE program reading the archive tapes and sorting out the various data types: radar, distrometer; link receiver, and rain gauge. PATHGE then tests and adjust these various data types for out-of-bounds and missing data points. Finally, PATHGE program stores the data into the following temporary files: the diversity site file, the local path file, and diversity path file, the RH-1 File, the RH-2 File, and the link data file.

The diversity site file contains distrometer DSD data and radar measured Z_H and ZDR values from the volume over the distrometer. The data from the diversity site file will provide the basis for a comparative study between distrometer and radar derived Z_H , ZDR, and rain rate values. This study will guide the selection of various parameters in the FORWP prediction model (see Chapter 2).

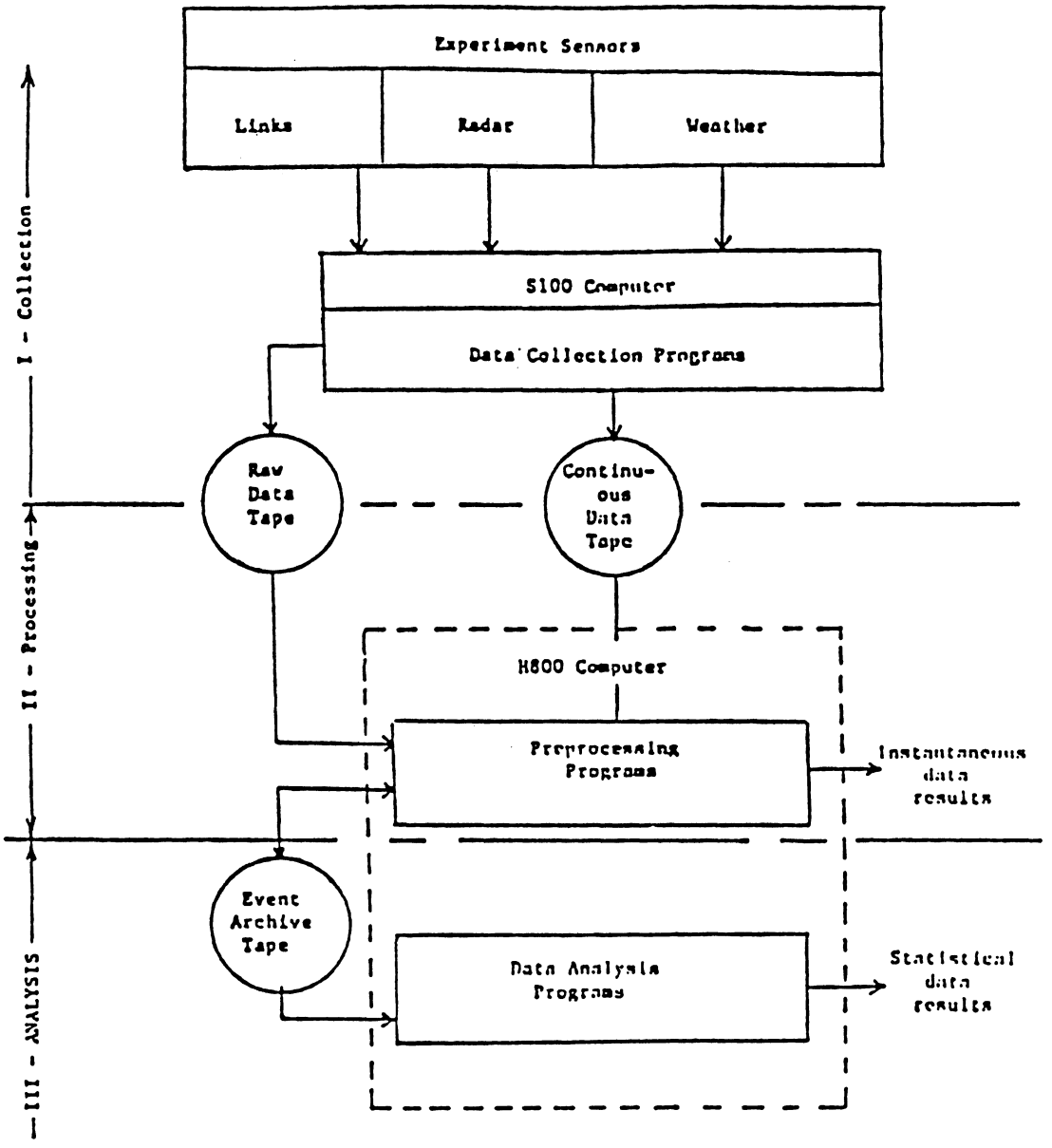

Figure 1.2.4-1. Data Collection, Data Processing, and Data Analysis

1.0 Review of Research Effort

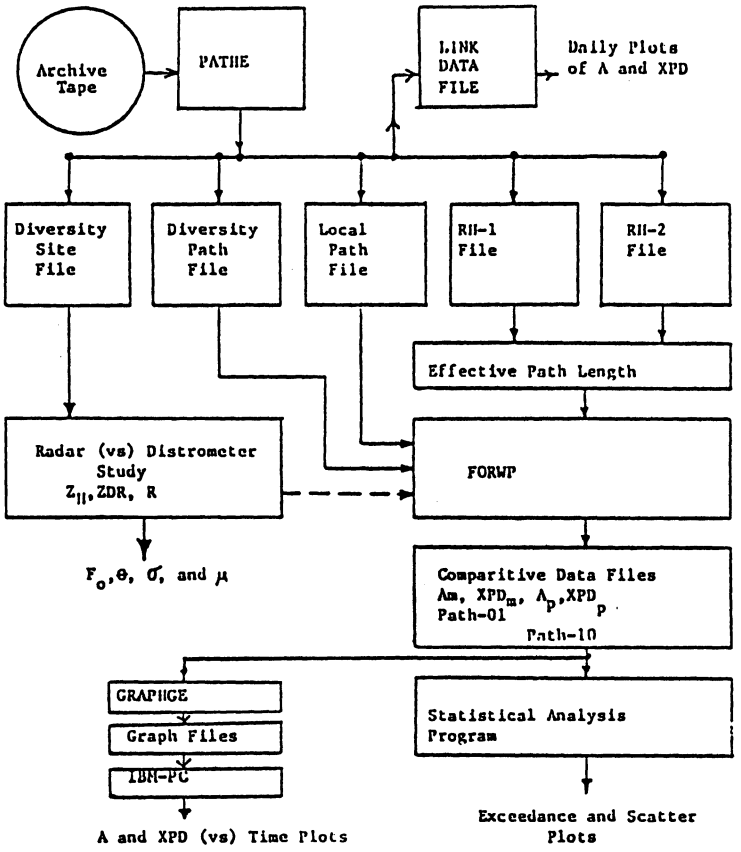

Figure 1.2.4-2 Block diagram of pre-analysis phase

The two range height files provide Z_H and ZDR profile information. These profiles are used to assess melting layer regions in the slant paths and determine the effective length of precipitation in the slant paths.

The local path file and the diversity path file contain link, rain rate and radar data associated with the two slant paths, and are processed by the FORWP prediction program.

The link data file contains the measured A and XPD values of the local and diversity site links. This file is used to generate daily plots of A and XPD as a function of time. The daily plots are used to determine when significant rain events have crossed the slant paths.

The GRAPHGE program in Figure 1.2.4-2 is used to generate plots of FORWP predicted attenuation and measured attenuation values for a given slant path type. GRAPHGE sorts the comparative data files into graph files suitable for plotting. Then these graph files are passed to an IBM-PC and plotted.

1.2.5 The FORWP Program

The FORWP program processes the data in the local path file and the diversity path file to calculate the radar-predicted A and XPD values for the two links. The FORWP program starts the prediction process by reading one of the path files (local or diversity).

The format of the local path file is shown in Table 1.2.5-1. The first line in the file contains the path type qualifier (LOC). The data lines following this first line are grouped into sequential data blocks of 33 lines. Each data block corresponds to the link and radar data collected during a complete radar probe (scan) of the path. The first line in each data block contains the date, time, link measured A and XPD values, and rain gauge measured rain rate. The following 32 data lines in the data block are arranged in 4 pairs of 2 columns representing the Z_H , ZDR data pair collected by the radar during the path probe (scan). From left to right and top to bottom these four columns of Z_H , ZDR pairs represent radar data samples collected up the slant path. The total number of data blocks in the Local Path File can vary from a few to

Table 1.2.5-1 An Example of the contents of the Local Path File

LOC							
01MAR85		00:00:00:0	8.47	14.32	8.46	14.32...	
125.02	0.895	25.02	0.895	25.02	0.895	25.02	0.895
525.02	0.895	25.02	0.895	25.02	0.895	25.02	0.895
925.02	0.895	25.02	0.895	25.02	0.895	25.02	0.895
.	.	.	.	.	.	.	.
.	.	.	.	.	.	.	.
.	.	.	.	.	.	.	.
12425.02	0.895	25.02	0.895	25.02	0.895	25.02	0.895
01MAR85		00:08:00:0	8.47	14.32	8.46	12.32...	
125.02	0.89	25.02	0.895	25.02	0.895	25.02	0.895
.	.	.	.	.	.	.	.
.	.	.	.	.	.	.	.
.	.	.	.	.	.	.	.
EOF							

thousands. All the data blocks in the file correspond to a single archive tape. An end-of-file (EOF) mark is used by FORWP to terminate file processing.

The format of the diversity path file is very similar to the local path file. The two major differences are the following: the name of the path type qualifier in line one is DIV instead of LOC, and the number of Z_H , ZDR radar data pairs is 90 instead of 127.

Figure 1.2.5-1 illustrates the logic flow of the FORWP program. FORWP starts by reading the first line of the selected path file (local or diversity) to determine its path type. With the path type known, FORWP sets four rain parameters, F_0, θ, σ, and μ , to pre-selected values. The selection and definitions of these four rain parameters are discussed in Chapter 2. After setting the rain parameters, FORWP calls the sub-program QSFGEN. This program uses the previous parameter settings and the backscattering program BSCAT to generate Λ_μ versus ZDR, Z_H N_μ versus Λ_μ and rain rate versus Λ_μ cubic-spline curve fits. The program BSCAT is discussed in Chapter 2 along with DSD parameters Λ_μ, N_μ, and μ. Next FORWP sets the length of each radar range interval in the path (local or diversity).

FORWP proceeds to process the radar data in the path file. Each data block in the path file will provide a predicted value for A and XPD. FORWP processes the path file until an end-of-file mark is reached.

The processing of a single data block by FORWP proceeds as follows. FORWP first reads and temporarily stores the first line in the data block. This line contains the time, radar data, measured A, measured XPD, and the measured rain rate. Next FORWP reads into two arrays the Z_H , ZDR radar data pairs contained in the data block. The Z_H array and the ZDR array are then tested and adjusted. Each Z_H , ZDR data pair is tested to see if it is a result of ground clutter. If Z_H is greater than 60 dBZ (mm^6m^{-3}) or ZDR is greater than 3.5 dB, then the radar data pair is assumed to be ground clutter and is replaced with the next data pair collected up the path. The ZDR value in each Z_H , ZDR data pair is then tested for reliability. If the value of ZDR is less than 0.5 dB (mm^6mm^{-3}), then the ZDR is considered unreliable and this ZDR value is replaced by an analytically derived value.

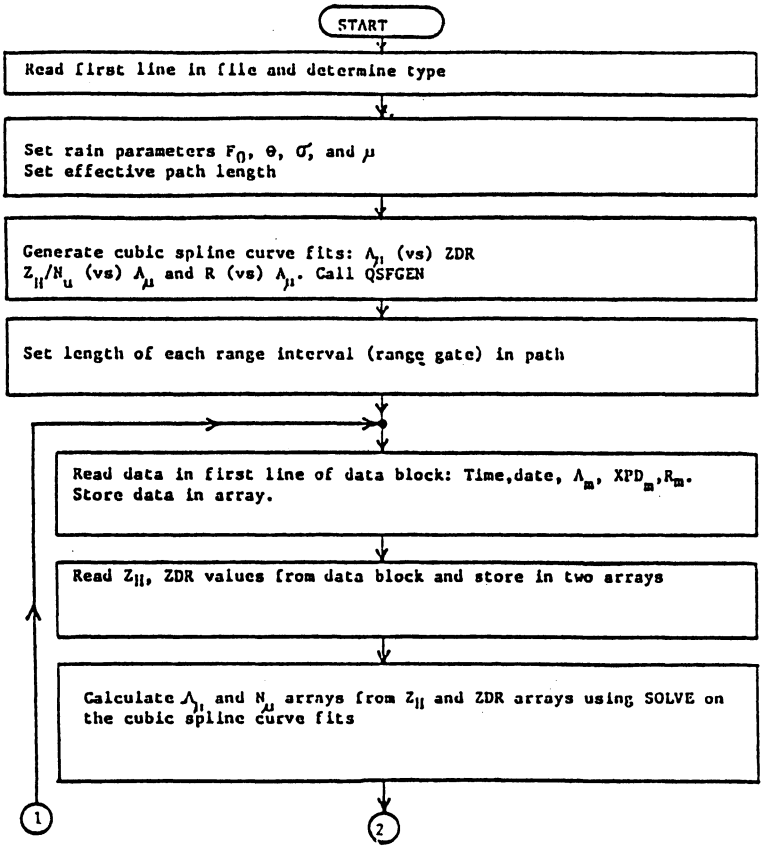

Figure 1.2.5-1. Flow Diagram of FORWP Program

1.0 Review of Research Effort

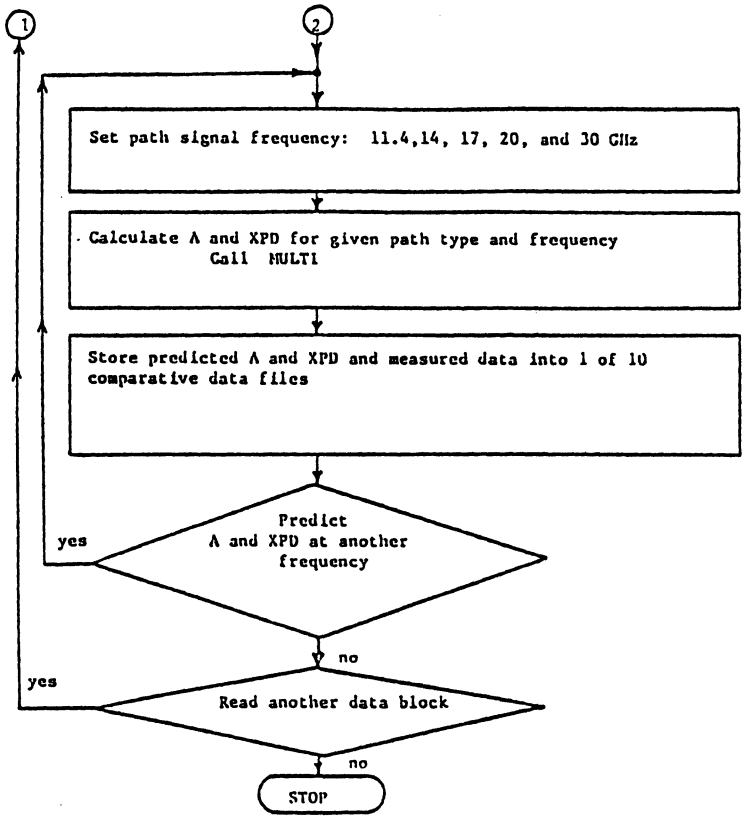

Figure 1.2.5-1 Flow diagram of FORWP program continued

With the radar data stored in arrays, FORWP then passes these arrays to the sub-program SOLVE. The sub-program calculates the N_μ, Λ_μ parameter pairs from Z_H , ZDR data pairs by solving the previously defined cubic-spline curve fits. From the Z_H array and the ZDR array, SOLVE produces a Λ_μ array and a N_μ array. The two DSD parameter arrays provide the information necessary to estimate the DSD along the slant path.

Next, FORWP passes the Λ_μ array and the N_μ array to the sub-program MULTI. This sub-program uses the DSD information in the Λ_μ and N_μ arrays to calculate the attenuation and cross-polarization of the path. FORWP also passes to MULTI the following data: the length of each path range interval, the effective length of the slant path, the frequency of the signal in the slant path, the rain parameters and the elevation angle of the path. Once MULTI predicts A and XPD, FORWP stores the predicted A and XPD values along with the data in the first line of the data block in a single line in a comparative data file. One data block in the path file (local or diversity) will produce one line in a comparative data file.

The comparative data file for the local path is PATH-01 and the comparative path file for the diversity path is PATH-02. Each line of these two files will contain predicted and measured data associated with a full radar probe (scan) of the path. The following data will be stored on each line of a comparative data file: data of rain event, mean time of path probe (scan), the link measured and XPD values, the rain gauge rain rate at the terminal site, and the radar predicted A and XPD values.

In addition to predicting A and XPD of the 01 and 02 paths at 11.4 GHz, we also predict A and XPD along these two paths at 14, 17, 20 and 30 GHz. We perform these higher frequency predictions after the A and XPD values have been predicted for 11.4 GHz. For example, FORWP predicts A and XPD values at 11.4 GHz for a data block in the local path file and stores these data in the comparative data file PATH-01. Next FORWP changes the frequency of the path signal from 11.4 GHz to 17.0 GHz. The FORWP program then calls the MULTI sub-program which predicts A and XPD at 17.0 GHz with the same DSD information used for the 11.4 GHz prediction. The predicted and XPD values at 17.0 GHz are then stored in the comparative data file PATH-03. FORWP stores each path prediction in a separate file for each frequency.

Table 1.2.5-2 summarizes the different frequency predictions performed. The left most column contains the name of the comparative path file in which the A and XPD predictions are stored. The second column from the left indicates the slant path (01 or 02) for which the predictions are made. The last column indicates the frequency at which the predictions are made.

The predicted A and XPD values stored in the comparative data files are used to amass a one year data base. The annual statistics of this data base will be studied using the Statistical Analysis Program.

It should be noted that the INTELSAT contract requires the prediction of A and XPD at a variety of paths not indicated in Table 1.2.5-2. The ability to process these paths has not yet been incorporated into FORWP and will be the subject of future work.

Table 1.2.5-2 A summary of the slant paths for which attenuation and XPD are predicted

Path and File Name	Parallel Path Type	Frequency GHz
Path-01	01	11.4
" -02	02	11.4
" -03	01	14.0
" -04	01	17.0
" -05	01	20.0
" -06	01	30.0
" -07	02	14.0
" -08	02	17.0
" -09	02	20.0
" -10	02	30.0

Chapter 2 Infering Rain Characteristics from Radar and Distrometer Measurements

2.1 Radar Prediction of Rain Characteristics

The experiment outlined in Chapter 1 is designed to predict attenuation (A) and cross polarization discrimination (XPD) on earth-space communication paths from dual-polarized radar data using the computer model FORWP. Measured radar horizontal reflectivity (Z_H) and differential reflectivity (ZDR) data are collected at regular points along the local and remote link paths and are applied to FORWP which predicts A and XPD. The prediction algorithms in FORWP are derived from theoretical models for backward and forward multiple scattering through precipitation. The backward scattering model (BSCAT) is based on work by Stapor [1982]. BSCAT predicts the rain drop size distribution (DSD) from radar measured Z_H and ZDR. The second scattering model (MULTI) is based on multiple scattering theory [Tsolakis and Stutzman, 1982] and uses the predicted DSD's from BSCAT to determine link A and XPD. Predicting A and XPD therefore requires two steps: first, the prediction of the DSD along the

link from radar measured Z_H and ZDR using BSCAT, and second, the prediction of A and XPD from radar derived DSD's.

2.2 A Review of Backscattering Theory

The computer model BSCAT used in the prediction model FORWP was coded from theoretical analysis developed by Stapor [1982]. This analysis was presented in a paper by Stapor and Pratt [1984]. Additional analysis on the model was performed by Pratt and Ozbay [1984]. The model was then modified for this effort and incorporated into the FORWP prediction model.

The theoretical analysis used in BSCAT begins with the development of a single backscattering matrix based on Rayleigh backscattering theory for a single rain drop. Then this single scattering matrix is used to calculate backscattering from a volume of rain drops with rain drop characteristics of shape, size, and canting angle incorporated into the model.

In the backscattering of electromagnetic waves by rain drops, Rayleigh scattering applies for frequencies below 5 GHz. In this frequency range it can be assumed the incident field induces a dipole moment inside the rain drop that instantaneously follows the applied field. Under this assumption, the static techniques developed by Stratton [1941] and Jones [1964] can be used to derive an expression for the back scattering cross section of a single rain drop.

Figure 2.2-1 shows the geometry used in calculating the backscattered field from an oblate spheroidal rain drop with an index of refraction m. The axis of revolution of the rain drop is in the $\hat{n}$ direction, and a is the semi-minor axis length. The vertical component of the induced dipole moment, p_v, lies along this axis. Unit vectors $\hat{\ell}$ and $\hat{m}$ define the equatorial

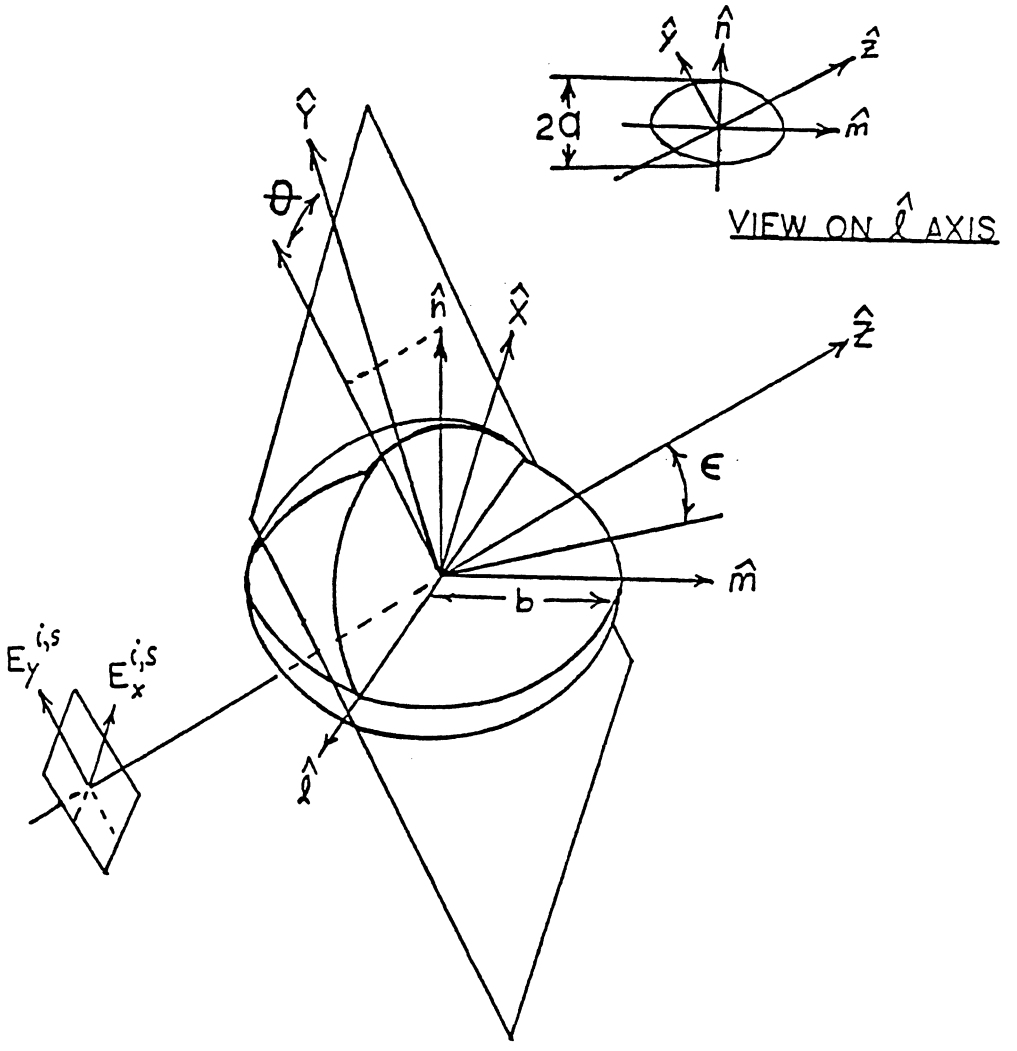

Figure 2.2-1 Geometry for backscattering from an oblate spherical rain drop

plane of the rain drop, and b is the semi-major axis length. The horizontal component of the dipole moment, p_h, lies in this plane. Note that $\hat{n}$, $\hat{\ell}$, and $\hat{m}$ define the rain drop coordinate system.

The unit vectors $\hat{n}, \hat{y}$, and $\hat{z}$ define the incident and scattered field coordinate systems. The elevation angle to the raindrop is ε. The canting angle θ is defined as the angle between the projection of $\hat{n}$ on to the $\hat{x},\hat{y}$ plane and $\hat{y}$. θ orients the rain drop with incident and scattered fields.

With the geometry of the raindrop defined, the backscattering field from a single rain drop is [Stapor, 1982]

$$\begin{bmatrix} E_x^s \\ E_y^s \end{bmatrix} = \frac{k_o^2}{4\pi\varepsilon_o} \begin{bmatrix} (p_v - p_h)\cos^2\varepsilon\sin^2\theta + p_h & (p_v - p_h)\cos^2\varepsilon\frac{\sin 2\theta}{2} \\ (p_v - p_h)\cos^2(\varepsilon)\sin^2\frac{\varepsilon}{2} & (p_v - p_h)\cos^2\varepsilon\cos^2(\theta) + p_h \end{bmatrix} X \qquad (2.2-1)$$

$$\frac{e^{-jk_o r}}{r} \begin{bmatrix} E_x^i \\ E_y^i \end{bmatrix}$$

or

$$E^s = \frac{\exp(-jk_o r)}{r} \begin{bmatrix} f_{11} & f_{12} \\ f_{21} & f_{22} \end{bmatrix} E^i \qquad (2.2-2)$$

The components of the dipole moment are

$$p_h = 4\pi\frac{ab^2}{3}\varepsilon_o(m^2 - 1)\left[\frac{1}{l_1(1 - m^2) + m^2 + 1}\right] \qquad (2.2-3)$$

$$p_v = 4\pi ab^2\varepsilon_o\frac{(m^2 - 1)}{3}E_o(m^2 - 1)\left[\frac{2}{l_1(m^2 - 1) + 1}\right] \qquad (2.2-4)$$

where

$$I_1 = \frac{1}{e^2}\left[1 - (1 - e^2)^{\frac{1}{2}} e^{\frac{1}{2}} \sin^{-1}(e)\right] \qquad (2.2 - 5)$$

and

$$e = \{1 - (a/b)^2\}^{\frac{1}{2}} \qquad (2.2 - 6)$$

which is the eccentricity of the ellipsoid

and where

k_o = $2\pi/\lambda_o$;

λ_o = free space wavelength;

ε_o = permittivity of free space;

r = distance from the scatter to the far-field observation point;

m = complex index of refraction of the drop drop at 20° C.

The matrix [f] in (2.2-2) is the backscattering matrix of a single raindrop and it includes the parameters necessary to describe elevation angle and canting angle effects.

To compute the backscattering from a volume of particles, consider a finite volume filled with rain drops illuminated by a radar. The received energy from the volume is due to the backscattered components of all N scatterers within the volume. The volume extends from range R_1 to R_2 and within the radar antenna half-power beam width θ_B where R_1 and R_2 are the on axis distances from the radar to the near and far edge of the scattering volume. The polar coordinates $(\theta_j, \varphi_j, r_j)$ define the position of the jth scatter within the volume. relative to the radar.

The radar in this experiment transmits at one polarization, and receives in the same polarization and then the radar transmits in another polarization and receives in that polarization. It is assumed that the time between transmissions at adjacent polarizations is sufficient to decorrelate the backscattering signal from successive transmissions, but that the

switching rate between polarizations is fast enough that the characteristics of the rain filled volume have not changed.

Assuming that the radar antenna gain is equal for both polarizations and no mismatch exists in the antenna, the received power from the entire volume can be expressed as [Stapor, 1982]

$$p^r = \left[\frac{\lambda_o}{4\pi}\right]^2 \sum_{j=1}^{N} \frac{G^2(\theta_j, \emptyset_j)B_j}{r_j^4} \qquad (2.2-7)$$

where

$$p^r = \begin{bmatrix} p_{11} & p_{12} \\ p_{21} & p_{22} \end{bmatrix} \qquad (2.2-8)$$

$$B_{1,2} = [\,f_j\,][p^t][f_j]^* \qquad (2.2-9)$$

$$p^t = \begin{bmatrix} p_1 & 0 \\ 0 & p_2 \end{bmatrix} \qquad (2.2-10)$$

$G(\theta_j, \varphi_j)$ is the gain of the antenna, and P^t is the transmitted field vector. The subscripts 1 and 2 are used to account for the general case of two orthogonal polarizations.

Equation (2.2-7) is simplified by calculating the backscattering from a single averaged rain drop cross-section instead of summing the scattered field from each rain drop in the volume. This single averaged cross section is obtained by averaging the cross section of a single rain drop over the particle distributions of position (r_j) , radius (a), oblateness (s), and orientation (θ). The particle distribution for the space volume of scatterers is a function of four variables, $n_o(r,a,\theta,s)$, and is defined as the fraction of particles in the space volume from r to r + dr with equilvolumetric radius of a to a + da, canting angle of θ to $\theta + d\theta$ and oblateness s to s + ds. Averaged over the particle distribution, p^r in (2.2-7) becomes

$$<p^r> = \frac{\lambda}{4\pi^4}\iiint G^2(\theta, \varphi)B(r,a,\theta,s)\, n_o(r,a,\theta,s)drdads \qquad (2.2-11)$$

where the angle brackets denote average quantities. If we assume that the rain drops uniformly fill the volume, that the antenna gain function is Gaussian [Probert-Jones, 1962], and that the antenna phase function is zero, (2.2-11) becomes

$$<p^r> = (\frac{\lambda}{4\pi})^2 G_o^2 \frac{\pi\theta_B^2}{8\ell n2} \frac{R_2 - R_1}{R_1 R_2}\iiint B(a, \theta, s)n(a, \theta, s)da d\theta ds \qquad (2.2-12)$$

where G_o is the on-axis gain of the radar antenna and R_1 and R_2 are the on-axis distance from the radar to the near and far edge of the scattering volume. Since the width of the scattering cell $(R_2 - R_1)$, which corresponds to the transmit pulse length, is much shorter than the distance to the center of the scattering volume (R), (2.2-12) can be approximated by

$$<p^r> = \frac{\lambda}{4\pi^2}G_o^2 \frac{\pi\theta_B}{8\ell n2} \frac{h}{2} \frac{1}{R^2}<B> \qquad (2.2-13)$$

where $h/2 = R_1 - R_2$. $<B>$ is the integral in (2.2-12).

Assuming a, θ, and s are independent, the particle distribution in (2.2-12) can be expressed as the product of three distributions

$$n_o(a, \theta, s) = n(a)t(\theta)p(s) \qquad (2.2-14)$$

The drop size distribution (DSD) used is the three-parameter gamma distribution given by

$$n(a) = N_\mu a^\mu \exp(-\Lambda_\mu a) \qquad (2.2-15)$$

where N_μ, μ, and Λ_μ are DSD parameters and have the following units: μ (dimensionless), $\Lambda_\mu(mm^{-1})$, and $N_\mu(m^{-3}mm^{-(1+\mu)})$

The canting angle θ is defined as the projection of actual canting angle of the rain drop onto the xy-plane as shown in Figure 2.2-1. The canting angle distribution is Gaussian with

mean $<\theta>$ and standard deviation $\sigma(\theta)$. $<\theta>$ and $\sigma(\theta)$ are denoted as simply θ and σ when no confusion will result.

The oblateness of a rain drop is proportional to its axial ratio, (a/b), shown in (2.2.6). Morrison and Cross [1974] give a simple relationship between a/b and a as

$$a/b = 1 - 0.1a \qquad (2.2 - 16)$$

where a is in millimeters. This simple relationship is a good approximation to equations for (a/b) as a function of (a) given by Pruppacher and Beard [1970] and is used in the model BSCAT because it greatly simplifies the backscattering matrix.

The drop shape distribution is bimodal with F_o being the fraction of raindrops that appear to be oblate and $1 - F_o$, the fraction of rain drops that appear spherical.

Including the factored distribution, the integral in (2.2-12)) becomes

$$<B> = \iiint [f] P^T [f]^* \; t(\theta)\, n(a)\; p(s) d\theta da ds \qquad (2.2 - 17)$$

For spherical rain drops, the backscattering matrix becomes

$$[f_{sp}] = \begin{bmatrix} f_s & 0 \\ 0 & f_s \end{bmatrix} \qquad (2.1 - 18)$$

$$f_s = k_o^2 K \frac{\exp(-jk_o r)}{r} \qquad (2.2 - 19)$$

where the reflectivity factor is

$$K = 1/|(m^2 - 1)/(m^2 + 2)| \qquad (2.2 - 20)$$

If equation (2.1.1-18) is averaged over θ and s then it becomes

$$<B> = \left|\frac{P^t}{4\pi}\right| \int_0^\infty \sigma(a) n(a) d(a) \qquad (2.2 - 21)$$

where $\sigma(a)$ is the backscattering cross-section averaged over a and s.

2.3 Radar Measureables

The radar measurables examined in this work are horizontal reflectivity (Z_H) , vertical reflectivity (Z_V), and differential reflectivity (ZDR). The analytical forms of these reflectivity factors used in the back scattering model are defined as follows:

$$Z_H = (\lambda^4/\pi^5|K|^2)\int_0^{a_m}\sigma_H(a)n(a)da \quad [mm^6m^{-3}] \qquad (2.3-1)$$

$$Z_V = (\lambda^4/\pi^5|K|^2)\int_0^{a_m}\sigma_V(a)n(a)da \quad [mm^6m^{-3}] \qquad (2.3-2)$$

$$ZDR = 10\log(Z_H/Z_V) \qquad (2.3-3)$$

$\sigma_H(a)$ and $\sigma_V(a)$ are the backscattering cross-sections of rain drops averaged over θ and s for horizontal and vertical polarizations in mm^2 ; they are defined in (2.2-22). λ is the radar wavelength in mm and a is the equivolumetric drop radius in mm and |K| is the refractivity factor of liquid water and is dimensionless, and a_m is the maximum drop size in mm. The distribution n(a) is the DSD shown in (2.2-16).

It should be noted that much of the literature defines (2.1-1) and (2.1-2) using equivolumetric diameter, D, instead of equivolumetric radius a. This proved to be a source of complication in our work. The values of the DSD parameters Λ_μ and N_μ differ depending on whether radius or diameter is used. To determine the relationship between Λ_μ and N_μ and equivolumetric radius and diameter, we computed the total number of rain drops by integating

(2.2-16) over both radius and diameter and equating the results using primes to denote radius. We derived the following relationships between radius and diameter DSD parameters:

$$N'_\mu = 2N_\mu 2^\mu \qquad (2.3-4)$$

and

$$\Lambda'_\mu = 2\Lambda_\mu \qquad (2.3-5)$$

In predicting DSD's, the general form of the DSD is assumed to be that of (2.2-15), where the parameter μ is determined prior to the prediction process. BSCAT then uses (2.3-1), (2.3-2) and (2.3-3) to calculate the DSD parameters N_μ, Λ_μ from Z_H and ZDR measured in each radar rain volume. But due to the complexity of the analytical form of $\sigma_H(D)$ and $\sigma_\Lambda(D)$, (2.3-1) and (2.3-2) cannot be solved explicitly for Λ_μ and N_μ. This problem can be overcome by using look-up tables or curve fits for the relationships between Z, ZDR and N_μ, Λ_μ .

In the data analysis approach described here, curves for Λ_μ versus ZDR and Z_H/N_μ versus Z_H were calculated using BSCAT for many settings of the rain model parameters, F_o, θ, $\sigma(\theta)$, ε . Cubic spline coefficients were then derived for these curves and stored, for subsequent use in the interpolation procedure. These cubic splines generate two curves: Λ_μ versus ZDR and Z_H/N_m versus Λ_μ. The first curve, Λ_μ versus ZDR, is used to determine Λ_μ from ZDR. This value of Λ_μ applied to the second curve, Z_H/N_μ versus Λ_μ, yields the value of Z_H/N_μ. With the measured value of Z_H known, then N_μ is easily obtained from Z_H/N_μ. Each curve fit procedure is performed for specific values of μ, F_θ, θ, σ and determined before the rain event is processed. Figures 2.3-1 and 2.3-2 give examples of the Λ_μ versus ZDR and Z_H/N_μ versus Λ_μ curves generated from BSCAT, [curves provided by Cahit Ozbay, 1986]. The following parameter settings were used in BSCAT: $F_o = 1, \theta = 0°$, and $\mu = 0$. The BSCAT curves in Figures 2.3-1 and 2.3-2 are compared against two power-law relationship developed by Ulbrich and Atlas [1984]. The BSCAT and power-law curves of Z_H/N_μ versus Λ_μ agree very well, but the BSCAT and power-law curves of Λ_μ versus ZDR show less agreement.

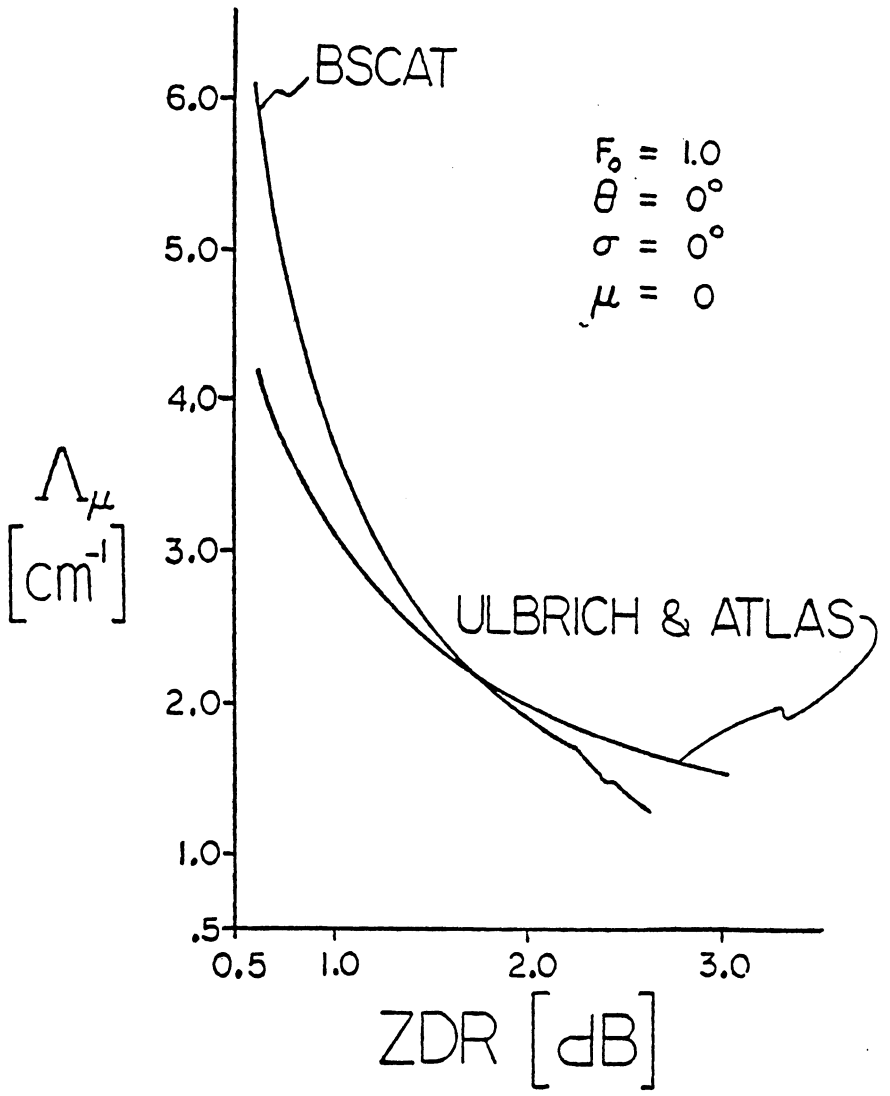

Figure 2.3-1. Λ_μ versus ZDR. Curves generated from BSCAT cubic spline fit from Ulbrich and Atlas's power law relationship

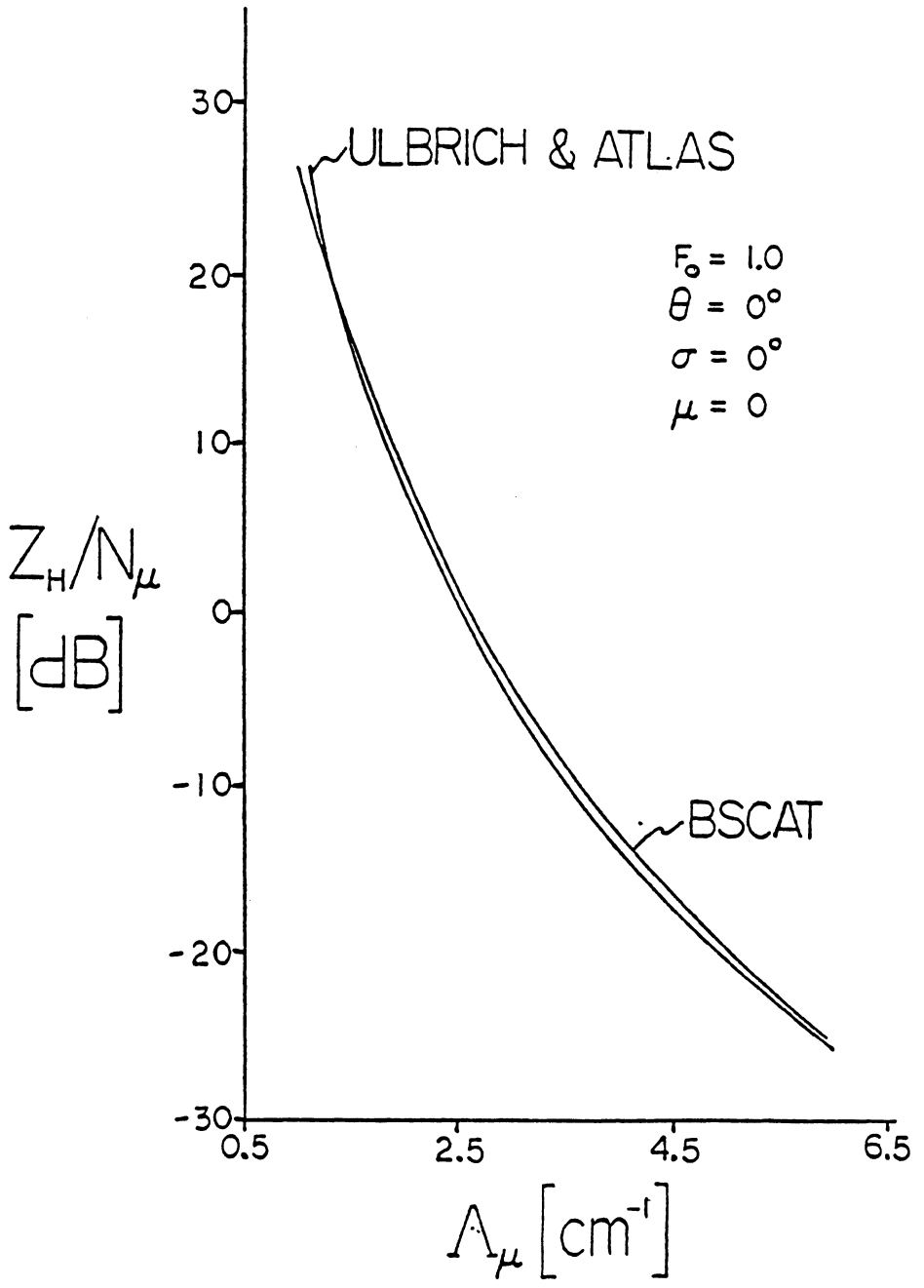

Figure 2.3-2. Z_H normalized to N_μ versus Λ_μ curves generated from BSCAT cubic spline fit and from Ulbrich and Atlas's power law relationship.

2.4 Rain Characteristics

After the DSD is derived from the radar measured Z_H and ZDR values, as described in the previous section, we are able to calculate rainfall rate (R), liquid water content (M), and median volume drop diameter (D_o) using the following

$$R = 0.6\pi\int_0^{D_m} D^3 V(D) n(D) dD \quad [mmh^{-1}] \qquad (2.4-1)$$

$$M = \pi/6\int_0^{D_m} D^3 n(D) dD \quad [gm^{-3}] \qquad (2.4-2)$$

$$2\int_0^{D_o} D^3 n(D) dD = \int_0^{D_m} D^3 n(D) dD \qquad (2.4-3)$$

where V(D) is the terminal velocity of raindrops [Atlas 1971] and is approximated by

$$V(D) = 9.65 - 10.3 \exp(-0.6D) \quad [m/s] \qquad (2.4-4)$$

The liquid water content represents the total mass of water in a cubic meter of air. The median volume drop diameter (D_o) is defined as the rain drop diameter for which in a given volume of space an equal amount of water is produced by rain drops smaller than D_o as there is by rain drops larger then D_o.

The median volume drop diameter will prove to be a useful tool in analyzing the effects of different DSDs.

2.5 Distrometer Prediction of Rain Characteristics

The distrometer is used as a "ground truth" instrument to analyze the radar data and the backscattering model. Since the distrometer directly estimates the drop size distribution it proves especially useful in optimizing the mathematical form of the DSD.

The distrometer used in this experiment is acoustical; it measures rain drop impact momentum and produces a voltage level proportional to the diameter of the rain drop. The distrometer counts the number of rain drops that hit it within a 30 second period for 20 different drop size intervals (bins) and passes these counts in digital form to a collection computer. Using the distrometer counts, and correcting for different drop velocities [Atlas, 1972], a discrete approximation of the real DSD proceeds as follows:

$$n(D_i) \cong N_i V/((D_i)\,\Delta T A D_i) \quad [mm^{-1}m^{-3}] \qquad (2.5-1)$$

where:

D_i = the drop size at the center of the ith bin (mm)

N_i = the number of distrometer counts in the ith bin

$V(D_i)$ = the fall velocity of rain drop size D_i (m/s)

ΔT = the collection time T(s)

A = the area of the distrometer head $(mm)^2$

D_i = the width of the ith bin (mm)

Rain characteristics are calculated from the distrometer derived DSD in (2.5-1) using discrete forms of (2.3-1), (2.3-2), and (2.3-3). Rain rate, liquid water content, and median drop size are calculated by summing the product of distrometer counts, drop sizes, and drop velocities at the center of each drop size bin as follows:

$$R = 0.6\pi \sum_{i=1}^{20} V(D_i) D_i^3 n(D_i) \Delta D_i \quad [mm/h] \qquad (2.5-2)$$

$$M = (\pi/6) \sum_{i=1}^{20} D_i^3 \, n(D_i) \, \Delta D_i \quad [gm/m^3] \qquad (2.5 - 3)$$

$$2 \sum_{i=1}^{J} D_i^3 \, n(D_i) \, \Delta D_i = \sum_{i=1}^{20} D_i^3 \, n(D_i) \qquad (2.5 - 4)$$

where the jth drop size bin contains the median drop size.

It should be noted that when the DSD given by (2.5-1) is used in (2.5-2) to calculate the rain rate the rain fall velocity term cancels out. Therefore, the calculation of rain rate using the distrometer requires no assumption about rain fall velocity.

2.6 *Distrometer Prediction of Z_H and ZDR*

Z_H and ZDR are calculated from (2.3-1), (2.3-2) and (2.3-3) and the distrometer data in the DSD of (2.5-1). Discrete approximations of (2.3-1), (2.3-2), and (2.3-3) are made by summing the product of distrometer counts and backscatter coefficients calculated at the center of each drop size bin. The calculation of radar reflectivity at vertical and horizontal reflectivity is performed by discrete approximations of (2.3-1) and (2.3-2):

$$Z_H = (\lambda^4/\pi^5 |K|^2) \sum_{i=1}^{20} \sigma_H(D_i) n(D_i) \Delta D_i \quad [mm^6 m^{-3}] \qquad (2.6 - 1)$$

$$Z_V = (\lambda^4/\pi^5 |K|^2) \sum_{i=1}^{20} \sigma_V \, n(D_i) \Delta D_i \quad [mm^6 m^{-3}] \qquad (2.6 - 2)$$

2.7 The Inference of Rain Medium Parameter values from Distrometer and Radar Data

2.7.1 Review of Literature

The process of predicting A and XPD from radar measured Z_H and ZDR is very sensitive to the intermediate step of predicting the DSD along the path. The accurate prediction of DSD's and other rain parameters by the use of a dual polarized radar has been advanced by Seliga and Bringi [1976]. Field tests to substantiate this contention have concentrated on demonstrations of the method and its ability to distinguish different types of hydrometers in storms. Among these are the experiments of Bringi et al. [1978], Cherry et al. [1980], Hall et al. [1979, 1981], and Stickel and Seliga [1981]. In each of these investigations, the results obtained for drop size, rainfall rate, liquid water content, and/or hydrometer type are displayed as a function of geographical position in the storm, but no systematic, point-by-point comparisons are made with rain gauges or distrometers.

A limited number of comparisons between radar and "ground truth" instrumentation have been made. One experiment was conducted by Seliga et al. [1981b], which compared radar deduced rain rates with rain gauge data and found an average deviation between radar deduced rain rates and gauge rain rates of 22%. Other investigations include the work of Seliga et al. [1982] and Goddard et al. [1982] which compared radar measured ZDR with distrometer deduced ZDR. Although these two investigations make no quantitative estimates of the difference between rainfall rates measured by radar and distrometer, Goddard et al. [1982] found that their distrometer values of ZDR were systematically larger than those measured by radar. This difference was attributed to theoretical over-estimation of the ratio of the backscattering cross sections at the two polarizations.

Ulbrich and Atlas [1984] made a comparison between radar derived rain rates and gauge rain rates. This work focused on the effects of variation in drop size distribution (DSD) on rain characteristics deduced from radar measured Z_H and ZDR. Ulbrich and Atlas concluded that a gamma distribtuion with DSD parameter of $\mu = 2$ (or $n = 2$) produced better agreement between theoretical and calculated rain rates than did the traditional exponential DSD where $\mu = 0$.

2.7.2 Systematic Comparison of Radar and Distrometer Data

To characterize the rain medium completely along an earth-space propagation path, we must predict the following rain parameters: μ, Λ_μ, N_μ, F_o, θ, and σ at every point along the path. Using our dual-polarized radar, the BSCAT program can be used to determine only the two rain parameter, N_μ and Λ_μ, at a finite number of points along the path. The other four rain parameters must be estimated before the prediction process begins. Even though these other four parameters vary along the path and from rain event to rain event, average values are often used. A satisfactory approach is to assume these remaining parameters to be constant during a rain event. In various research efforts, optimum values of the parameters μ, F_o, θ, and σ have been sought by comparing radar and distrometer measured rain characteristics.

In our present experiment, radar measured Z_H and ZDR values are collected for an entire year from the volume directly over a distrometer. These radar measured Z_H and ZDR values are supplied to the BSCAT portion of the FORWP program that uses (2.3-1), (2.3-2), (2.3-3), and the cubic spline curves explained in Section 2.3 to predict the DSD parameters Λ_μ and N_μ. From the radar-predicted DSD, the rain rate over the distrometer can be predicted using (2.4-1). Using this type of analysis for events, an annual data base can be built up for radar derived Z_H, ZDR, and rain rate over the distrometer.

Corresponding in time with the radar measurements over the distrometer, the DSD can be directly calculated from distrometer data, and then used to calculate rain rate, from (2.5-2), and Z_H and ZDR from (2.6-1) and (2.6-2). These Z_H , ZDR, and R values can be collected in an annual data base compared with the corresponding radar data and rain gauge data.

Using the radar and distrometer data bases, scatter plots can be generated of radar versus distrometer predictions of Z_H, ZDR and R in the volume over the distrometer. These scatter plots would indicate the accuracy of the radar and distrometer calibrations, and the accuracy of the setting of the rain parameters μ, F_o, θ, and σ. Because of the relationship between Z_H, ZDR and R, the order in which these radar and distrometer predicted quantities are compared must be carefully considered as will be explained in more detail later in this section.

A summary of the steps used to compare radar, distrometer, and rain gauge predicted R, and also radar and distrometer predicted Z_H and ZDR, proceeds as follows:

Step 1: The calculated rain rate, R, from the distrometer measured DSDs is compared with the rain rate data, from the rain gauge. This comparison is used to verify the "proper" operation of the distrometer.

Step 2: The comparison of radar measured Z_H data with Z_H data calculated from the distrometer measured DSDs (see (2.6-1)) is used to calibrate the radar.

Step 3: The ZDR data measured by the radar is compared with the ZDR data calculated from the distrometer measured DSDs. This will provide estimates of the rain parameters F_o, θ, and σ.

Step 4: The rain rate data calculated from the distrometer measured DSDs is compared with the rain rate data calculated from the radar derived gamma DSDs (see (2.4-1)). This will provide estimates of the DSD parameter μ.

The comparison of radar and distrometer derived Z_H will reveal the accuracy of the radar calibration. Radars are generally calibrated with a metal sphere hung from a helium-filled balloon. This type of calibration may not be adequate for predicting rain characteristics. A metal sphere is a point object located at one position in the antenna

beam. But, rain will usually fill large portions of the antenna beam; therefore the resulting returned signal is spatially averaged over the beam shape. The effects of spatial averaging on radar calibration is indicated in the work by Cherry and Goddard [1984]. They calibrated their radar with a metal sphere. But after comparing the prediction of rain rate by radar, rain gauges, and distrometers, they concluded that the radar was overpredicting Z_H by 1.5 dB. This overprediction may well be due to the spatial averaging of the antenna beam.

Distrometer data is used to predict Z_H in the volume over the distrometer using (2.6-1). Since the DSD used in (2.6-1) is directly measured using (2.5-1), the only unknown quantities in (2.6-1) are the parameters associated with $\sigma_H(D)$, F_o, θ, and σ. These parameters are related to the non-spherical shape of the rain drops and therefore have a strong effect on the distrometer prediction of ZDR, but a weak effect on the prediction of Z_H. Since the relationship between Z_H and the rain parameters F_o, θ, and σ is weak, the prediction of Z_H by the distrometer should be nearly independent of the assumed values of these rain parameters. Therefore, the only system parameter that can reasonably be adjusted, to optimize agreement between radar and distrometer derived Z_H, is the radar calibration constant.

Once the radar has been calibrated from the comparison with distrometer predicted Z_H values, then a comparison between radar and distrometer predictions of ZDR values can be used to give insight into the prediction of optimum values for F_o, θ, and σ. These three rain parameters modify the effective axial ratio of the rain drops and therefore control the relationship between Z_H and ZDR as predicted by the distrometer. With the agreement between radar and distrometer predicted Z_H already optimized, then the parameters F_o, θ, and σ can be adjusted to yield agreement between predicted ZDR values. The parameters F_o and θ affect the relationship between Z_H and ZDR for all values of ZDR, and σ mainly affects the prediction of larger ZDR values.

Next, the comparison between radar and distrometer predicted rain rate will yield an estimate of the optimum value for the rain parameter μ. The distrometer calculates

predicted rain rates from measured DSD using (2.5-2) and requires no assumptions of any rain parameter. But, prediction of rain rate from radar measured Z_H and ZDR first requires the prediction of the DSD parameters Λ_μ and N_μ using (2.3-1), (2.3-2) and (2.3-3). These equations require assumptions for F_o, θ, and σ.

It should be noted that the prediction of rainrate from radar measured Z_H and ZDR, and the predictions of Z_H and ZDR from distrometer data, requires the use of a rain drop fall velocity relationship. In this work, we have used the Atlas [1981] relationship given by (2.4-4). This approximation appears to be the best drop velocity relationship available at the present time.

2.7.3 Effect of μ on Rain Rate

To analyze the effects of the DSD parameter μ on the prediction of rain rate by BSCAT, we had to isolate the effects of μ from the two other DSD parameters N_μ and Λ_μ. We accomplished this by constraining Λ_μ and N_μ to rain rate and median drop diameter such that as μ changes R and N_o remain constant. Therefore the physical significance of N_μ and Λ_μ does not change with μ. The equations relating Λ_μ and N_μ to R and D_o for different values of μ were derived starting with a simple relationship between Λ_μ, D_o and μ obtained by approximating the integral in (2.3-1) as follows. Applying the gamma distribution of (2.2-16) to (2.3-3) yields

$$2\int_0^{D_o} D^3 N_\mu D^\mu e^{-\Lambda\mu^D} dD = \int_0^{D_m} D^3 N_\mu D^\mu e^{-\Lambda\mu^D} dD \qquad (2.7.3-1)$$

Solving the above integral yields the following relationship [Ulbrich and Atlas, 1984, equation (4)]

$$2\Gamma(4+\mu, \Lambda_\mu D_o) = \Gamma(4+\mu, \Lambda D_m) \qquad (2.7.3-2)$$

where

$$\Gamma(m,D) = \int_0^D x^{m-1} e^{-x} dx \qquad (2.7.3 - 3)$$

According to Ulbrich and Atlas [1984], when $\Lambda_\mu D_o$ is less than 7 and D_m/D_o is less than 2 the solution to (2.7.3-2) can be approximated by

$$\Lambda_\mu D_o = (\mu + 3.672) \qquad (2.7.3 - 4)$$

This result yields an error of less than 2%. Assuming D_o is constant for different values of μ the above equation yields the following relationship between Λ_μ and Λ_o:

$$\Lambda_\mu = \frac{(\mu + 3.672)\Lambda_o}{3.672} \ [mm^{-1}] \qquad (2.7.3 - 5)$$

Next an equation is needed to relate N_μ to N_o for different rain rates. Classical power-law curve fits are available and can be used to relate the DSD parameters N_o and N_μ to rain rate as follows

$$R = N_\mu C_\mu \Lambda_\mu b_\mu \ [mm/h] \qquad (2.7.3 - 6)$$

where C_μ and b_μ are curve fit parameters that depend on μ. The values of μ studied are $\mu = 0$, 2, and 5, and the corresponding curve fit parameters [Ulbrich and Atlas 1984, Ozbay 1986] are $C_o = 0.1003$, $C_2 = 0.02688$, $C_3 = 0.097$, $b_0 = -6.67$, $b_2 = -4.67$, and $b_3 = -9.46$. Assuming $R = R(\mu = 0) = R(\mu = 2) = R(\mu = 5)$ and $Do = Do(\mu = 0) = Do(\mu = 2) = Do(\mu = 5)$, then using (2.7.3-5) and (2.7.3-6) yields

$$N_\mu = N_o[C_o/C_\mu] \left[\frac{\mu + 3.672}{3.672}\right]^{-b_\mu} \Lambda_o(b - b_\mu)^{-3} \ [mm^{-(1+\mu)}] \qquad (2.7.3 - 7)$$

Equations (2.7.3-5) and (2.7.3-7) relate the DSD parameters N_μ and Λ_μ (for $\mu \neq 0$) to N_o ($\mu = 0$) and D_o while keeping D_o and rain rate constant. Therefore, changing the value of μ would have no effect on the rain rate or D_o.

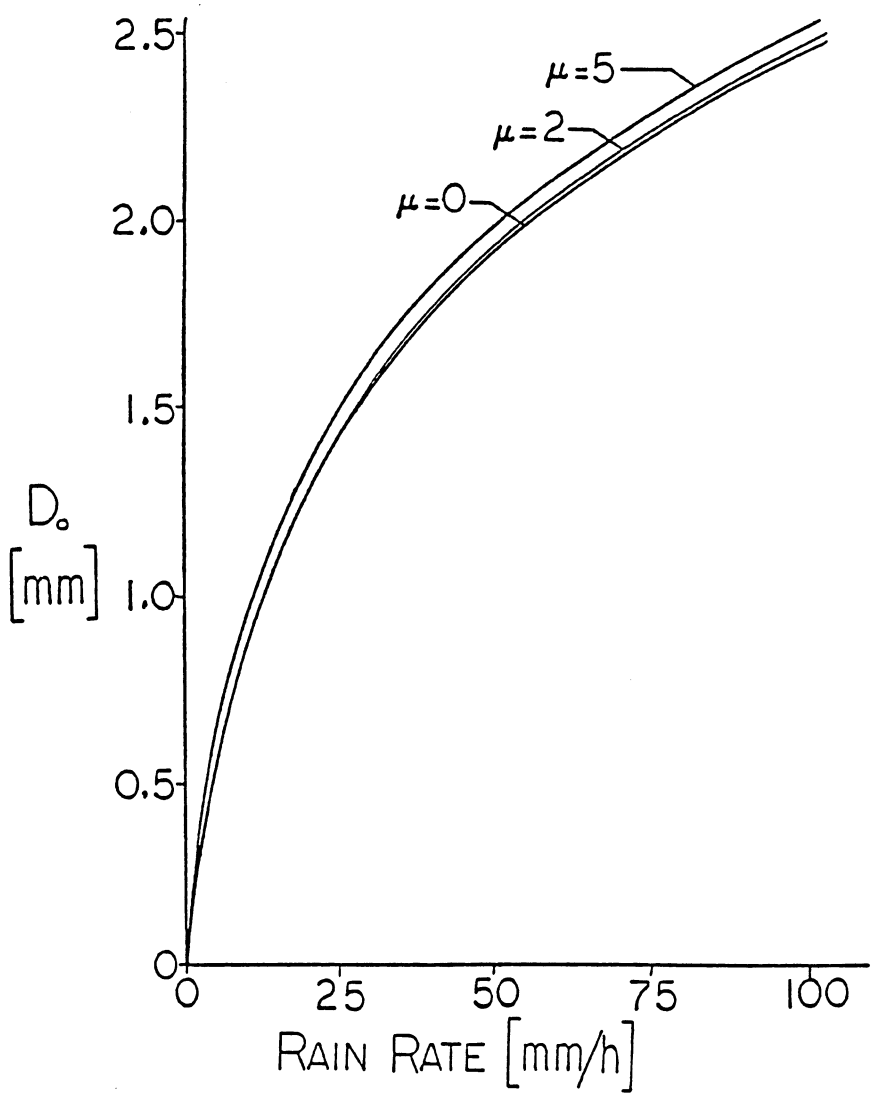

Figure 2.7.3-1. Median rain drop diameter versus rain rate using the relationships in equations (2.7.3-5) and 2.7.3-7) for n = 0, 2, and 5.

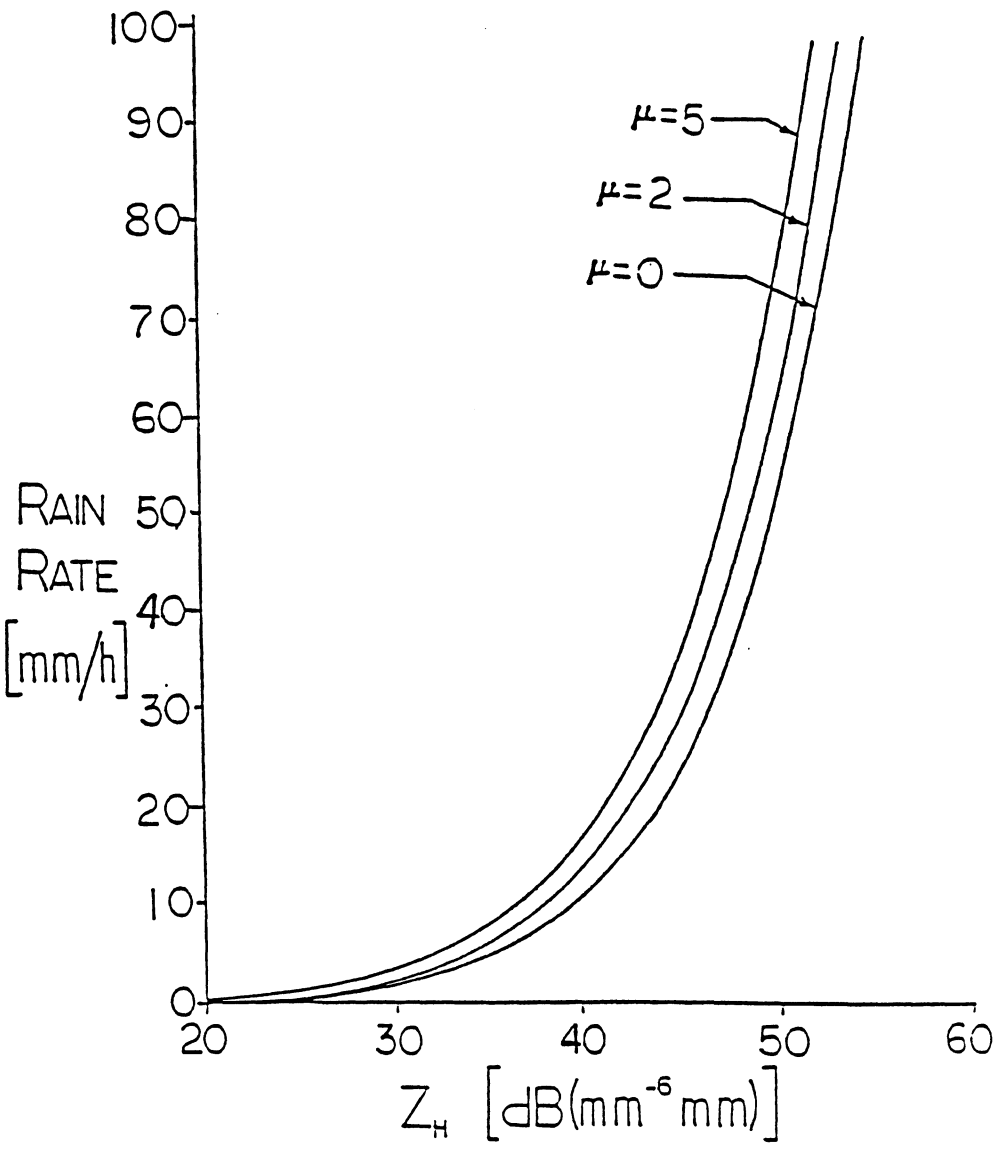

Figure 2.7.3-2. Rain rate versus Z_H with the relationship between rain rate and median drop size independent of μ.

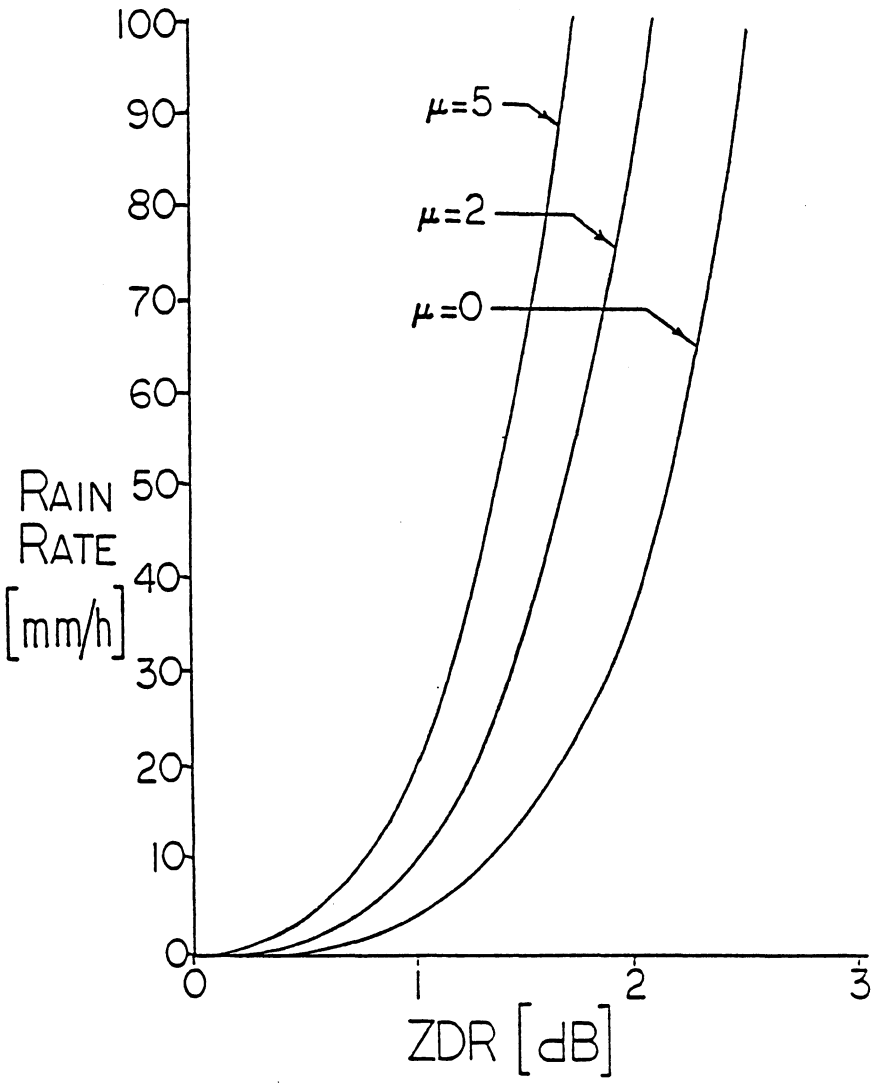

Figure 2.7.3-3. Rain rate versus ZDR with the relationship between rain rate and median drop size independent of μ.

To assess the consistency of the assumptions used in (2.7.3-5) and (2.7.3-7), we assumed the Marshal Palmer DSD relationship at $N_0 = 8000$ and used (2.7.3-6) to relate Λ_o to R for a range of rain rate values. Then we used (2.7.3-5) and (2.7.3-7) to relate N_o and Λ_o to N_μ for this same range of rain rate values. Next these values of N_μ and Λ_μ were used to calculate D_o for $\mu = 0$, 2, and 5 over the same range of rain rates. Figure 2.7.3-1 shows the relationship between R and D_o for $\mu = 0$, 2, and 5. These curves indicate that the relationship between R and D_o is nearly independent of μ as required by our assumptions.

Next we examined the effects of using $\mu = 0$, 2, and 5 on the prediction of rain rate from measured Z and ZDR. The Marshall Palmer relationship for $\mu = 0$ with $N_o = 8000$, was used to calculate Λ_o for a range of R values. Then we used (2.7.3) and (2.7.3) to relate N_μ and Λ_μ to N_o and Λ_o over this range of R values. Next (2.3-1), (2.3-2), and (2.3-3) were used to calculate Z_H and ZDR from N_μ and Λ_μ over the range of rain rate values and for $\mu = 0$, 2, and 5.

Figure 2.7.3-2 gives the curves for predicted rain rate as a function of Z_H for $\mu = 0$, 2, and 5. This figure shows that as μ increases the predicted rain rate increases; recall that D_o is held constant. But this effect is not significant and indicates that the relationship between R and Z_H is relatively insensitive to μ.

Figure 2.7.3-3 gives predicted rain rate as a function of ZDR for $\mu = 0$, 2 and 5. This figure indicates that as μ increases the predicted rain rate increases; recall that D_o is held constant. It is apparent from Figures 2.7.3-2 and 2.7.3-3 that the value of μ has a much greater effect on ZDR than it does on Z_H. The increase in predicted R for a given ZDR value as μ increases is due to the reduction in the number of large rain drops as μ increases in the gamma DSD. The larger rain drops are more oblate than smaller rain drops and are primarily responsible for producing ZDR. Therefore a reduction in the number of large rain drops will require a larger rain rate to produce the same ZDR.

In summary, the overall effect of increasing μ is to increase the rain rate predicted for a given rain cell. Also the parameter μ has a much larger effect on the relationship between prediction of R from ZDR than from Z_H.

Chapter 3 Predicting of Link Performance from Radar Data

The MULTI portion of the FORWP prediction program calculates A and XPD values for earth-space communication paths from radar derived DSD information supplied by the computer model BSCAT (See Chapter 2). MULTI models the earth-space link as dual elliptically-polarized communication channels. The various system blocks in the communications link are represented by a series of matrices. The model accounts for a variety of system effects including the following: antenna polarization, antenna gain, medium depolarization, medium attenuation, and wave guide losses.

3.1 Communication Path Modeling

The propagation path is modeled by a series of homogeneous rain slabs each represented by a scattering matrix. Each rain slab is a maximum of 255 m thick and is centered at consecutive range intervals (range gates) along the communication path.

To simplify the path modeling, all precipitation is assumed to be rain. For the situation where the precipitation extends past the freezing height of the atmosphere, the path range is terminated midway into the bright band of the Z_H vertical profile [Goddard and Cherry, 1984].

The scattering matrix used by MULTI to model the propagation path medium was developed from forward multiple scattering theory. This scattering matrix relates the electric field leaving the path medium with the electric field incident on the medium as follows

$$\begin{bmatrix} E_1 \\ E_2 \end{bmatrix} = \begin{bmatrix} D_{11} & D_{12} \\ D_{21} & D_{22} \end{bmatrix} \begin{bmatrix} E_1^i \\ E_2^i \end{bmatrix} \qquad (3.1-1)$$

or

$$[E] = [D]\ [E^i] \qquad (3.1-2)$$

where [E] contains two orthognal components of the electric field exiting the medium, $[E^i]$ contains two orthognal components of the electrical field entering the path medium normalized to free space loss conditions. [D] is the depolarization matrix for the entire propagation path and the subscripts 1 and 2 refer to the two orthogonal channels. For the clear air case (free space), $[E] = [E^i]$ and $[D]$ is the identity matrix. Any departures from the clear air case are accounted for in the scattering matrix.

MULTI models the propagation path medium with a series of homogenous rain slabs; each rain slab is represented by an individual scattering matrix $[D_i]$. The overall scattering matrix [D] is then the product of the rain slab matrices as follows

$$[D] = [D_1] \cdot \ldots \cdot [D_n] \qquad (3.1-3)$$

The scattering matrix $[D_i]$ for each rain slab is constructed from the DSD parameters Λ_μ and N_μ. These parameters are derived from Z_H and ZDR values measured at center of each rain slab using the program BSCAT as described in Section 2.7.

In modeling the communication channel, MULTI accounts for antenna polarization by the matrices $[A_R]$ and $[A_T]$. These matrices are derived from the polarization parameters (ε, τ) for the receive and transmit antenna in each channel of the communication path [Stutzman, 1977, p. 28]. MULTI relates the electric fields associated with the receive and transmit antennas to link voltages with the conversion matrices $[C_R]$ and $[C_T]$ [Stutzman, 1982, p.28]. These matrices take into account antenna gain, receiver effects, and wave guide losses. Including antenna effects, the end-to-end equation used to model the communication path is then given by

$$[V_R] = [C_R][A_R]^* [D] \{A_T\}^T [C_T]^{-1} [V_T] \qquad (3.1 - 4)$$

where

$$[V_R] = \begin{bmatrix} V_1^r \\ V_2^r \end{bmatrix} \qquad (3.1 - 5)$$

is the phasor voltage matrix at the output of the dual polarized communication link. $[V_T]$ is the transmitter phasor voltage.

3.2 *Link Measured Quantities*

The propagation effects on the communication channel are quantified by cross polarization discrimination (XPD) and attenuation (A). XPD is defined for channel 1 as

$$XPD = 20 \log \left| \frac{|V_{11}|}{|V_{12}|} \right| [dB] \qquad (3.2 - 1)$$

where V_{11} is the signal voltage received at one end of the link in channel 1 arising from a signal voltage transmitted at the other end of the link in channel 1. V_{12} is the signal

voltage received at one end of the link in channel arising from a signal voltage transmitted at the other end of the link in channel 2. The signal applied to the transmitters is the same for V_{11} and V_{12}.

A is defined for channel 1 as

$$A = 20 \text{ Log } \frac{|V_{11}^r|}{|V_{11}^{r'}|} \qquad (3.2 - 2)$$

where $V_1^{r'}$ is the received voltage in clear weather.

3.3 Forward Multiple Scattering Theory

The multiple scattering theory used in the computer model MULTI was developed by Tsolakis and Stutzman [1982]. A detailed description of this multiple scattering model was presented by Runyon and Stutzman [1982]. The presentation here will be an overview of their work. For this work the FORWD program from Runyon and Stutzman [1983] was modified and renamed MULTI. The modifications for this work included the following changes: the correction of some minor coding errors, the incorporation of a gamma drop size distribution See (2.5-16) and the adaptation for use in FORWP the complete prediction model.

The multiple scattering approach determines the propagation effects on plane electromagnetic waves passing through a tenuous medium of discrete scatterers including forward and backward multiple scattering effects. The model includes effects for triple scattering between two scatterers such as the backscattering of particle 1 onto particle 2 which in turn is forward scattered back to particle 1 in the forward direction. But fourth and higher-order scatterings are neglected. The path medium is modeled with a series of rain slabs. The model assumes a homogeneous distribution of

scatterers in each rain sub slab. The model accounts for random variations in the following three rain drop characteristics: rain drop size represented by equivolmetric radius (a), rain drop oblateness (s), and rain drop canting angle θ.

The depolarization matrix for each rain slab is defined as follows

$$[D_i] = e^{-j[k_i]} \qquad (3.3-1)$$

where $[k_i]$ is the propagation constant matrix and is determined from

$$[k_i] = \frac{2\pi}{K_o} L_i \int_\omega [f]\, n_{oi}(\omega)\, d\omega \qquad (3.3-2)$$

where L_i is the thickness of the ith rain slab used to model the link path. Each rain slab is centered about the radar range intervals (range gates) used to probe the path (see Figure 1.2.3-2. $\omega = (a, s, \theta)$ represents the rain drop variables. The scattering matrix for a single rain drop is

$$[f] = \begin{bmatrix} f_{11} & f_{12} \\ f_{21} & f_{22} \end{bmatrix} \qquad (3.3-3)$$

where

$$f_{11} = \frac{1}{2}\{f_V(a) + f_H(a) + \cos 2\theta[f_H(a) - f_V(a)]\} \qquad (3.3-4)$$

$$f_{12} = f_{21} = \frac{1}{2}[f_V(a) - f_H(a)] \sin 2\theta \qquad (3.3-5)$$

$$f_{22} = \frac{1}{2}\{f_V(a) + f_H(a) + \cos 2\theta[f_V(a) - f_H(a)]\} \qquad (3.3-6)$$

and where $f_V(a)$ and $f_H(a)$ are the vertical and horizontal scattering coefficients of a single drop [Runyon and Stutzman, 1982, p. 56]. $n_{oi}(\omega)$ is the rain drop distribution function in size (a),

shape (S) and orientation (θ). If we assume a, S, and θ are independent then $n_{oi}(a)$ can be written as a product of three independent distributions as follows

$$n_{oi}(\omega) = P(\theta)\, t(S)\, n_i(a) \qquad (3.3 - 7)$$

$P(\theta)$ is a Gaussian distribution with a mean θ and a standard deviation σ. t(S) is bimodal with the fraction of oblate drops defined as P1 = F_0 and the fraction of spherical drops defined as $P2 = 1 - F_0$. $n_i(a)$ is the three parameter drop size distribution defined as (repeating 2.2-15)

$$n_i(a) = N_{\mu i}\, a^{\mu}\, e^{-\Lambda_{\mu i} a} \qquad (3.3 - 8)$$

The parameters $\mu, N_{\mu i}$, and $\Lambda_{\mu i}$ are supplied by the program BSCAT in the FORWP prediction model. These parameters are derived from radar Z_H and ZDR values measured at the center of each rain slab used to model the propagation path.

Integrating (3.3-2) over shape (S) and canting angle (θ) gives the following for one components of the propagation constant.

$$k_{mi} = \frac{2\pi}{K_o} L_i \left\{ P_1 f_{mi}^{sph} + P_2 f_m^{obl}(a, <\theta>) \right\} da \qquad (3.3 - 9)$$

where f_m^{sph} is the spherical coefficient which equals zero when $m \neq i$, and f_{mi}^{obl} is the scattering coefficient from (3.3-4), (3.3-5), and (3.3-6) averaged over θ and s. The single drop scattering coefficients inside the integral in (3.2-8) are approximated by polynomial curve fits over a range of drop radius intervals (see Runyon and Stutzman [1983] p. 58). Using these curve fits (3.3-8) involves integrals of the form

$$I = \sum_q \sum_{j=0}^{5} \alpha_{jq} \int_q a^j n_i(a)\, da \qquad (3.3 - 10)$$

where q is a drop radius interval and α_{jq} is the jth polynomial fit coefficient in the qth drop size interval. It should be noted that for drop size interval q = 1, where $a \leq 0.25$ mm, spherical rain

drops are assumed. If the DSD parameter μ is forced to be an integer value, the integral in (3.3-8) has a closed form solution and this greatly reduces the computational time.

MULTI finds the propagation constant of each rain slab scattering matrix in the medium by solving (3.3-10). For each rain slab, a different set of polynominal coefficients are used to solve (3.3-10).

3.4 The Effect of the DSD Parameter μ On MULTI

For this work one of the modifications made to the original multiple scattering model [Runyon, 1983] was the incorporation of the three parameter gamma drop size distribution (see (3.2-8)). Originally an exponential DSD was used in which $\mu = 0$. To analyze the effect of μ on the model MULTI, we used the same procedure that was used to test the effects of μ values on BSCAT as outlined in Section 2.7.3.

To test MULTI, a computer simulated earth-space link path was constructed. The path was filled with a homogeneous rain out to a range of 4 km. The spatially uniform rain rate in the path was varied over a range of 0-50 mm/h. Equations (2.7.3-5) and (2.7.3-7) were used on the rain medium in the simulated path to hold the rain rate and median drop size independent of μ. Then MULTI was used to predict A and XPD for rain rates of 0-50 mm/h with $\mu = 0$, 2, and 5.

Figures 3.4-1 and 3.4-2 show the curves of A and XPD versus rain rate for $\mu = 0$, 2, and 5. The computer simulated described above was used. The other rain parameters were set to the following values: $F_o = 0.6$, $\theta = 0°$, and $\sigma = 12°$. The frequency of the signal was 11.0 GHz. As the parameter μ increased, predicted attenuation decreased slightly. This effect is more pronounced at higher rain rates. Also as μ increases XPD increases.

The decrease in attenuation with increasing μ can be explained by considering (2.7-5) and (2.7-7) which force the median drop size to remain constant for a given rain rate.

Therefore as μ increases, the median drop size and rain rate is constant, but the number of rain drops considerably larger and smaller than the median drop size decreases. To keep the rain rate constant, the number of rain drops around the median drop size must significantly increase. Rain drops considerably larger the median drop size ($D \geq 0.4$ cm) have a greater effect on attenuation than rain drops around the median drop size. Therefore the decrease in the number of large rain drops has a stronger effect on attenuation then the increase in median size drops. This decrease in larger rain drops results in a decrease in attenuation.

Figure 3.4-2 shows an increase in predicted XPD as μ increases. This effect corresponds with the decrease of A with μ. As A decreases, XPD becomes more favorable (increase). From Figure 3.4-2, it appears that μ has a more pronounced effect on XPD at lower rain rates, but for probable situations μ has negligible impact on XPD.

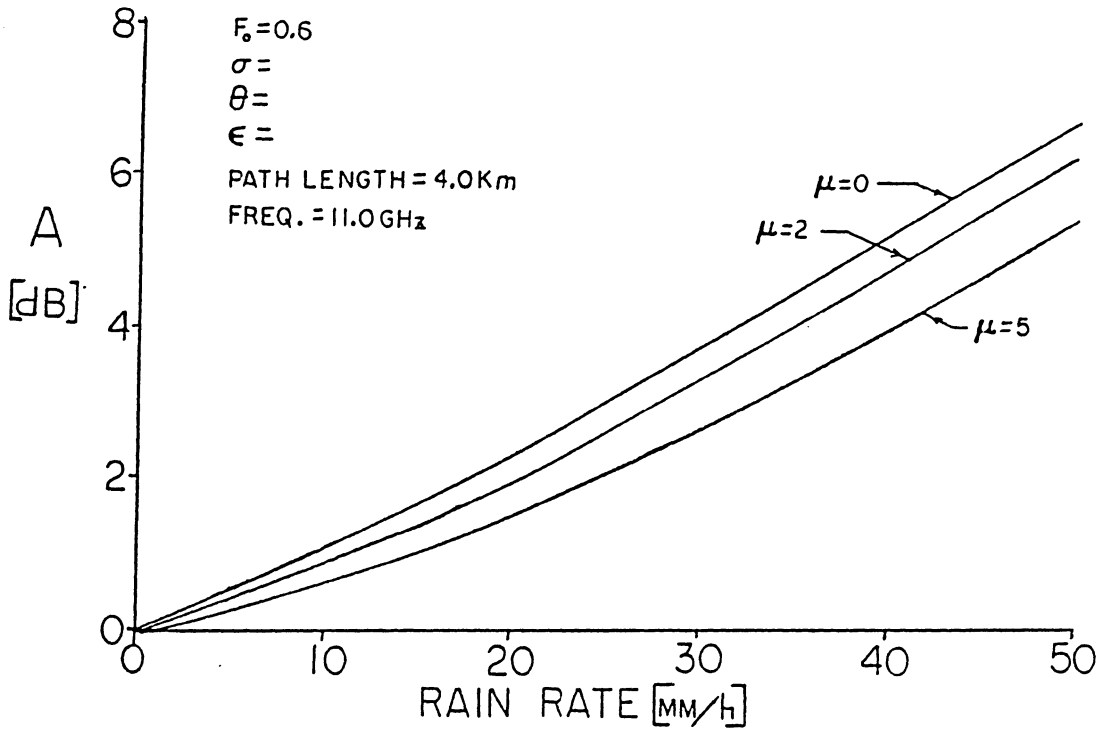

Figure 3.4-1. Attenuation calculated for various μ values of the gamma drop size distribution as a function of uniform rain rate along a 4 km slant path.

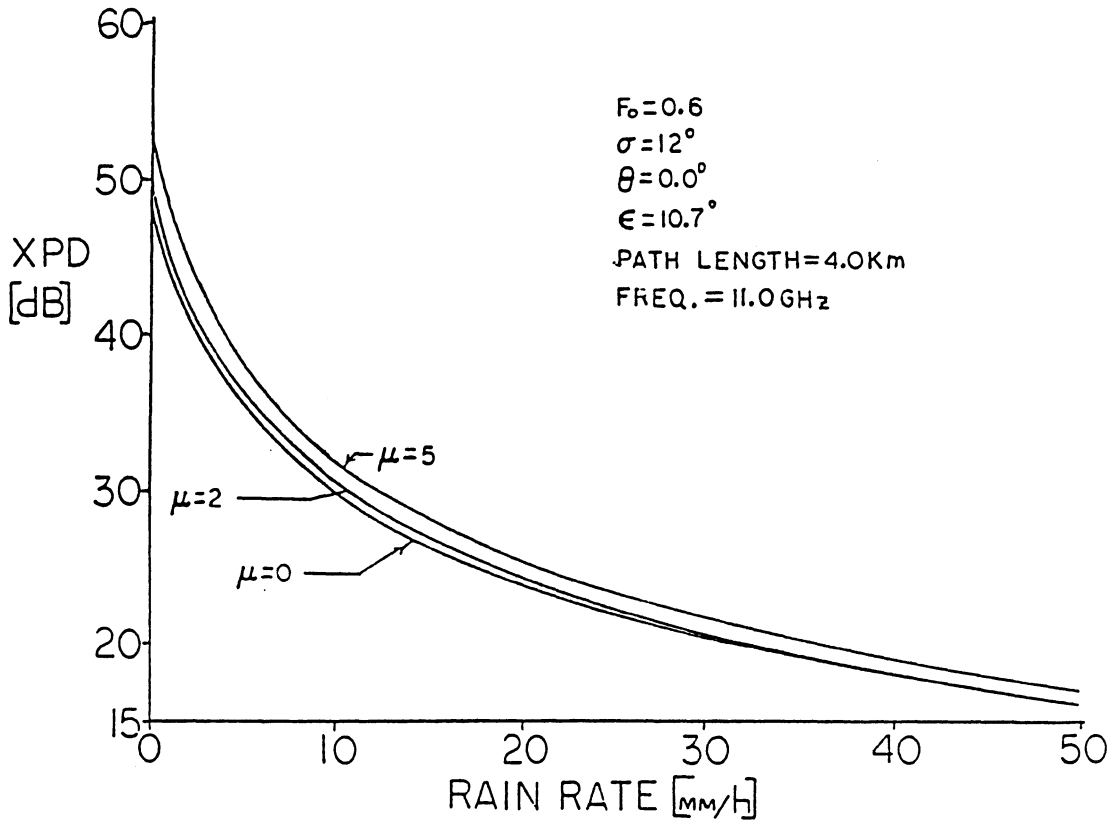

Figure 3.4-2 Cross-polarization calculated for various μ values of the gamma drop size distribution as a function of the rain rate along a 4 km slant path of uniform rain.

Chapter 4 EVALUATION OF FORWP

4.1 Two Semi-Empirical Prediction Models

Two simple semi-empirical prediction models have been developed to test FORWP. The first simple model (Z-Model) predicts link path attenuation solely from Z_H data. The second simple model (Z, ZDR-Model) predicts link path attenuation from both Z_H and ZDR data.

Both simple models assume a series of homogeneous rain slabs each 255 m thick in order to model the propagation path. Each rain slab is centered about a radar range gate (range interval) data point where Z_H and ZDR are collected. This Z_H, ZDR data is then used to estimate the rain rate in each rain slab. Using these estimated rain rate values, semi-empirical power-law relationships are used to calculate the attenuation due to each rain slab in the link. Finally the attenuation from each rain slab is summed over the link path to predict the total link attenuation. These models do not predict XPD.

The Z-Model model predicts the rain rate for each rain slab from the radar measured Z_H values using the empirical power-law relationship given by Ulbrich and Atlas [1977] as follows

$$R = d\, Z_H^e \qquad (4.1-1)$$

where d = 0.01563 [$mm/h^{-1}\,(mm^6m^{-3})^{-e}$] and e = 0.7042. The Z, ZDR-Model predicts the rain rate for each rain slab using a semi-empirical expression relating rain rate to Z_H and ZDR developed by Ulbrich and Atlas [1983].

A summary of the development of the Ulbrich and Atlas rain rate to Z_H and ZDR expression is now described. First, consider the expression for Z_H in (2.3-1) developed earlier. If we change the units on D from [mm] to [cm], (2.3-1) becomes

$$Z_H = \frac{10^6\lambda^4}{\Pi^5|K|^2} \int_0^{D_m} \sigma_H(D)n(D)dD\ [mm^6m^{-3}] \qquad (4.1-2)$$

where D is in [cm], and $\sigma_H(D)[cm^2]$ is the backscattering cross-section averaged over drop shape and drop canting angle. $n(D)[cmm^3]$ is the three parameter gamma drop size distribution (see equation (2.2-16)). A very good approximation for $\sigma(D)$ in (4.1-2) is the Rayleigh backscattering cross-section for a single spherical rain drop gives by Ulbrich and Atlas [1984] as

$$\sigma_H(D) = \pi^5\,|K|^2\,D^6/\lambda^4\ [cm] \qquad (4.1-3)$$

where D is in [cm]; λ = 10.0 [cm], and K is the reflectivity factor. Another reasonable approximation on (4.2-2) can be made by replacing D_m by ∞ [Ulbrich and Atlas, 1984]. If we use the above assumptions for D_m and $\sigma_H(D)$ and force μ to be an integer (4.1-2) has a closed form solution as follows [Ulbrich and Atlas, 1984, equation (9)]

$$Z_H = 10^6\,(6+\mu)!\,N_\mu\,\Lambda_\mu^{-(7+\mu)}\ [mm^6m^{-3}] \qquad (4.1-4)$$

Next consider the expression for rain rate in (2.4-1). If we change the units on D from [mm] to [cm] and replace D_m with ∞, (2.4-1) becomes

$$R = 0.6\pi \int_0^{\infty} D^3\,V(D)\,D(D)\,dD[mm/h] \qquad (4.1-5)$$

where D is in [cm]; $n(D)$ $[cm/m^3]$ is defined by (2.2-16), and V(D)[m/s] is the raindrop fall velocity. Ulbrich and Atlas [1984] give a power law expression for the drop fall velocity as follows

$$V(D) = \gamma D^{0.67} [m/s] \qquad (4.1 - 6)$$

where $\gamma = 17.67$ $[ms^{-1}cm^{-0.67}]$, and D is in [cm]. An average drop fall velocity that provides a good approximation to the above equation [Ulbrich and Atlas, 1984] is given by

$$V = \gamma D_o^{0.67} \ [m/s] \qquad (4.1 - 7)$$

where D_o [cm] is the median drop size. If (4.1-6) is used in (4.1-5), we cannot solve (4.1-5) in closed form, but if we use the approximation in (4.1-7) a closed form solution of (4.1-5) exists as follows

$$R = 0.6\pi \gamma D_o^{0.67} \ (3 + \mu) \ N_\mu \Lambda_\mu^{-(4+\mu)} [mm/h] \qquad (4.1 - 8)$$

We then combine (4.1-4) and (4.1-8) to eliminate N_μ and use the relationship $D_o \Lambda_\mu = \mu + 3.67$ in (2.4-12) to eliminate Λ_μ. The following relationship between R, Z_H and D_o results

$$R = G_\mu Z_H D_o^{-2.33} \ [mm/h] \qquad (4.1 - 9)$$

where Z_H is in $[mm^6m^{-3}]$; $D_o[cm]$ is the median drop diameter; $G_0 = 1.37 \times 10^{-5}$ for $\mu = 0$, and $G_2 = 1.806 \times 10^{-5}$ for $\mu = 2$. Next we use an empirical power-law relationship [Ulbrich and Atlas, 1984,equation (10)] to relate D_o to ZDR as follows

$$ZDR = C_\mu D_o^{1.55} [dB] \qquad (4.1 - 10)$$

where $C_o = 27.1$ [dB $cm^{-1.55}$] for $\mu = 0$, and $C_2 = 20.6$ [dB $cm^{-1.55}$] for $\mu = 2$. We combine (4.1-9) and (4.1-10) to eliminate D_o , and the following rain rate, Z_H, and ZDR relationship results

$$R = g_\mu Z_H ZDR^{-1.5} \text{ [mm/h]} \qquad (4.1-11)$$

where Z_H is in $[mm^6m^{-3}]$; ZDR is in [dB]; $g_0 = 1.93 \times 10^{-3}$ for $\mu = 0$; and $g_2 = 5.50 \times 10^{-4}$ for $\mu = 2$. Equation (4.1-11) gives a simple and, as we shall see, reasonably accurate relationship between rain rate Z_H and ZDR [Ulbrich and Atlas, 1984]. It should be noted that rain rate is inversely related to ZDR.

With the rain rate in each rain slab estimated through (4.1-1) or (4.1-11), we then use known power law relationships to relate rain rate to attenuation [Olsen et al. (1978)] as follows

$$\alpha(R) = a R^b \text{ [dB/km]} \qquad (4.1-12)$$

where R is in [mm/h], and a and b are given for the frequency of interest

$$a(f) = 4.21 \times 10^{-5} f^{2.42} \quad 2.9 \le f < 54\text{GHz} \qquad (4.1-13)$$

$$b(f) = 1.41 f^{-0.0779} \quad 8.5 \le f < 25\text{GHz} \qquad (4.1-14)$$

The attenuation for the entire path is then obtained by summing the contributions from each rain slab. For the Z-Model, this summation is given by

$$A(Z_H) = \sum_{i=1}^{m} L_i a(Z_{Hi}^e)^b \text{ [dB]} \qquad (4.1-15)$$

and for the Z, ZDR-Model this summation is given by

$$A(Z_H, ZDR) = \sum_{i=1}^{m} L_i a(g_\mu Z_{Hi} ZDR_i^{-1.5})^b \text{ [dB]} \qquad (4.1-16)$$

were $Z_{Hi}[mm^6mm^{-3}]$ is the measured Z_H value in the ith range interval; ZDR_i [dB] is the measured ZDR value in the ith range interval; a and b are defined by (4.1-13) and (4.1-14); e is defined by (4.1-1); g_μ is defined by (4.1-11) and L_i is the thickness of the ith rain slab used to model the path. Each rain slab is centered about a radar range interval (range gate) used to probe the path. The above path models (4.1-15) and (4.1-16) stop the path integration at the

nth range interval which ends midway into the Z_H bright band. If there is no Z_H bright band, path integration is stopped at the last rain slab with significant attenuation along the path. Therefore the summations in (4.1-15) and (4.1-16) end with the mth rain cell that either terminates closest to the center of the Z_H bright band or represents the last rain slab along the path of significant attenuation.

4.2 *Initial Analysis and Verification of the FORWP Prediction Model*

The values of A and XPD produced by FORWP were tested by performing calculations for attenuation with a computer simulated propagation path. The result of these calculations were also compared with Z-Model and Z, ZDR-Model predictions. In this section we present the results of these tests.

The computer simulated path we constructed had an elevation angle of $\varepsilon = 18.50°$ and was filled with a homogeneous rain medium out to a slant range of 3.57 km. This range corresponds to 14 consecutive rain slabs of 255 m each. We assumed that radar data points were collected from the center of each rain slab and that each rain slab produced the same Z_H and ZDR value. The signal frequency (f) of the path was set to 11.0 GHz. The rain parameters for the path were the following: $F_0 = 1.0$, $\theta = 0°$, $\sigma = 0°$, and $\mu = 0$.

4.2.1 Attenuation

To test the attenuation predictions of FORWP, various combinations of Z_H and ZDR values were assumed along the simulated path. Figures 4.2.1-1 through 4.2.1 give the predicted link attenuations on the simulated path by FORWP, Z-Model, and Z, ZDR-Model as a function of Z_H for ZDR = 0.4 dB, 1.05 dB, 1.70 dB, 2.35 dB and 3.0 dB respectively. The range of Z_H values was 0 - 60 [dB (mm^6m^{-3})] which represents typical radar measured values. The range of predicted attenuation values was 0 - 60 dB. This large attenuation range was used because the attenuation due to a single rain slab is a fourteenth of the entire path and gives attenuation values of 0 to 4.3 dB. These values are realistic for the attenuation in a 255 m thick rain slab. The attenuation due to a single rain slab is more representative of heavy rain events than the uniform path assumption which leads to very high attenuations. In other words, heavy rain is not likely to extend over the entire path and is better represented for test purposes by the attenuation due to one rain slab.

It should be noted in Figures 4.2.1-1 through 4.2.1-5, there are discontinuities in the FORWP prediction curves. These discontinuities are due to the polynomial curve fits used to approximate the forward scattering cross-sections (see (3.3-10)). FORWP uses these curve fits over five drop size intervals. For various combinations of Z_H and ZDR, the transition from one drop size to another is magnified and a discontinuity results. These discontinuities will go unnoticed in the prediction of A from real radar data.

The predictions of the three models are compared in Figures 4.2.1-1 through 4.2.1-5. These curves indicate that, for ZDR $\leq$ 0.5 dB and $Z_H \leq$ 30 dB ($mm^6\,m^{-3}$), the three prediction models agree fairly well. Since the Z-Model depends only on Z_H, this agreement between the three models indicates that ZDR provides little information in predicting attenuation when ZDR $\leq$ 0.5 dB and $Z_H \leq 30dB$ (mm^6m^{-3}).

Figures 4.2.1-1 through 4.2.1-5 also indicate that for ZDR $\geq$ 0.5 dB (mm^6m^{-3}) and $Z_H \leq 30dB$ (mm^6m^{-3}) the Z-Model predicts much higher attenuation values than the Z,

ZDR-Model which slightly over predicts the results of FORWP. The Z, ZDR-Model and FORWP agree closely for larger Z_H and ZDR values but they both depart significantly from the Z-Model. The lack of agreement of FORWP and Z, ZDR-Model indicates that, for larger Z_H and ZDR values, ZDR becomes critical in predicting attenuation.

Figures 4.2.1-6 through 4.2.1-8 give predicted link attenuation on the simulated link path by FORWP, the Z, ZDR-Model, and the Z-Model as a function of ZDR for Z_H = 0.4, 47.5, and 60 [dB (mm^6m^{-3})]. The range of ZDR values is 0.4 dB to 3 dB corresponding to typical measured values. In these figures, the Z-Model prediction is a horizontal line since it is independent of ZDR. The Z, ZDR-Model and FORWP predictions agree fairly closely for Z_H values below 50 dB ($mm^6\,m^{-3}$). But for largerZ_H values, Z, ZDR Model predicts lower attenuations than the FORWP model.

It is observed from figures 4.2.1-6 through 4.2.1-8 that the Z, ZDR-Model and FORWP predict attenuation values for a given Z_H value that decrease with increasing ZDR. This inverse relationship between A and ZDR can be explained from (4.2-11) which shows an inverse relationship between R and ZDR for a given Z_H . As a result, increasing ZDR decreases the rain rate and therefore the predicted attenuation decreases because of the direct relationship between rain rate and attenuation. Another way to view this inverse relationship between A and ZDR is to consider the homogeneous medium used to construct the simulated path. This medium was forced to produce a constant Z_H value while ZDR was varied. For a rain drop in this medium, the effective horizontal cross-section is the primary factor in determining Z_H . With a constant Z_H value and therefore a constant horizontal cross-section, the vertical cross-section of the rain drop will vary as ZDR varies. Therefore as ZDR increases, Z_V decreases and the vertical cross-section of the rain drops decreases. With a constant horizontal cross-section, a decrease in the vertical cross-section will decrease the water volume of the rain drop. This decreased water volume will decrease the rain rate which in turn decreases the predicted attenuation.

These tests have shown that as expected FORWP predictions agree grossly with the Z-Model and relatively closely to the Z, ZDR-Model. We concluded that the FORWP prediction

model had been coded and constructed correctly. This comparison between FORWP, the Z, ZDR-Model and the Z-Model will also prove beneficial in assessing our prediction results for real events.

4.2.2 Cross Polarization

We evaluate the cross polarization predictions of FORWP, by assuming various combinations of Z_H and ZDR values along the simulated path described in Section 4.2. Figures 4.2.2-1 and 4.2.2-2 give XPD as a function of Z_H and ZDR. The range of XPD is 0 to 90 dB which represents typical values that are associated with the range of attenuation values used in Section 4.2.1. The ranges of Z_H and ZDR are 0 to 60 [dB($mm^6\,m^{-3}$)] and 0 to 3 [dB] which represent typical radar measured values.

To test the cross polarization prediction characteristics of FORWP shown in Figures 4.2.2-1 and 4.2.2-2, we derived a simple relationship between XPD, Z_H, and ZDR. The Stutzman and Runyon [1984] "SIM" isolation model was used to develop the simple relationship. The SIM model provides a relationship between A and XPD that is relatively invariant and can be expressed as follows (see equation (2), Stuzman and Runyon [1984])

$$XPD = U - V \log(A) \qquad (4.2.2 - 1)$$

where all quantities are in dB and the log is base 10. The V coefficient is chosen to be a constant value of 19. The coefficient U is dependent on a variety of system and rain parameters, but since the simulated test path is assumed to be filled with a constant uniform rain then U is also a constant for the following evaluation.

With (4.2.2-1) providing a simple relationship between XPD and A, we then use (4.1-16) to relate A to Z_H and ZDR. Since the simulated test path is filled with a constant uniform rain,

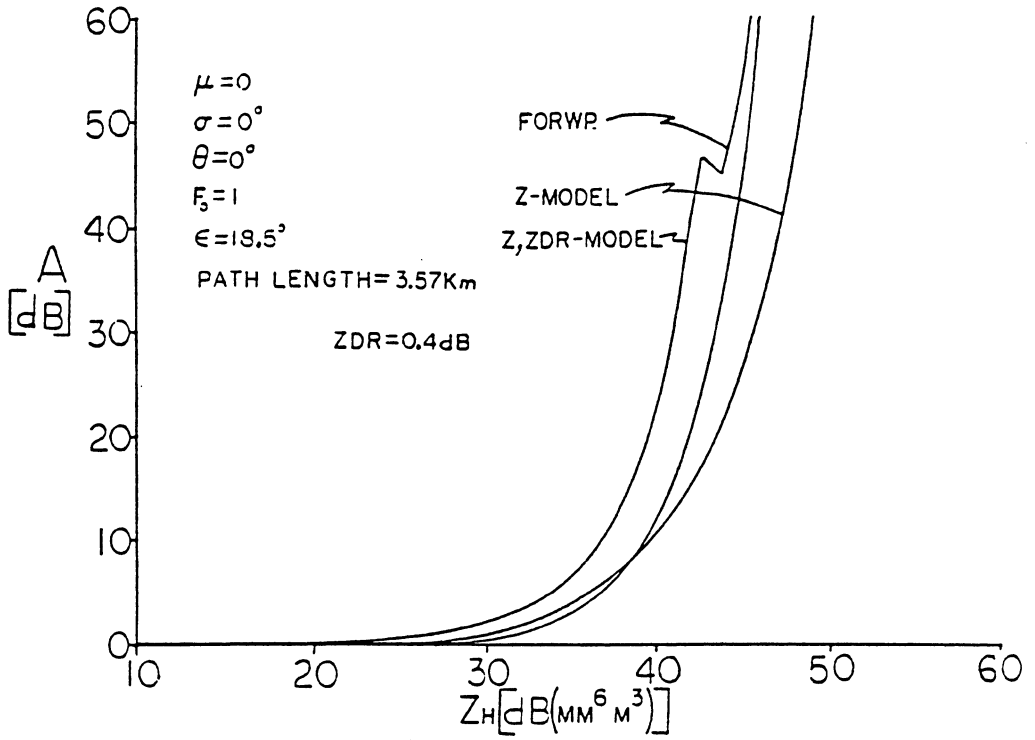

Figure 4.2.1-1 Predicted attenuation on simulated path by three prediction models as a function of Z_H for ZDR=0.4dB.

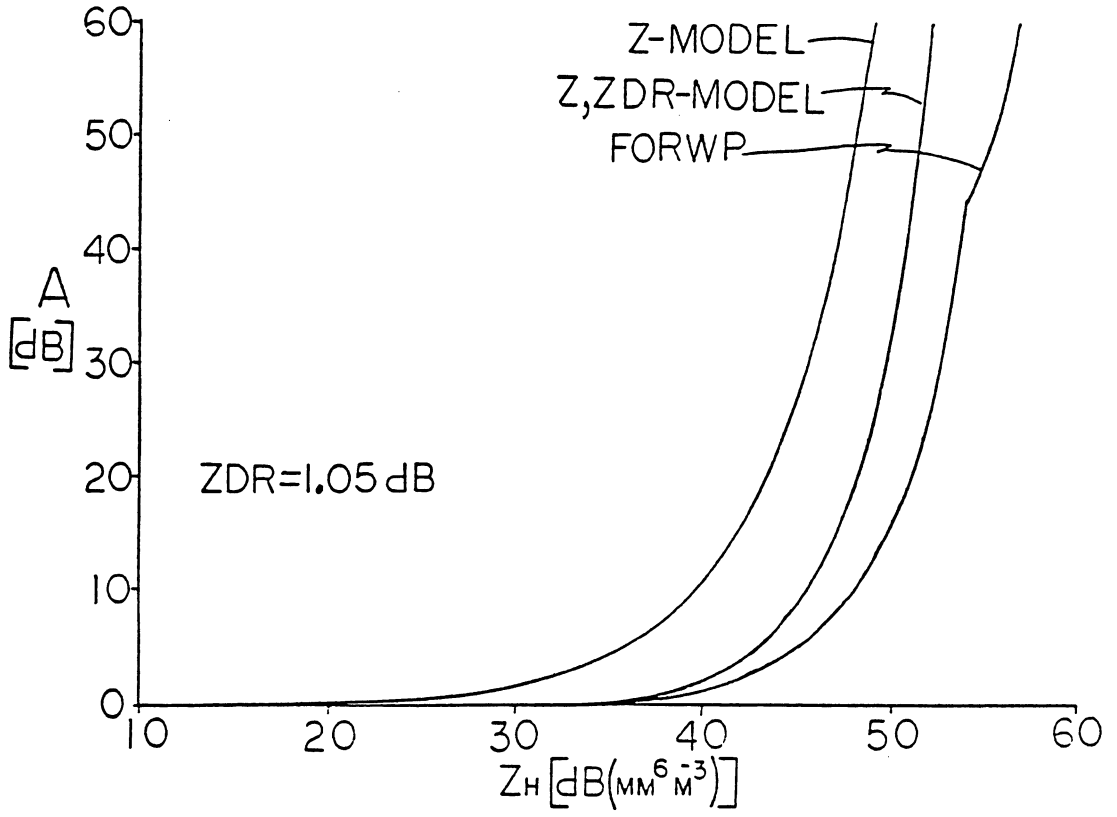

Figure 4.2.1-2 Predicted attenuation on simulated path by three prediction models as a function of Z_H for ZDR = 1.05dB

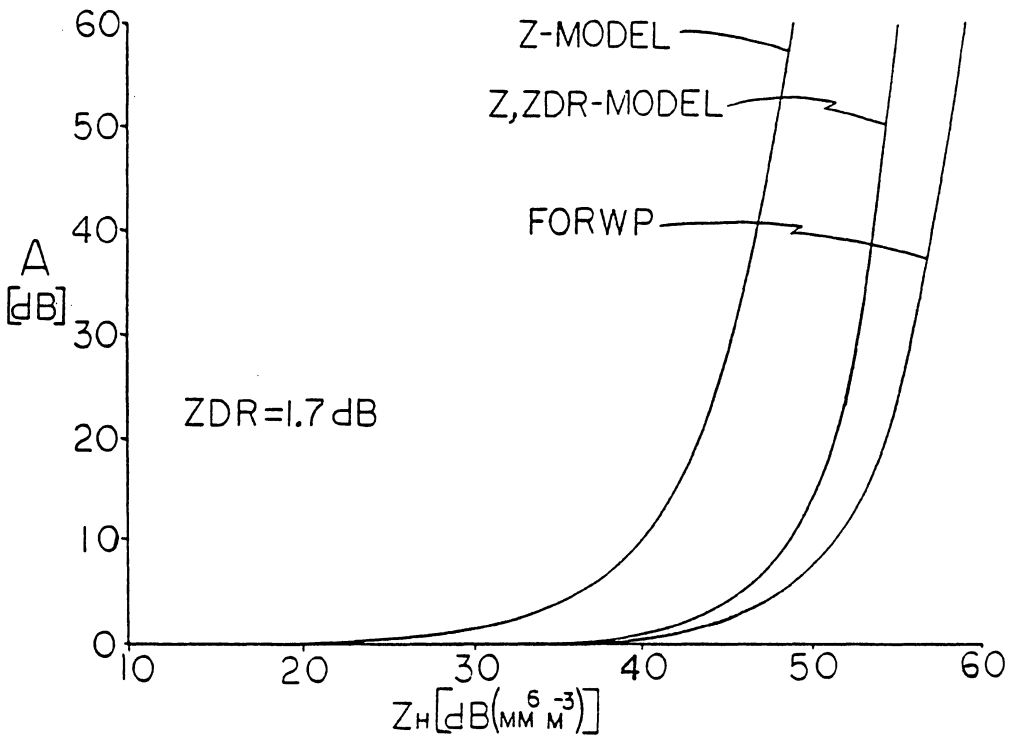

Figure 4.2.1-3 Predicted attenuation on simulated path by three prediction models as a function of Z_H for ZDR = 1.7dB.

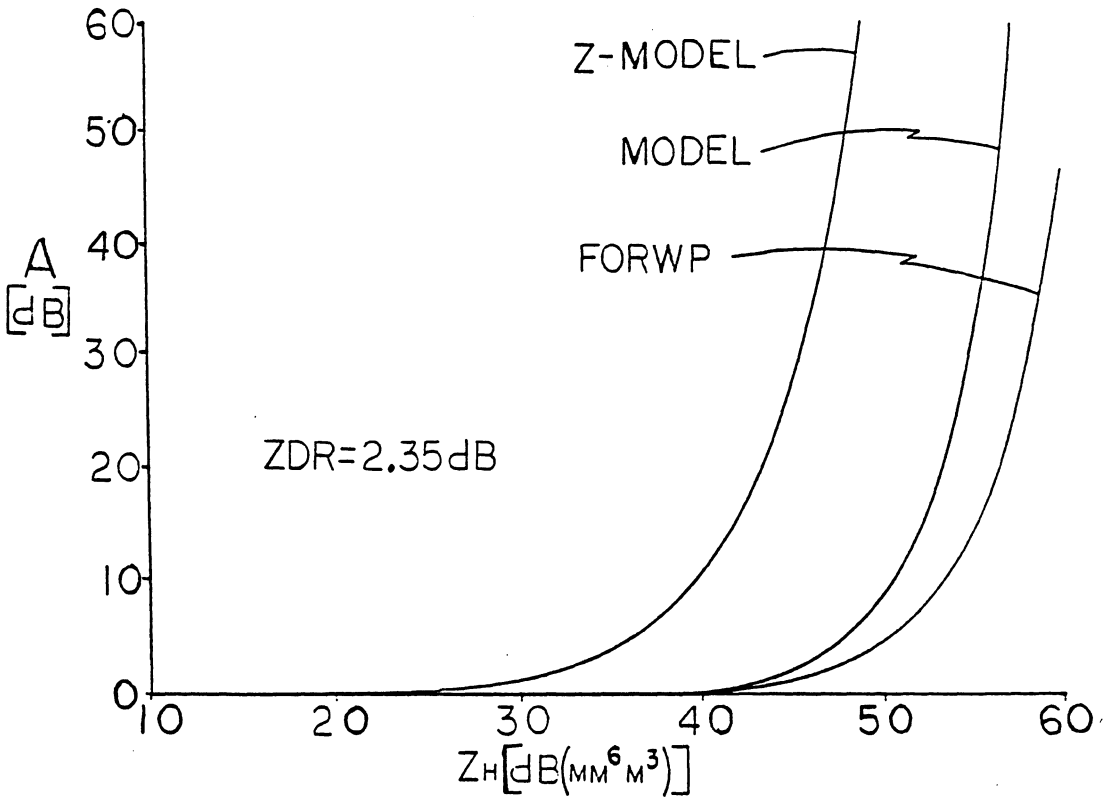

Figure 4.2.1-4 Predicted attenuation on simulated path by three prediction models as a function of Z_H for ZDR = 2.34dB

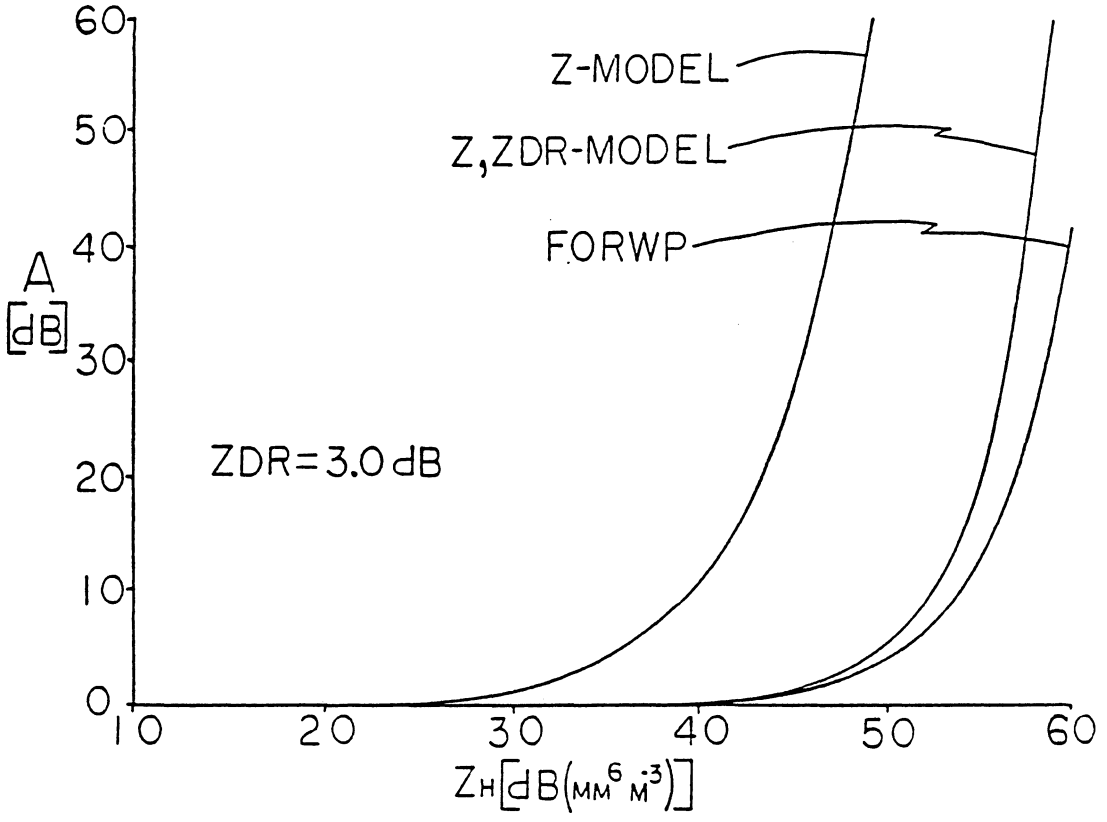

Figure 4.2.1-5 Predicted attenuation on simulated path by three prediction models as a function of Z_H for ZDR = 3.0dB.

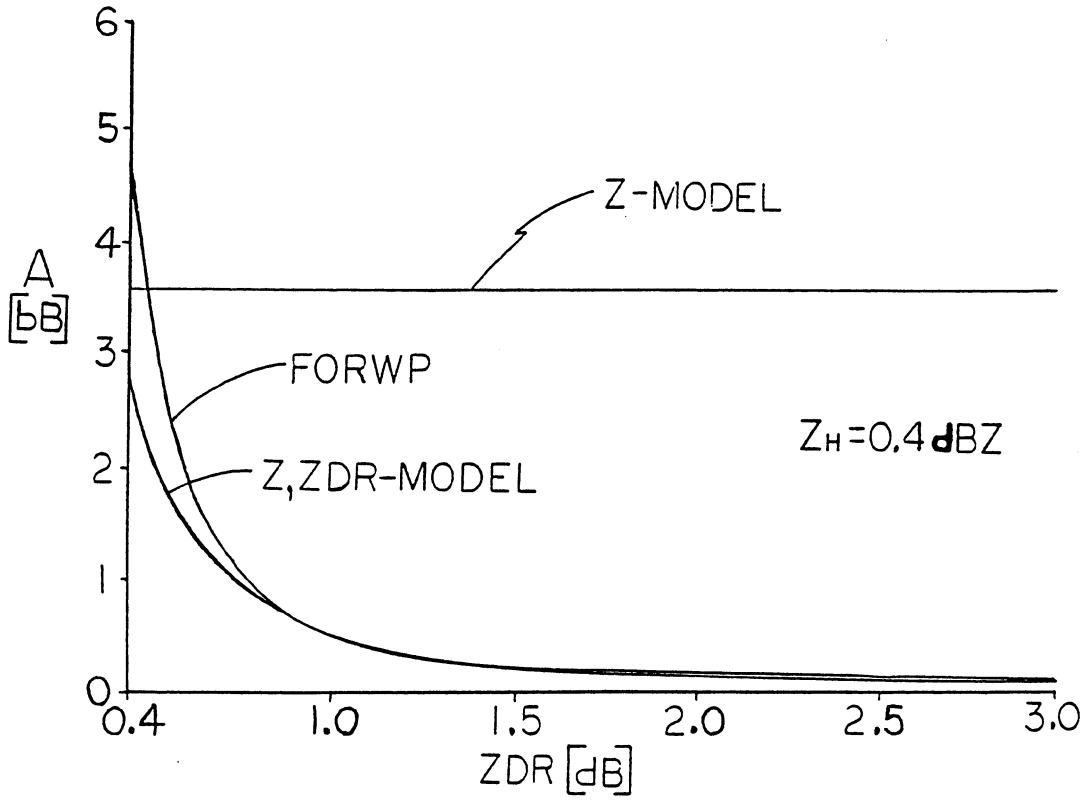

Figure 4.2.1-6 Predicted attenuation as a function of ZDR on a simulated link using three prediction models for Z_H= 0.4dB (mm^6 m^{-3})

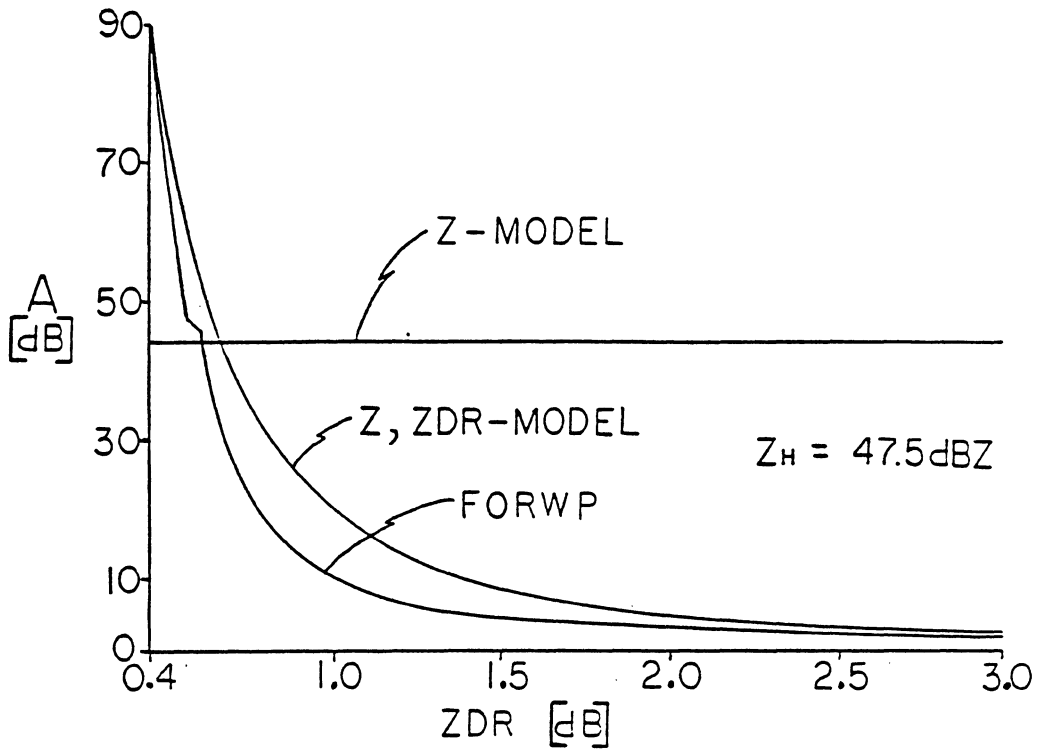

Figure 4.2.1-7 Predicted attenuation as a function of ZDR on a simulated link using three prediction models for $Z_H = 47.5dB(mm^6m^{-3})$

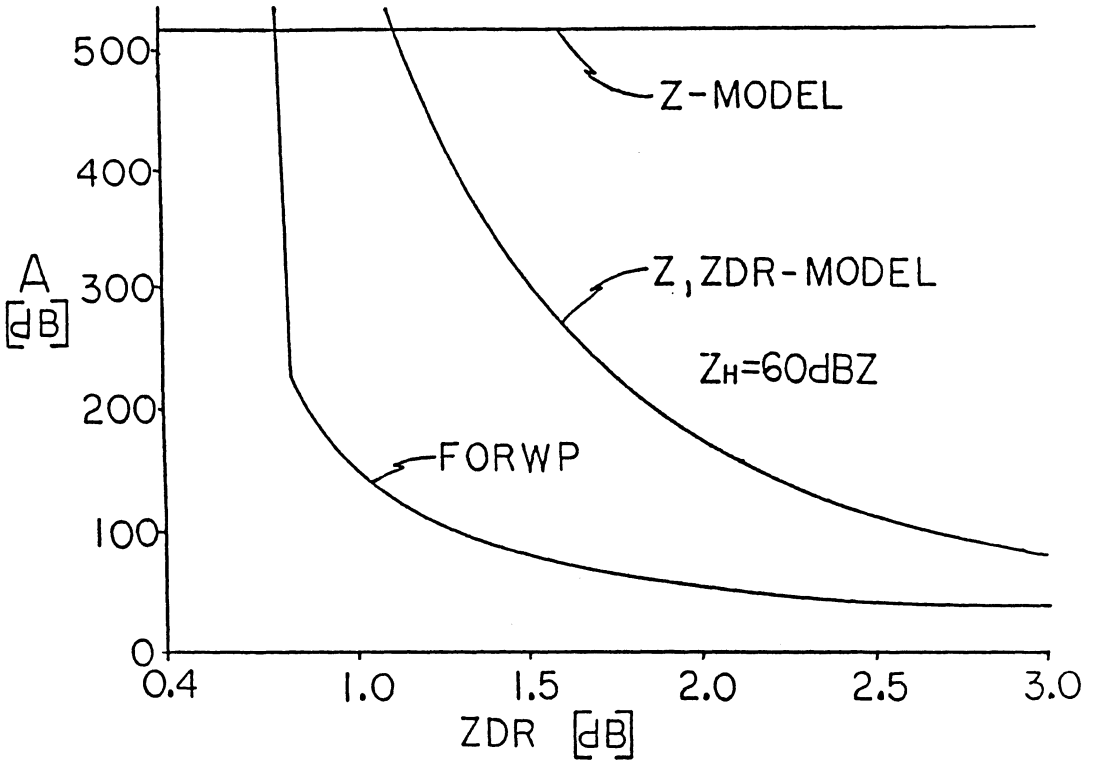

Figure 4.2.1-8 Predicted attenuation as a function of ZDR on a simulated link using three prediction models for $Z_H = 60.0dB(mm^6m^{-3})$

we can assume that Z_H and ZDR are constant along the length of the slant path, and (4.1-16) can be written in the following form:

$$A = L\,\alpha\, q_\mu^b\, Z_H^b\, ZDR^{-1.5b} \qquad (4.2.2-2)$$

where L is the length of the path, and α, q_μ, and b are defined in (4.1-16). Z_H has units of $[mm^6 m^{-3}]$, and ZDR is in [dB].

Combining (4.2.2-1) and (4.2.2-2) to eliminate A yields the relationship

$$XPD = U - V\log(L\alpha q_\mu^b) + Vb(1.5\log(ZDR) - \log(Z_H)) \qquad (4.2.2-3)$$

Equation (4.2.2-3) can be written in a more simplified form as

$$XPD = P + 22.4\,[1.5\log(ZDR) - Z_H/10] \qquad (4.2.2-4)$$

where ZDR and Z_H are in dB and P is a constant for a given path length. The above equation gives a simple relationship for evaluating the effects of Z_H and ZDR on XPD.

Figure 4.2.2-1 gives XPD as a function of Z_H for ZDR = 0.5 dB, 1.7 dB, and 2.3 dB. These curves indicate that XPD decreases almost linearly with Z_H. This linear decrease agrees with the linear relationship between XPD and Z_H indicated in (4.2.2-4).

Figure 4.2.2-1 also shows that ZDR increases with XPD. This relationship between XPD and ZDR also agrees with (4.2.2-4) which indicates that XPD increases with the log of ZDR [dB]. Figure 4.2.2-2 also shows XPD to increase nonlinearly with ZDR and confirms the relationship between XPD and ZDR in (4.2.2-4). It should be noted that (4.2.2-4) could be developed into a simple XPD model in the same manner the Z, ZDR-Model in (4.1-16) was developed.

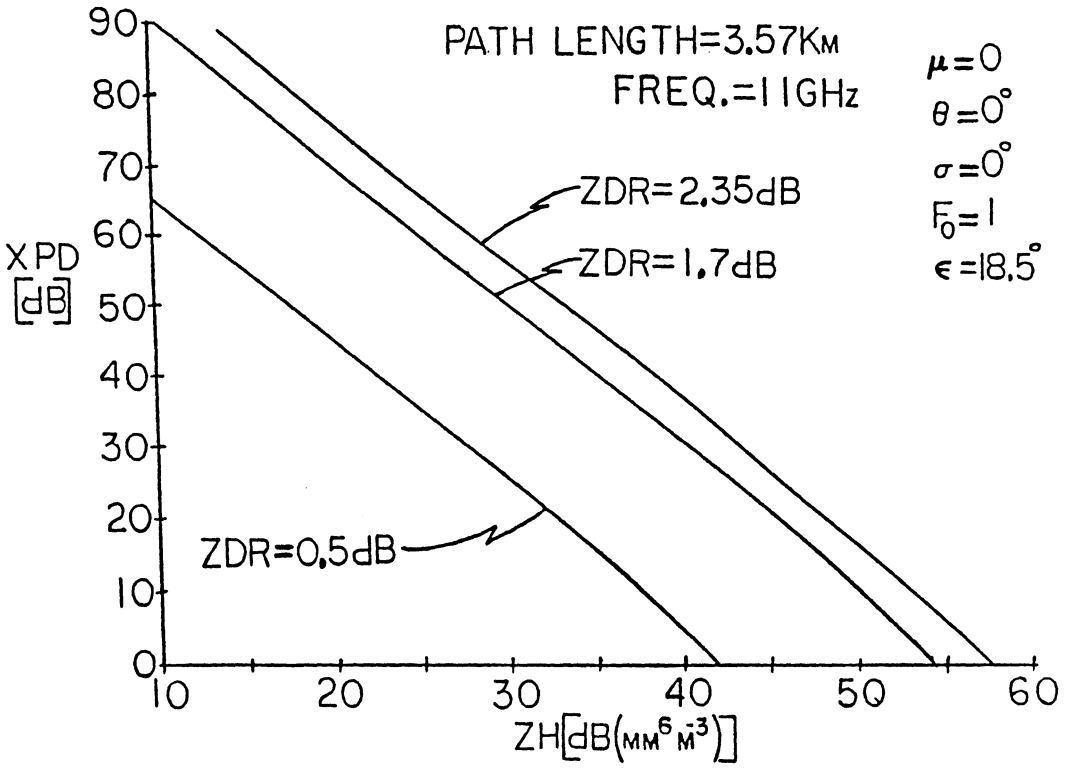

Figure 4.2.2-1 Predicted cross polarization as a function of Z_H on a simulated path by FORWP for ZDR = 0.5dB, 1.7dB, and 2.35dB

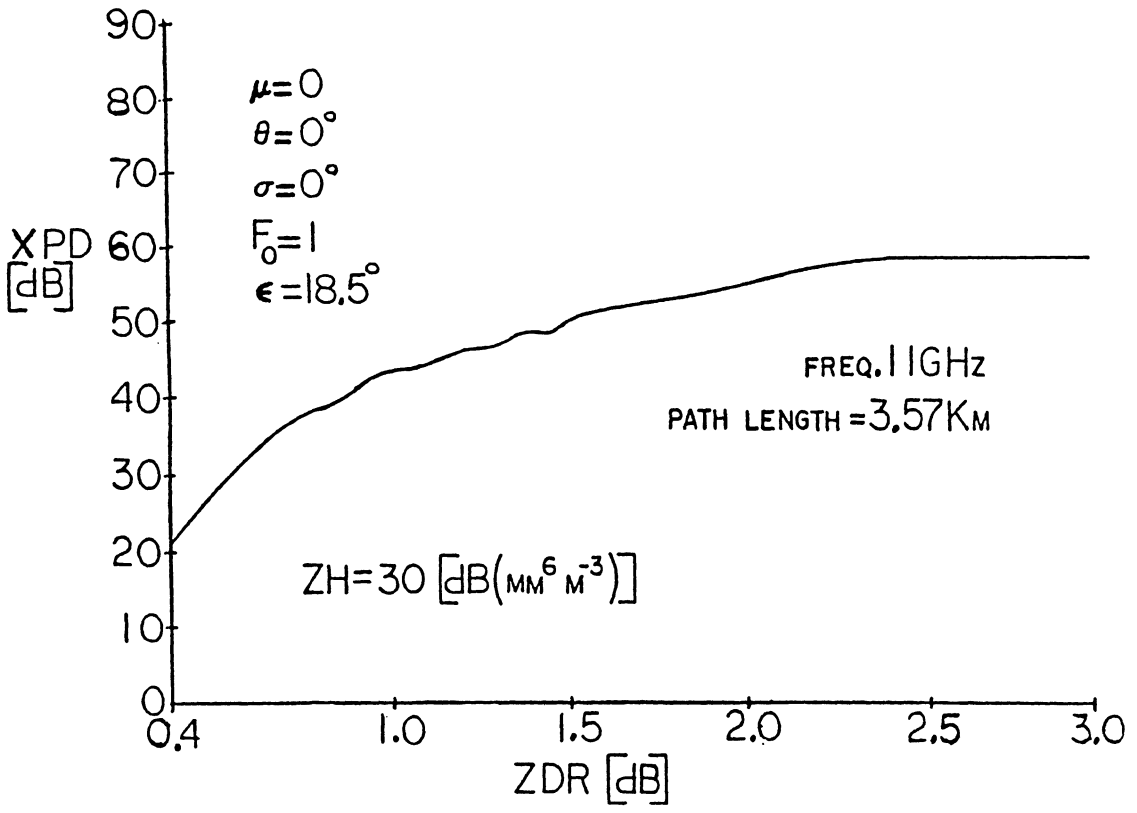

Figure 4.2.2-2 Predicted cross polarization as a function of ZDR on a simulated path by FORWP for Z_H =30dB (mm^6m^{-3})

4.3 A Parametric Investigation of FORWP

FORWP has six rain parameters and nine system parameters. The six rain parameters are associated with the physical characteristics of the rain medium in the path (see Section 2.7). The nine system parameters are associated with the polarization states of the communication link antennas (see Section 3.1). These various parameters afford FORWP considerable flexibility in modeling earth-space communication paths. Effects of these parameters on the BSCAT and MULTI portions of the FORWP prediction model have been studied by Stapor [1982] and by Runyon and Stutzman [1983], respectively. But the effects of these parameters on the combined prediction model FORWP had not been examined. Therefore we conducted an initial investigation of the effects of some of these parameters on the prediction characteristics of FORWP.

Of the nine system parameters, eight are antenna polarization state parameters, ε and τ, associated with the two transmit antennas and the two receive antennas of the dual channel communication link. For better quality antennas, polarization mismatch is a second order effect in this type of system [Stutzman, 1980]. Therefore we will assume perfect orthogonal circular polarization for the link antennas and not discuss the effects of antenna parameters in this work.

For a constant rain path length, FORWP will compensate for any change in elevation angle (ε) and cause the predictions of A and XPD to be independent of θ. Therefore, the effects of elevation angle will not be examined.

We test the effect of the remaining parameters μ, θ, σ, and F_o, on FORWP's predictions, by using the computer simulated path developed in Section 4.2. FORWP is applied to the simulated path, and then predicted A and XPD values are calculated as a function of Z_H for ZDR = 1.7dB or 2.3dB with various parameters values. The values of ZDR = 1.7dB and 2.35dB are used because many of the parameter effects are not noticeable at lower ZDR values.

4.3.1 The effect of μ on FORWP

Figure 4.3.1-1 shows the predictions of attenuation by FORWP on the simulated path as a function of Z_H for ZDR=2.35dB. Curves were generated for μ = 0, 2, and 5. These curves indicate that for Z_H greater than 50[dB (mm^6m^{-3})] the predicted attenuation increases slightly with μ. This increase in A with increasing μ can be explained by considering the rain medium used to construct the simulated test path (see Section 4.2). This medium produces a constant Z_H and ZDR along the path. In Section 2.7.3, it was shown that a medium with a constant Z_H or ZDR will yield a higher rain rate when μ is increased (see Figures 2.7.3-1 and 2.7.3-2). This increased rain rate will in turn produce higher attenuation. Therefore, predicted attenuation increases with μ.

It should be noted that preliminary investigation into the effect of μ on the prediction characteristics of FORWP have indicated some unexpected behavior when ZDR values are less than about 0.4dB. For very low ZDR values, the effect of increasing μ is to significantly decrease the predicted attenuation. This decrease may in part be due to the behavior of the Λ_μ versus ZDR cubic-spline curve fit (see Figure 2.3-1) near the lower limit of ZDR. Further investigation into the μ parameter is needed.

The prediction of XPD on the simulated test path as a function of Z_H for ZDR=2.3 dB and μ = 0 and 5 are shown in Figure 4.3.1-2. These curves indicate that the effect of increasing μ from 0 to 5 is to decrease the predicted XPD by nearly a constant across the range of the Z_H values shown. This decrease in XPD corresponds to the increase in predicted A shown in Figure 4.3.1-1. As μ increases, the rain rate increases; the attenuation increases, and the cross polarization decreases.

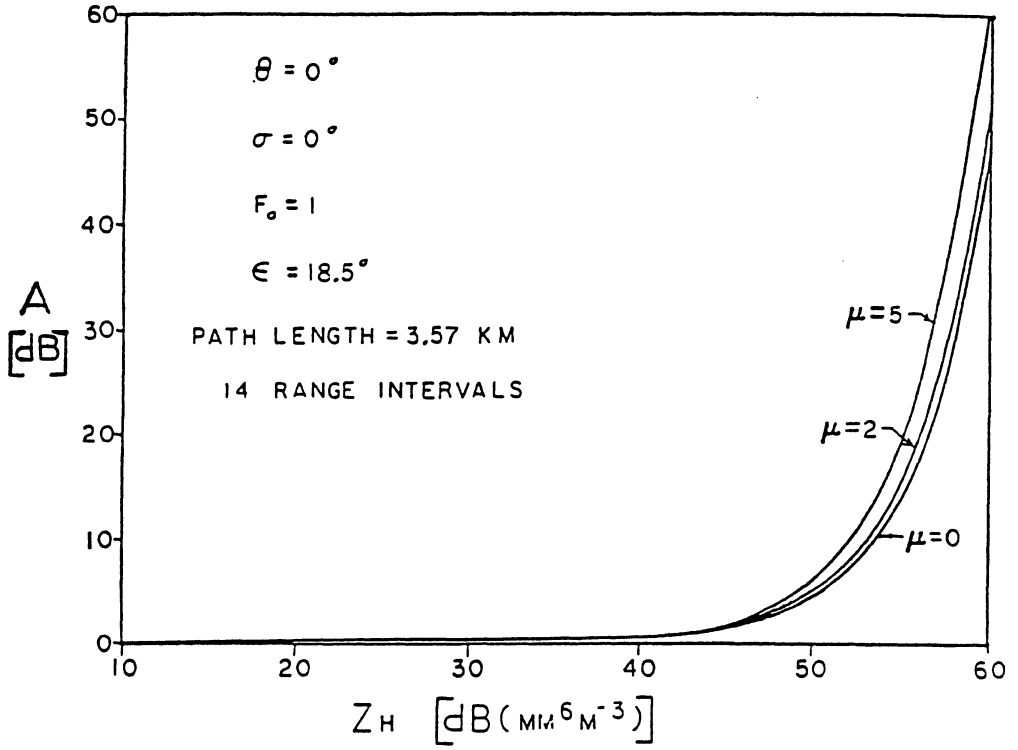

Figure 4.3.1-1 Predicted attenuation by FORWP on a simulated test path as a function of Z_H for ZDR=2.35dB and the drop size distribution parameter u=0, 2, and 5

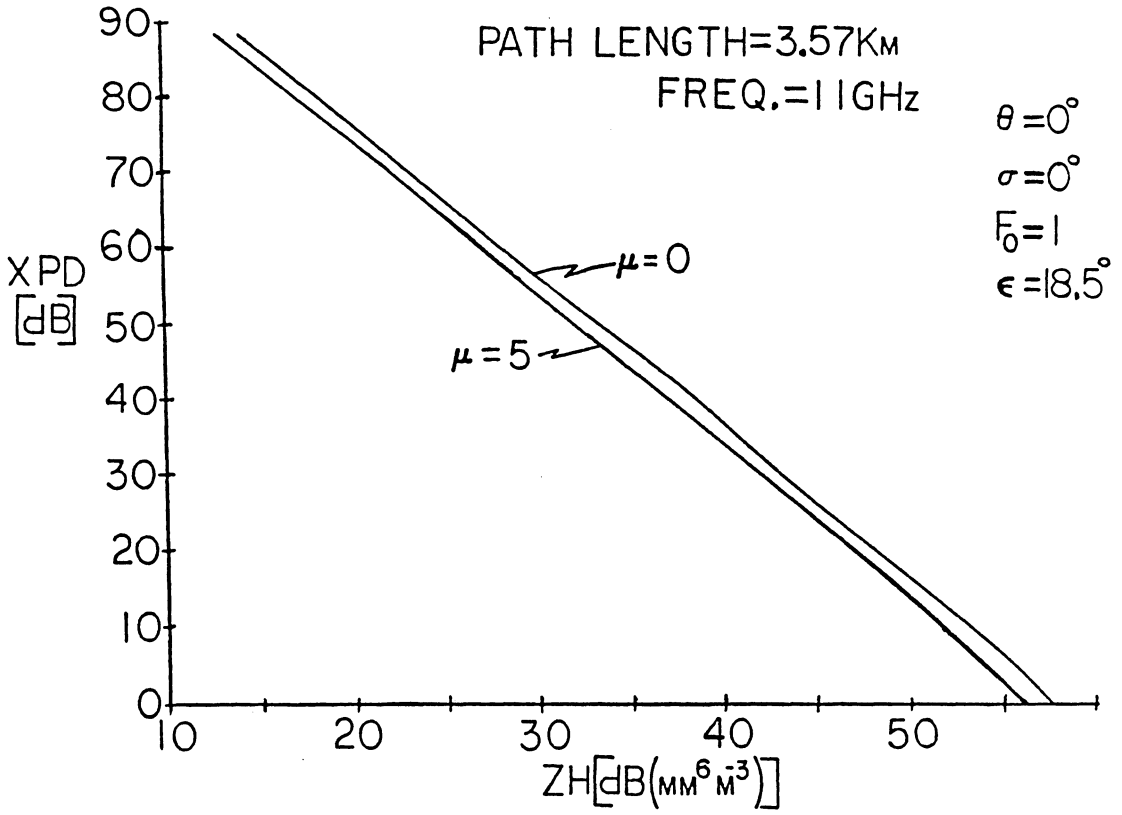

Figure 4.3.1-2 Predicted XPD by FORWP on a simulated test path as a function of Z_H for ZDR= 2.35dB and the drop size distribution parameter u=0, and 5

4.3.2 The effect of canting angle on FORWP

Figures 4.3.2-1 and 4.3.2-2 show the predictions of A and XPD by FORWP on the simulated path as a function of Z_H . The value of ZDR is 1.7dB, and curves are generated for $\theta = 0°$ and 15°.

The curves in Figure 4.3.2-1 indicate that the predicted A decreases for Z_H greater than about 45 dB(mm^6m^{-3}) when θ increases from 0° to 15°. For a ZDR = 1.7dB and a constant Z_H, increasing the average canting angle of the rain drops in the simulated path medium causes the effective cross sectional area of the rain drops , as seen by the linear dual-polarized radar, to increase. To compensate for the larger effective radar cross section of the rain drops, FORWP decreases the attenuation associated with a given Z_H , ZDR pair.

It should be noted that increasing the canting angle will decrease FORWP's prediction of A only when the canting angle is less than about 45° and the ZDR is less than about 1dB. As ZDR values decrease to zero, the effect of the canting angle diminishes.

The effect of increasing θ from 0° to 15° on the prediction of XPD by FORWP as a function of Z_H using the simulated path is shown in Figure 4.3.2-2. The predicted value of XPD increases by nearly a constant over the range of Z_H specified. The value of ZDR is 1.7dB. This increase in XPD corresponds to the decrease in A shown in Figure 4.3.2-1.

4.3.3 The effect of canting angle standard deviation on FORWP

The effect of increasing σ from 0° to 15° on the prediction of A and XPD by FORWP for ZDR = 1.7dB is nearly identical to the effect of increasing θ form 0° to 15°. The predicted

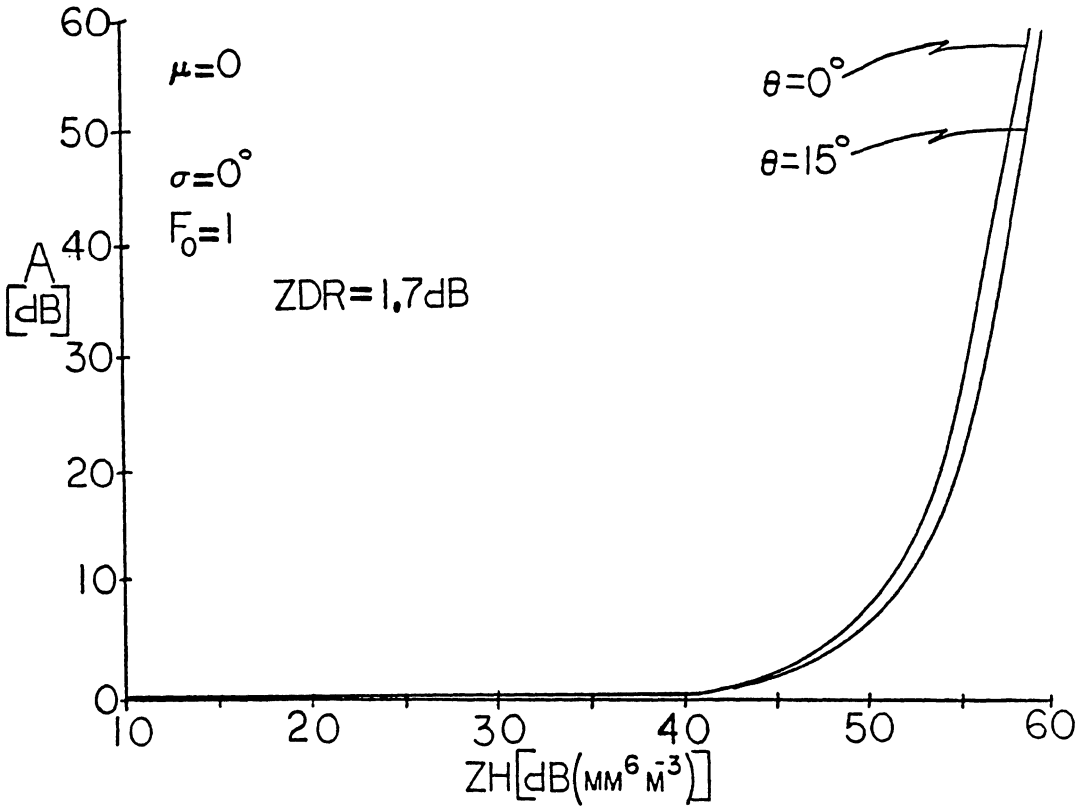

Figure 4.3.2-1 Predicted attenuation by FORWP on a simulated test path as a function of Z_H for ZDR = 1.7dB and the rain drop parameter $\theta = 0°$ and 15°

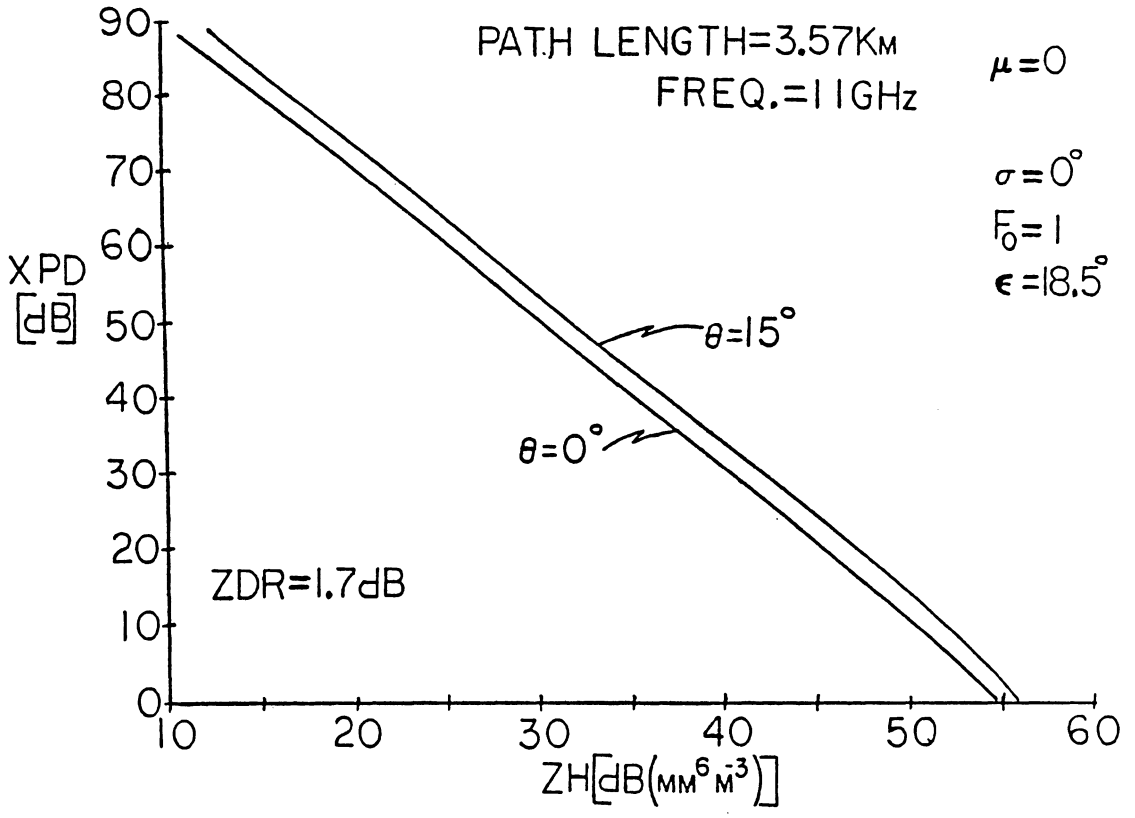

Figure 4.3.2-2 Predicted XPD by FORWP on a simulated test path as a function of Z_H for ZDR = 1.7dB and the rain drop parameter $\theta = 0°$ and 15°

values of A and XPD by FORWP as a function of Z_H for ZDR=1.7dB and θ=0° and 15° produced nearly identical curves to Figures 4.3.2-1 and 4.3.2-2.

The standard deviation of the canting angle (σ) determines how much the oblate rain drops, in the simulated path medium, oscillates about the mean canting angle. For a given Z_H and ZDR along the simulated path, an increase in σ causes the average effective cross-sectional area of the rain drops to appear larger to the dual-polarized radar. FORWP compensates for this larger cross sectional area by decreasing the predicted attenuation associated with a given Z_H, ZDR pair.

The effect of increasing σ from 0° to 15° on FORWP's predictions of XPD is nearly identical to the effect of increasing θ form 0° to 15° (see Figure 4.3.2-2). To evaluate the effect of σ on FORWP's we utilize the SIM model (Stutzman and Runyon[1984]) introduced in (4.2.2-1). The V coefficient in (4.2.2-1) is a constant and equals 19. The other coefficient (U) is a function of a variety of rain and system parameters. If we let f=11.0GHz, ε = 18.5°, θ = 0° and we assume circular polarized antennas, the U coefficient in (4.2.2-1) (see Equation (11) Stutzman and Runyon [1984]) becomes

$$U = 31.48 + 0.0053\,(\sigma^2) - 20\mathrm{Log}\,(F_o) \qquad (4.3.3-1)$$

where F_o is the fraction of oblate drops. Using (4.3.3-1) and (4.2.2-1), (4.2.2-2) can be written in the form

$$XPD = 31.48 + 0.0053\,(\sigma^2) \qquad (4.3.3-2)$$

$$- 20\mathrm{Log}\,(F_o) + 19\,\mathrm{Log}\,(aLq_\mu\, Z_H^b\, ZDR^{-15b})$$

where a, L, q_μ, and b are constants defined in (4.2.2-2). Equation (4.3.3-2) shows that XPD increases with σ.

4.3.4 The Effect of F_o on FORWP

Figures 4.3.4-1 and 4.3.4-2 show the predictions of A and XPD by FORWP as a function of Z_H for ZDR = 1.7dB and F_o = 1 and 0.6.

The curves in Figure 4.3.4-1 show that the predicted values of A decrease for Z_H greater than about 40dB (mm^6m^{-3}) when F_o is decreased from 1.0 to 0.6. The decrease in predicted attenuation becomes very large for Z_H values greater than about 52 dB(mm^6m^{-3}).

The effect of decreasing F_o from 1.0 to 0.6 on the prediction of XPD by FORWP for ZDR=1.7dB is shown in Figure 4.3.4-2. These curves indicate that XPD increases by nearly a constant over the range of Z_H values used in the figure. This increase in XPD corresponds to the decrease in A indicated in Figure 4.3.4-1.

The relationship in (4.3.3-3) also indicates that XPD increases with F_o. Using the (4.3.3-3) to calculate the change in XPD as F_o increases from 0.6 to 1.0 indicates a 4.43 dB decrease in the value of XPD. This increase is independent of Z_H and ZDR. Equation (4.3.3-3) confirms the relationship indicated by the curves in Figure 4.3.4-1.

4.4 Comparison of Predicted and Measured Attenuation

For the final evaluation of the FORWP prediction model, this section gives a comparison between measured and predicted link attenuation from a real rain event on April 15, 1986.

At 3:40 PM eastern standard time, the leading edge of the storm cell (event) passed through our local and diversity satellite link paths. The total time of significant attenuation (above 1 dB) was about 100 minutes. The attenuation on the links was measured and stored on computer at asynchronous time intervals during the event. This produced approximately 300 measured link attenuation values. At the same time each measured attenuation value was

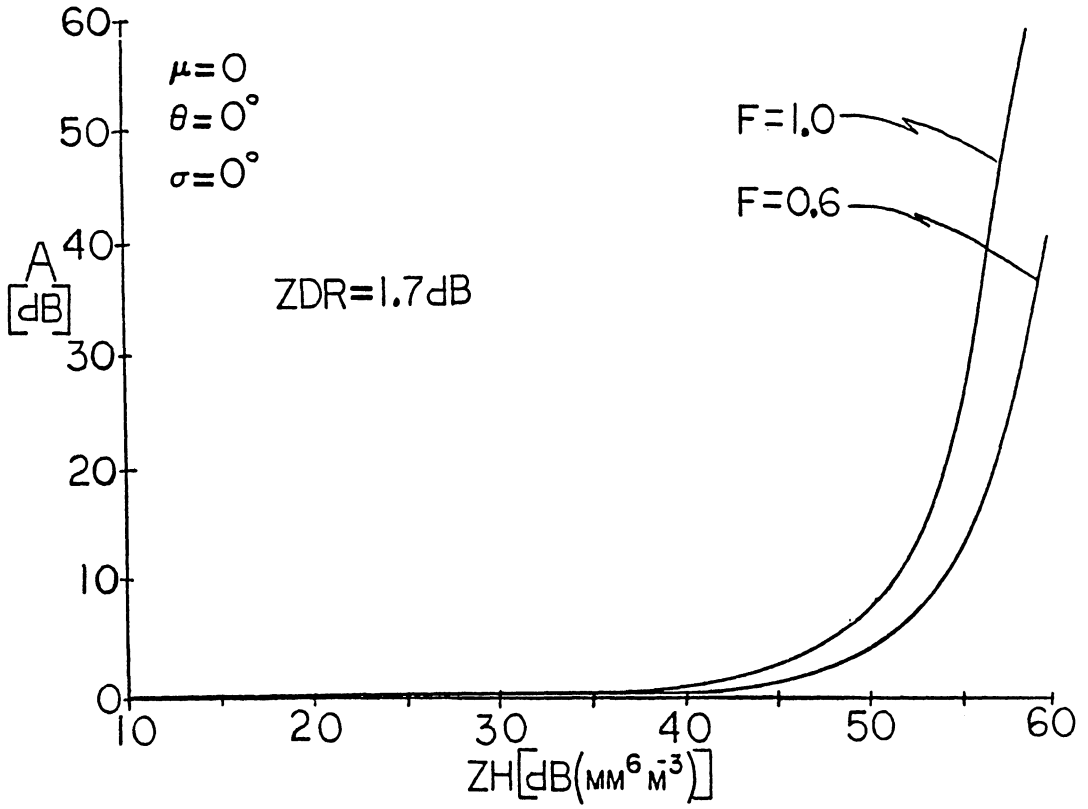

Figure 4.3.4-1 Predicted attenuation by FORWP on a simulated test path as a function of Z_H for ZDR = 1.7dB and the rain drop parameter F_O = 1.0 and 0.6

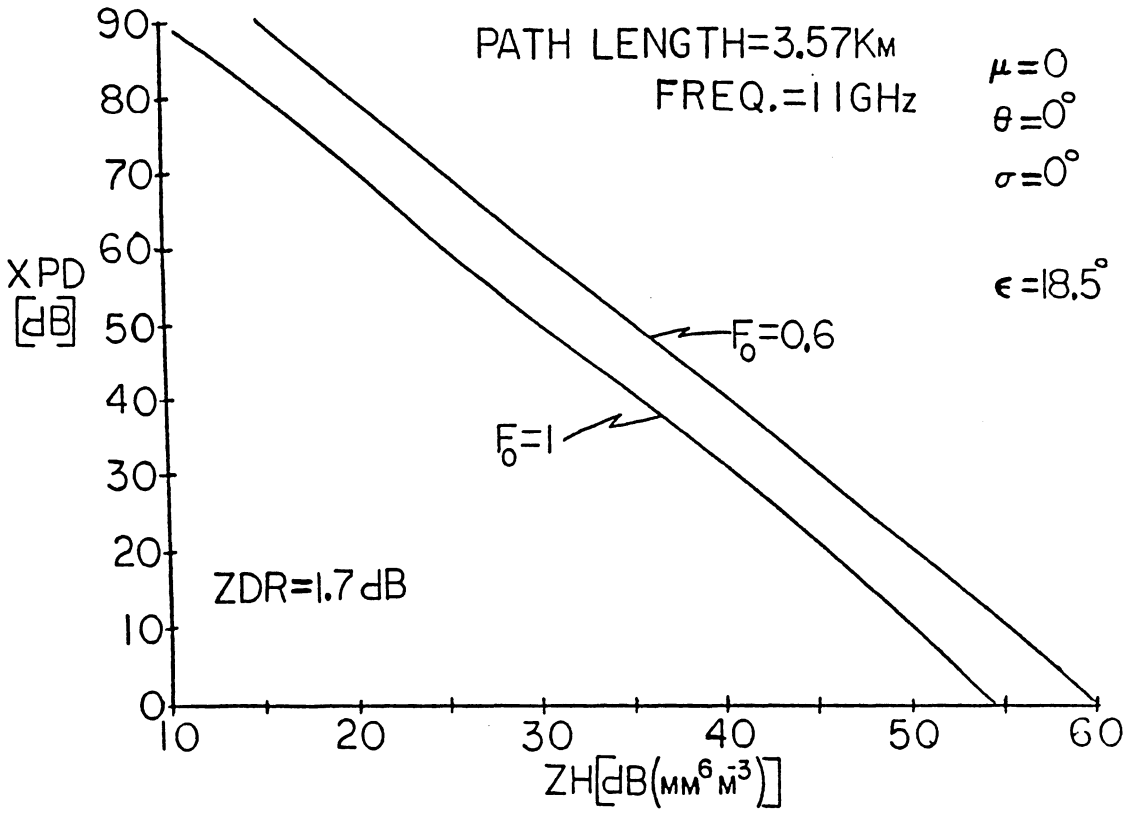

Figure 4.3.4-2 Predicted XPD by FORWP on a simulated test path as a function of Z_H for ZDR = 1.7dB and the rain drop parameter F_0 = 1.0 and 0.6

collected, the radar scanned the satellite path. The radar data generated from the path scans were processed through the three prediction models to predict attenuation values corresponding in time with the collected link attenuation values. The slant path length used in this event was 1.13 km and corresponded to the average range of the middle of the Z_H bright band.

The initial prediction attempt using FORWP and the Z, ZDR-Model produced gross over estimates of link attenuation by about a factor of about 40. But the Z-Model agreed fairly well with measured link attenuation values. This over prediction by FORWP and the Z, ZDR-Model was found to be associated with low ZDR values. In Section 4.2 it was shown that both these models have an inverse relationship between attenuation and ZDR. Therefore when ZDR approaches zero, the predicted attenuation becomes very large (see Figures 4.2.1-6 through 4.2.1-8). Due to the statistical nature of rain, low to moderate Z_H values often produce ZDR values at or near zero. Therefore, only one measured ZDR value near zero would cause FORWP or the Z, ZDR-Model to grossly over predict for the entire link.

The sensitivity of FORWP and the Z, ZDR-Model to low ZDR values makes the measurement of lower ZDR values critical. But measuring low ZDR values accurately is difficult. Due to the statistical nature of backscattering from rain, ZDR values represent random variables and therefore cannot be measured exactly. Also, the cross polarization isolation of the antenna and polarizer in the radar is not large, leading to measurement error for low ZDR values.

To compensate for the sensitivity of FORWP and the Z, ZDR-Model to low ZDR values, we set a floor on ZDR of 0.5 dB. In other words, the measured ZDR values below 0.5dB are set to 0.5 dB.

4.4.1 ZDR Floor of 0.5dB

Next, the April 15, 1986 data was processed again for the local path with the three prediction models using the 0.5 dB floor on ZDR. Figures 4.4.1-1, 4.4.1-2, and 4.4.1-3 show the prediction results. The parameter values used as input to FORWP were as follows: $F_o = 1$, $\theta = 0°$, $\sigma = 0°$, and $\mu = 0$. FORWP produced the best over all agreement between measured and predicted attenuation. The Z, ZDR-Model agrees fairly closely with FORWP and produced better over all predictions than the Z-Model. FORWP and the Z, ZDR-Model both generally over predicts for attenuation less than about 1.2 dB and under predicts for attenuation greater than 1.2 dB. The Z-Model generally over predict for attenuation greater than about 1 dB and under predict for attenuation less than 1 dB.

The Z-Model produces excellent predictions when the attenuation is less than about 1.2 dB. Since low ZDR and Z_H values are associated with low attenuation, this result indicates that ZDR is not required to predict attenuation when Z_H and ZDR are small. This is in agreement with the study conducted in Section 4.2.

4.4.2 Power Law Correction For Low ZDR

To produce a better prediction model we modified FORWP and Z, ZDR-Model for low attenuations. This was accomplished by comparing the Z-Model with the Z, ZDR-Model and deriving an analytical expression relating ZDR to Z_H which we shall discuss shortly. Then this expression was used, when ZDR $<$ 0.5 dB or $Z_H \leq$ 2.5 dB (mm^6m^{-3}), to generate ZDR values from measured Z_H values. These ZDR values were then used in place of the measured ZDR values in the Z, ZDR-Model and FORWP. We developed the ZDR, Z_H expression by equating the rain rate expression developed separately for the Z-Model and the Z, ZDR-Model given in

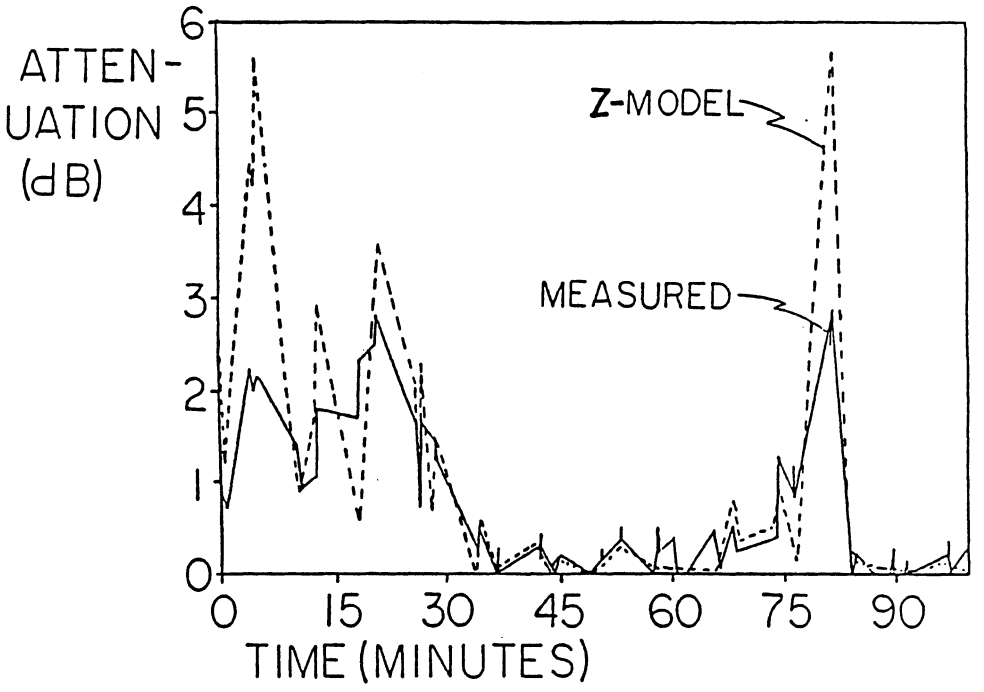

Figure 4.4.1-1 The Prediction of attenuation by Z-Model (dotted line) as a function of time and compared against measured link attenuation (solid line) for an event on April 15, 1986 along the Local Path

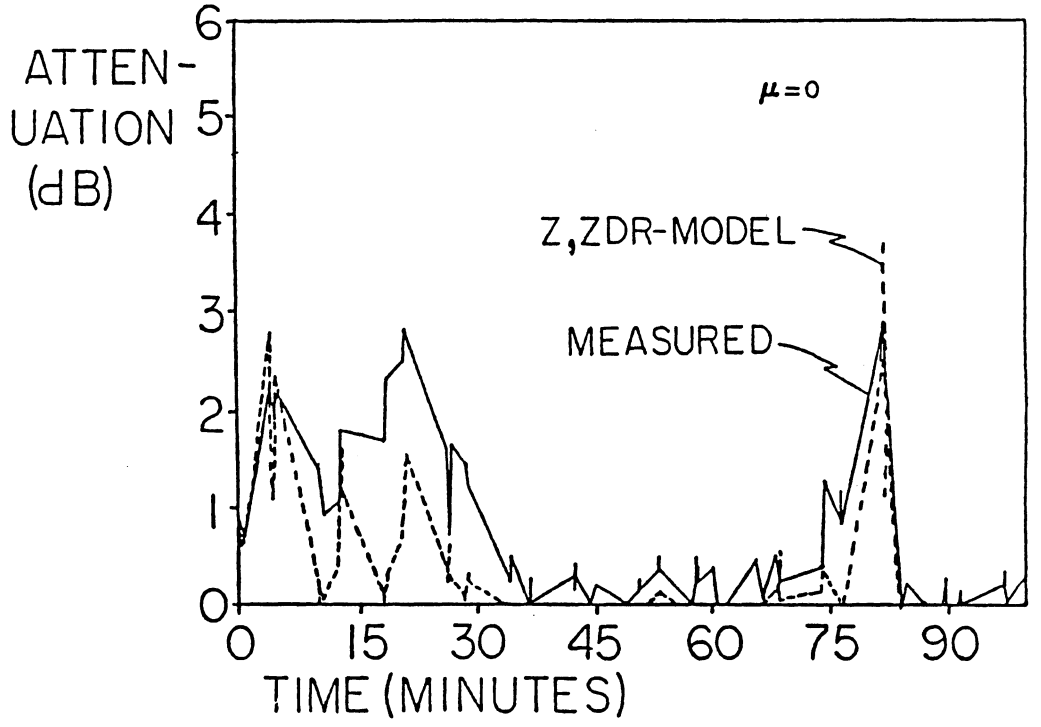

Figure 4.4.1-2 The Prediction of attenuation by Z, ZDR-Model (dotted line) as a function of time and compared against measured link attenuation (solid line) for an event on April 15, 1986 along the Local Path using a 0.5dB floor on ZDR

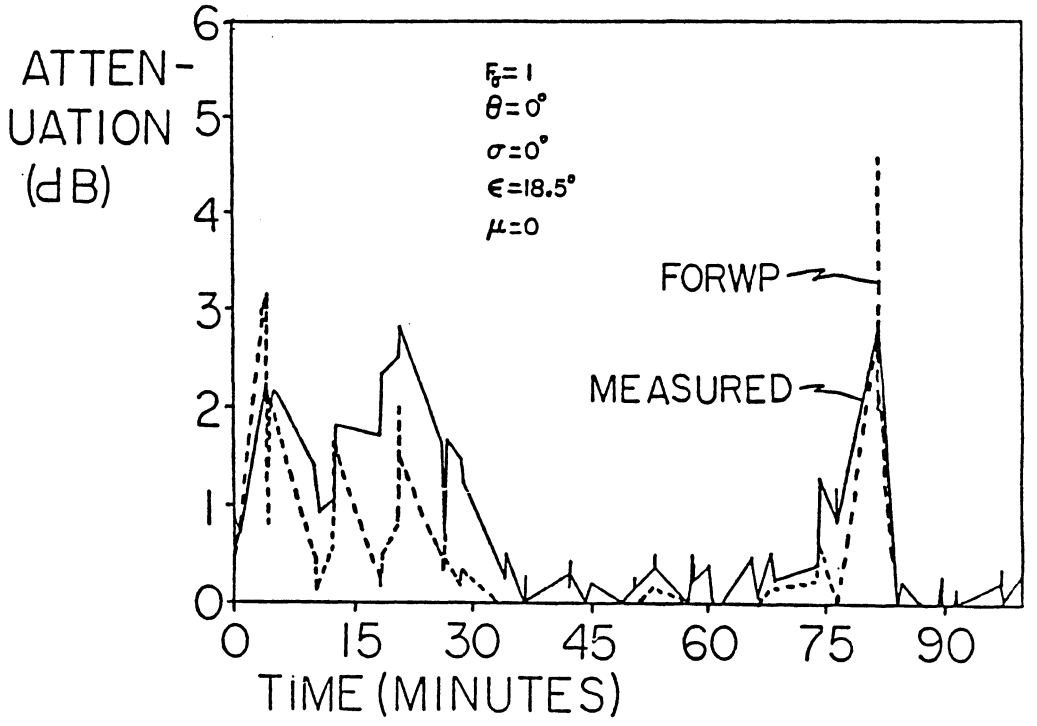

Figure 4.4.1-3 The Prediction of attenuation by FORWP (dotted line) as a function of time and compared against measured link attenuation (solid line) for an event on April 15, 1986 along the Local Path using a 0.5dB floor on ZDR

(4.1-10) and (4.1-11), respectively. Of course, rain rate is directly related to attenuation and therefore in equating predicted rain rates we are essentially forcing the predicted attenuations to be equal. Equating the rain rate equations (4.1-10) and (4.1-11), we produced the following ZDR, Z_H relationship:

$$ZDR = q_\mu Z_H^{0.1972} \text{ [dB]} \qquad (4.4.2 - 1)$$

where $q_o = 0.0155$ ($\mu = 0$), and $q_2 = 0.006713$ ($\mu = 2$)

To evaluate the relationship developed in (4.4.2-1), we reprocessed the radar data from the April 15, 1986 event for the local path. Each radar data pair was modified such that when ZDR was less than 0.5dB the measured ZDR value was replaced with a ZDR value calculated from (4.4.2-1). Figures 4.4.2-1 and 4.4.2-2 give the reproduced attenuation predictions by FORWP and the Z, ZDR-Model for the local path. Z-Model was not used to reprocess the radar data since this model is independent of ZDR and would produce the same results as shown in Figure 4.4.1-1.

The use of (4.4.2-1) to replace measured ZDR values less than 0.5dB instead of using a 0.5dB floor caused predicted attenuation values of Z, ZDR-Model and FORWP to decrease when compared against measured values above about 2dB. The prediction of A values below about 1dB by Z, ZDR-Model on the local path showed little difference whether a 0.5dB floor was used or if (4.4.2-1) was used on ZDR values less than 0.5dB. It should be noted that FORWP's predictions of A for measured value less than about 1dB increase when (4.4.2-1) was used instead of the 0.5dB floor.

Further work is needed to determine the optimal ZDR level below which the relationship in (4.4.2-1) should be used. Initial investigations indicated that when the ZDR level, at which (4.4.2-1) was used to correct for poor ZDR, was drop below 0.5dB the predicted values of A by FORWP and Z, ZDR-Model increased.

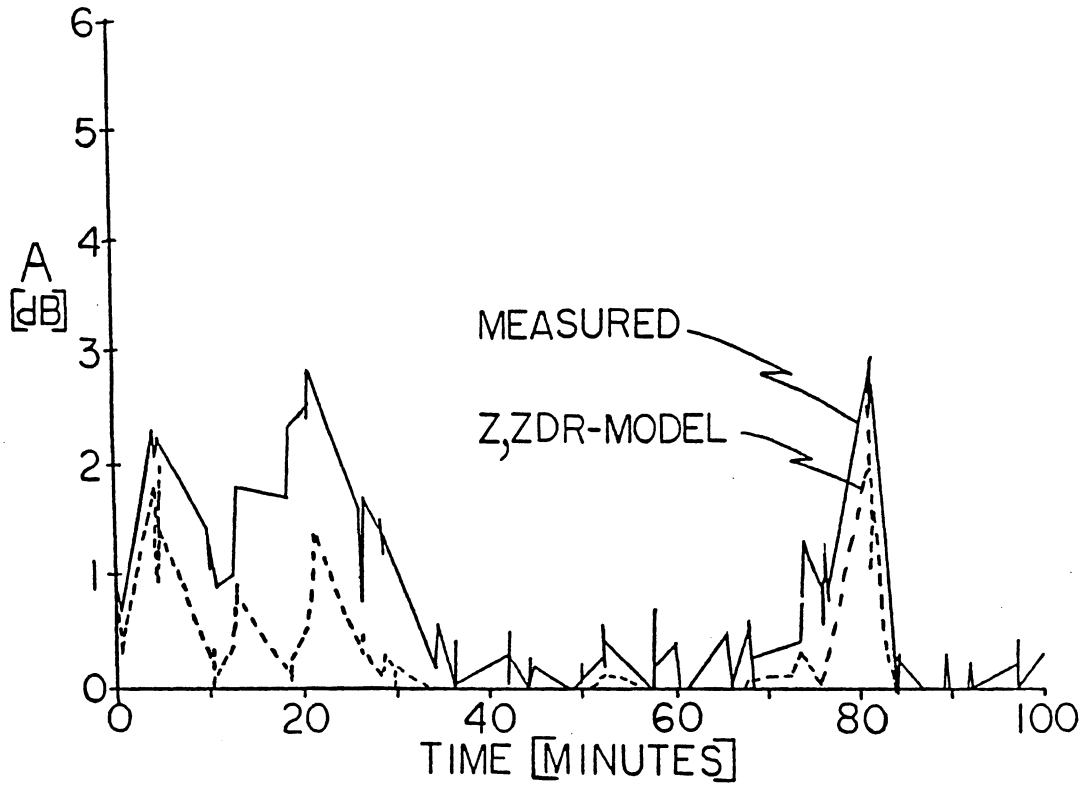

Figure 4.4.2-1 The Prediction of attenuation by Z, ZDR-Model (dotted line) as a function of time and compared against measured link attenuation (solid line) for an event on April 15, 1986 along the Local Path using (4.4.2-1) to replace measured ZDR values below 0.5dB

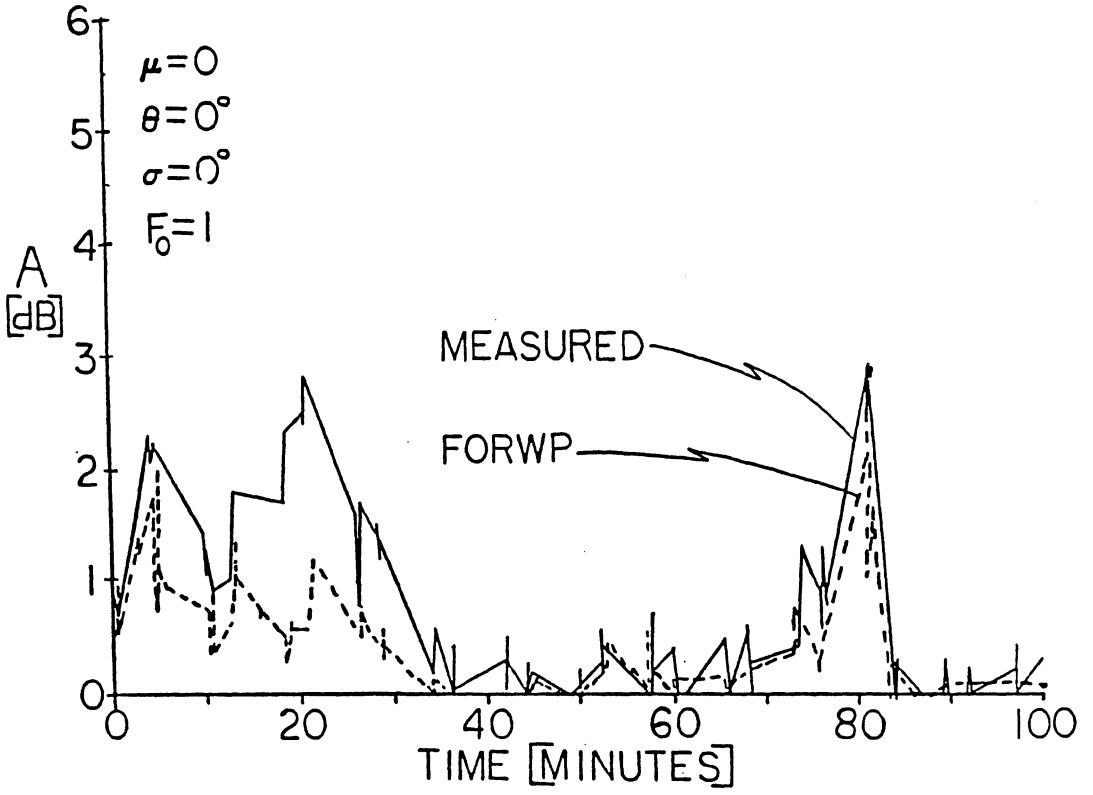

Figure 4.4.2-2 The Prediction of attenuation by FORWP (dotted line) as a function of time and compared against measured link attenuation (solid line) for an event on April 15, 1986 along the Local Path using (4.4.2-1) to replace measured ZDR values below 0.5dB

4.4.3 Diversity Path Predictions

Next we processed the radar data for the diversity site link on the April 15, 1986 event. The rain path length was about 1.13km and was nearly the as the local path. The relationship in (4.4.2-1) was used to replace measured ZDR values below 0.5dB.

Figure 4.4.3-1 through 4.4.3-3 give the predicted attenuation curves of Z-Model, Z, ZDR-Model, and FORWP. The Z-Model (Figure 4.4.3-1) generally overestimates measured attenuation for value above 1dB. But, the Z-Model produces reasonable agreement with measured A values less than about 1dB.

Z, ZDR-model (Figure 4.4.3-1) produces reasonable agreement with measured attenuation values. Z, ZDR-Model slightly underestimates measured A values less than about 1dB. FORWP (Figure 4.4.3-1) constantly over estimates measured attenuation. FORWP produces better agreement with measured attenuation than the Z-Model for values above about 1dB. The best prediction of attenuation by the three models for the diversity path event was the Z, ZDR-Model.

4.4.4 Comparison of Local and Diversity Path Attenuation Predictions

Next we compared the attenuation predictions of the three prediction models for the local and diversity paths on the April 15, 1986 event. Since the diversity path measured attenuation never exceeded 1.5dB, we are limited to comparing predicted attenuation values of less than 1.5dB for the two paths. To compare the prediction on the two paths, we used the

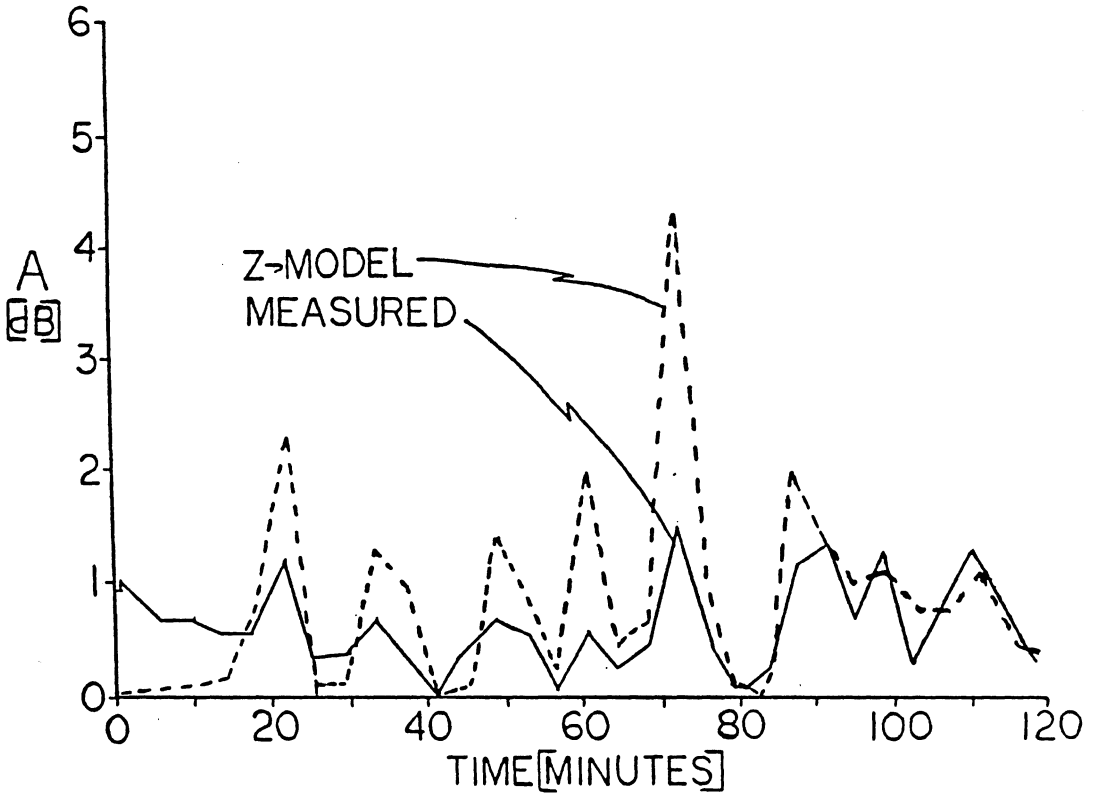

Figure 4.4.3-1 The Prediction of attenuation by Z-Model (dotted line) as a function of time and compared against measured link attenuation (solid line) for an event on April 15, 1986 along the Diversity Path

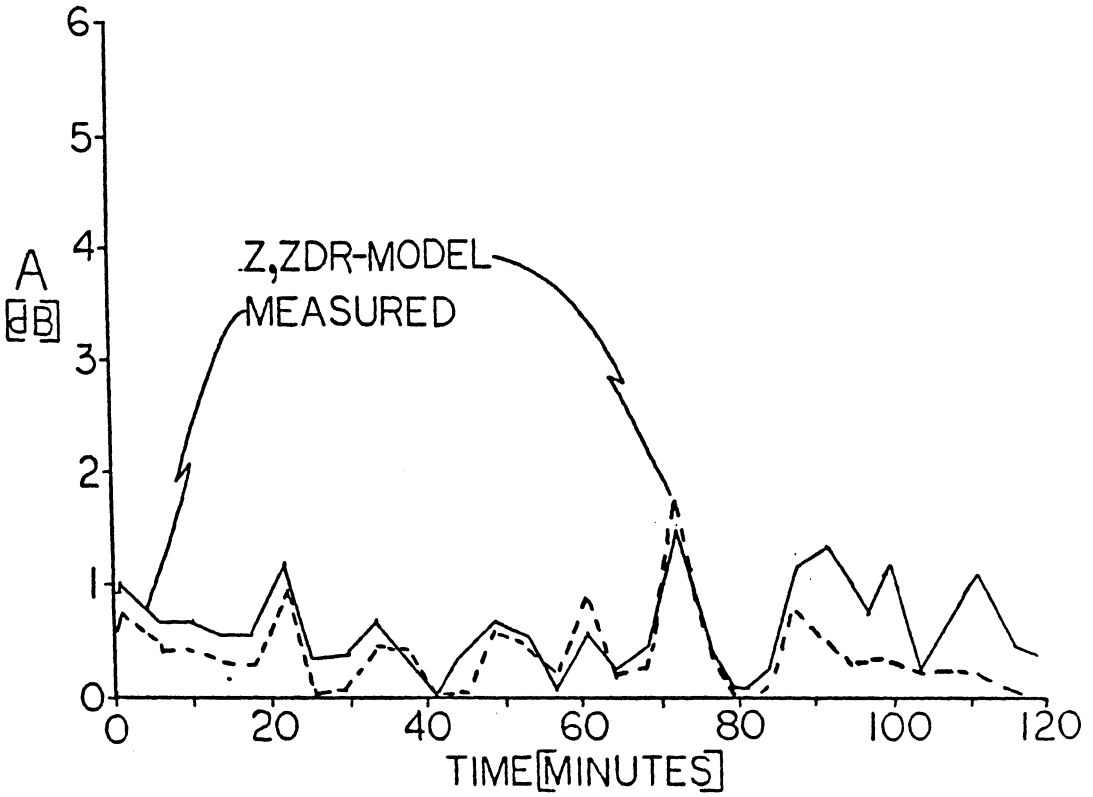

Figure 4.4.3-2 The Prediction of attenuation by Z,ZDR-Model (dotted line) as a function of time and compared against measured link attenuation (solid line) for an event on April 15, 1986 along the Diversity Path using (4.4.2-1) to replace measured ZDR values below 0.5dB

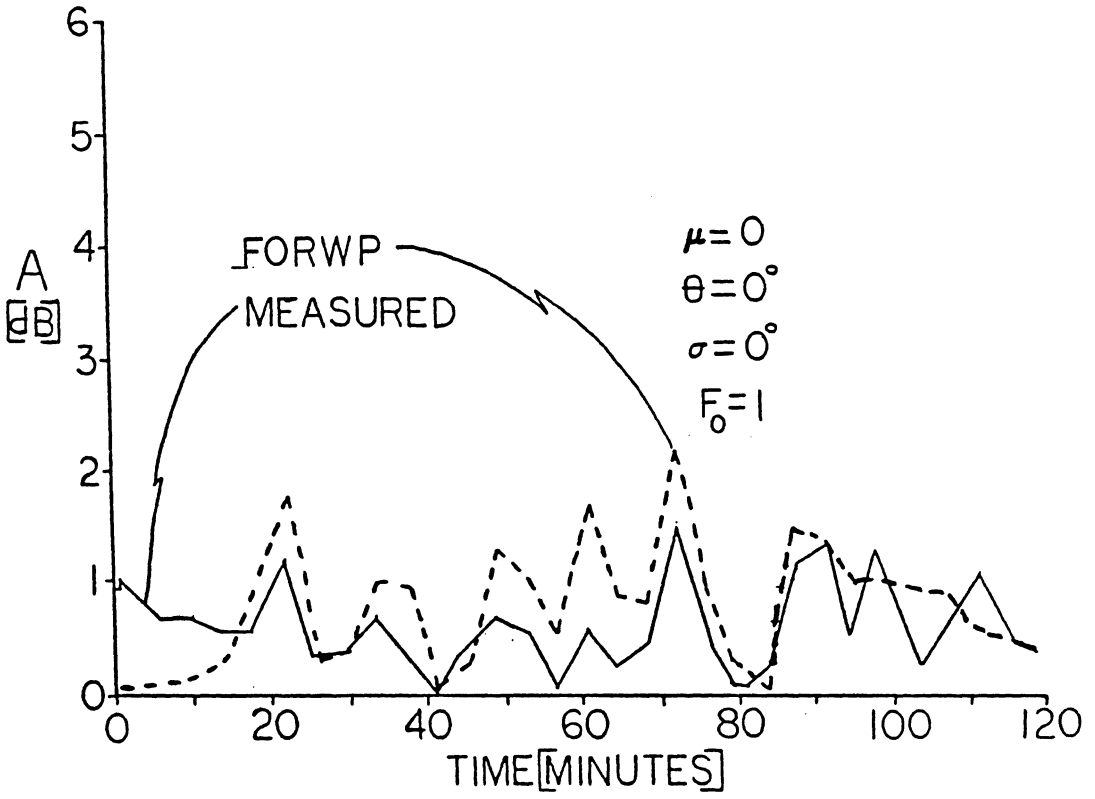

Figure 4.4.3-3 The Prediction of attenuation by FORWP (dotted line) as a function of time and compared against measured link attenuation (solid line) for an event on April 15, 1986 along the Diversity Path using (4.4.2-1) to replace measured ZDR values below 0.5dB

ZDR power law correction on measured ZDR values less than 0.5dB for both the local and diversity paths.

A comparison of the curves shown in Figure 4.4.1-1 with the predictions in Figure 4.4.3-1 indicates that the Z-Model produced similar predictions for the two path for attenuation values less than 1.5dB with the diversity path prediction giving slightly higher values.

The attenuation predictions of Z,ZDR-Model, and FORWP on the local path (see Figures 4.4.2-1 and 4.4.2-2) compared with their diversity path predictions (see Figures 4.4.3-1 and 4.4.3.-2) show that these models produced significantly better agreement with measured attenuation values for the diversity path than the local path. Both model generally under estimated for measurd values less than about 1.2dB. The superior prediction of attenuation for the two models on the diversity path may in part be due to the two different methods by which the radar scans the local and diversity paths (see Section 1.2.3). The radar probes the local path by aligning the axis of its antenna with the center of the propagation path (see Figure 1.2.3-1 and 1.2.3-2). The radar scans the diversity path by sweeping its antenna beam along the length of the path (see Figure 1.2.3-1).

Another factor that may cause the diversity path to produce better predictions is that the data for the first two range gates (510m) along the local path can not be collected. Under our present processing scheme, the radar data from the third range gate is used to process the first two range gates. If a different rain distribution exists in the third range gate than in the first two the prediction results will be biased.

Chapter 5 Summary and Conclusion

5.1 Overview of Thesis

A one-year propagation experiment investigated the use of multi-polarized radar for predicting satellite link path attenuation. The research included a comparison of measured link attenuation with attenuation predicted from radar measurement. A rigorous computer scattering model, FORWP, was used to perform the predictions of attenuation from dual-polarized radar data. FORWP was constructed from a backscattering computer model (BSCAT) and a forward multiple scattering computer model (MULTI). This thesis presented the development of FORWP and its initial prediction results from the experiment.

5.2 Summary of Chapter 1 - The Experiment and FORWP

The set up and operation of the experiment was review in Chapter 1. Also the procedures for collecting, processing, and anlayzing data was explained. Additionally, Chapter 1 described the operation and logic flow of the FORWP program.

5.3 Summary of Chapter 2 - The Prediction of Rain Characteristics

The BSCAT portion of FORWP was developed from Rayleigh backscattering theory using oblate spherical rain drops. BSCAT uses a cubic spline curve fit procedure for calculating the DSD parameters N_μ and Λ_μ from Z_H and ZDR. The cubic splines accurately calculate N_μ and Λ_μ for any combination of system and rain parameters.

Chapter 2 includes evaluation of the effects of the DSD parameter μ on BSCAT. This was done by comparing predicted rain rate values derived from BSCAT for a range of Z_H and ZDR values with $\mu = 0$, 2, and 5. The resulting effect of μ on BSCAT was that as μ increased the predicted rain rate increased.

Next, Chapter 2 discussed and outlined a procedure for comparing radar and distrometer-derived Z_H, ZDR, and rainrate values. It was proposed that the comparison of a large data base of radar and distrometer-derived Z_H values could produce better calibration of the radar than a metal sphere. Then it was indicated that the comparison of radar and distrometer derived ZDR values could provide insight into selecting the rain parameters F_0, θ, and σ. Finally the comparison of radar and disdrometer predicted rain rates was shown to be useful in the selection of the DSD parameter μ.

5.4 Summary of Chapter 3 - Forward Multiple Scattering

The MULTI portion of FORWP was developed from forward multiple scattering theory. MULTI predicted A and XPD at 10-30 GHz from DSD information.

The effect of the DSD parameter μ on MULTI was investigated. To test MULTI, a computer simulated slant path was constructed. The path had a constant rain rate up to 4 km. MULTI predicted A and XPD from the simulated path over a range of rain rates. At a given rain rate, the median drop size was held constant. Finally as μ increased, MULTI indicated a slight decrease in predicted A and a slight increase in predicted XPD.

5.5 Summary of Chapter 4 - The Evaluaton of FORWP 11.4GHZ

FORWP was evaluated by comparing it with two simple semi-empirical prediction models at 11.4 GHz. The first simple model (Z-Model) predicted A solely from Z_H values. The second semi-empirical model (Z, ZDR-Model) predicted A from both Z_H and ZDR values. The comparison of the three prediction models indicated that FORWP agreed well with the Z, ZDR-Model over a wide range of Z_H and ZDR values with $F_0 = 1, \theta = 0°, \sigma = 0°$, and $\mu = 0$. FORWP also agreed well with the Z-Model for Z_H less than about 25 dB (mm^6m^{-3}). But, the Z-Model over-predicted FORWP for higher Z_H values.

As a final test of FORWP, this work compared predictions of FORWP, Z-Model, and Z, ZDR-Model against measured link attenuation at 11.4 GHz for a rain event on April 15, 1986. The parameters of FORWP were set to: $F_0 = 1, \theta = 0°, \sigma = 0°$, and $\mu = 0°$. This comparison indicated that Z-Model produced good agreement with measured link A for $A \leq 1.5$ dB. But,

FORWP and the Z, ZDR-Model significantly over predicted measured A. This over prediction of A was due to the sensitivity of FORWP and Z, ZDR-Model to low ZDR values. It was also concluded that the OCTOPOD radar system could not accurately measure ZDR below about 0.5 dB.

Initially we compensated for the sensitivity to low ZDR and the inaccuracy in measuring it by setting a 0.5dB floor on ZDR. We replaced all measured ZDR values below 0.5 dB with a value of 0.5 dB. After compensation for low ZDR with a 0.5 dB floor, FORWP and Z, ZDR-Model produced good agreement with measured link A greater than about 1.5 dB but under predicted measured A values below 1.5 dB.

Next we derived another method for compensating for low ZDR values. When the measured ZDR values were less than 0.5 dB, we replaced them with analytical ZDR values. A power law relationship was developed to calculate an analytical ZDR value from the corresponding Z_H value. After adjusting low ZDR values with the power low relationship, the FORWP and Z, ZDR-Model produced good agreement with measured link A for A less than about 2.0 dB. But, FORWP and the Z, ZDR-Model under predicted measured A values greater than about 2.0 dB.

5.6 *Summary of Major Results*

The FORWP computer model predictions of attenuation from radar measured Z_H and ZDR produced good agreement with measured link attenuation. The results of FORWP were also compared with two semi-empirical models (Z-Model and Z, ZDR-Models) and showed very close agreement with the Z, ZDR-Model and agreed well with the Z-Model when Z_H was less than about 25 dB (mm^6m^{-3}). Because of the agreement of the FORWP predictions with the two semi-empirical models and measured link attenuation, we conclude that FORWP was properly derived from backward and forward multiple scattering theory and that FORWP was

successfully coded into a Fortran program. Also, the agreement between measured attenuation and the results of FORWP indicates that the experiment with its associated radar, computers, software, and hardware was designed, constructed, and operated correctly.

FORWP and the Z, ZDR-Model showed a strong sensitivity to low ZDR values. This sensitivity to low ZDR was due to an inverse relationship between attenuation and ZDR that results in large predicted attenuations for ZDR values near zero.

The Z-Model, which predicts attenuation independently of ZDR, produced good agreement with measured attenuation values for values less than about 1.5 dB. Attenuation values below 1.5 dB are associated with low rain rates, therefore the results of the Z-Model indicate that the accurate prediction of attenuation of low rain rates does not require the use of ZDR. Also since the radar cannot accurately measure ZDR below 0.5 dB, any information provided by low ZDR values is not reliable.

5.7 *Discussion of Future Work*

5.7.1 Attenuation at Higher Frequencies

The ability of FORWP to predict A at frequencies up to 30 GHz will be the subject of further studies. The MULTI sub-program gives FORWP the capability of predicting A and XPD, by utilizing forward multiple scattering theory which is capable of modeling attenuation and depolarization effects up to 30 GHz [Tsolakis and Stutzman, 1982]. Also the accurate prediction of A at 11.4 GHz indicates that FORWP can provide successful predictions for at least a portion of these higher frequencies.

Further work will need to assess the effect of DSD on the prediction of A at higher frequencies. Also, the modeling of the freezing (melting) layer may prove to be critical at higher frequencies.

5.7.2 Cross Polarization Predictions

FORWP ability to model depolarization effects up to 30 GHz make it a promising model for predicting XPD. According to work conducted by Baptita and McEwan (1985), XPD can be predicted successfully from dual polarized radar measurements.

To predict cross polarization accurately, the freezing layer must be modeled more precisely than it is presently done in this work. The following researchers have studied the profile of precipitation in the freezing layer: Leitao and Watson (1983) and (1984); Martin, Goddard and Cherry (1984); and Dissanayaka, Chandra, and Watson (1983). These researchers indicate that the freezing layer profile for non convective storms can be accurately modeled using dual polarization radar measurements.

Further development of BSCAT is needed to enable the prediction of hydrometeor distributions other than rain. This development of BSCAT has in part been done by Stapor [1984] in an earlier version of BSCAT. Stapor developed the ability to model ice crystals and ice spheres.

Also, the MULTI portion of FORWP must be modified to predict A and XPD from hydrometeors other than rain. This will require the development of forward scattering cross sections for ice crystals and ice spheres.

References

Atlas, D., and C.W. Ulbrich, (1977) "Path- and area-infegrated rain fall measurement by microwave attenuation in the 1-3 cm band," *J. Appl. Meteorol.*, 16, 1322-1331.

Atlas, D., C.W. Ulbrich, and R. Meneghini (1984), "The multiparameter remote measurement of rainfall," *Radio. Sci.*, 19, 49-57.

Atlas, D. and A.C. Chmela (1957), "Physical-Synoptic variations of drop-size parameters", in *Proceedings 6th Weather Radar Conference*, pp. 22-29, American Meteorlogical Society, Boston, Mass.

Baptista and McEwan (1985) "Prediction of Slant-Path Rain Cross Polarisation Discrimination Ratio and Phase Using Dual-Polarisation Radar Data," *Electronics Letters* pp. 460-461, Vol. 21, May.

Beard, K.V., D.B. Johnson, and A.R. Jameson (1983), "Collisional forcing of raindrop oscillations", *J. Atmos. Sci.*, 40, 455-462.

Bringi, V.N., T.A. Seliga, and S.M. Cherry (1983), "Statistical properties of dual-polarization differential reflectivity radar signal," *Trans. Iee Geosci. Remote Sensing*, GE-21(2), 215-220.

Bringi, V.N., S.M. Cherry, M.P.M. Hall, and T.A. Seliga (1978) "A new accuracy in determining rainfall rates and attenuation due to rain by means of dual-polarization measurements," *IEE Conf.* Publication, 169(2), P12C-124.

Cherry, S.M., J.W.F. Goddard, and M.P.M. Hall (1980) "Examination of raindrop sizes using a dual-polarization radar," *Preceedings 19 conference on radar meteorology*, pp. 526-531, American Meteorological Society, Boston, Mass.

Diresheneli, H., T.A. Seliga and K. Aydia (1983) "Differential reflectivity (ZDR) measurements of rain fall compared with ground-based disdrometer measurements," Preprints *21st Conf. on radar Metero.*, AMS, Boston.

Goddard, J.W.F., S.M. Cherry, and V.N. Bringi, (1982), "Comparison of dual-polarization radar measurements of rain with ground based disdrometer measurements," *J. Appl. Meteorol.*, 21, 252-256.

Goddard, W.F., S.M. Cherry (1984), "Quantitative precipitation measurements with dual linear polarisation radar," *22nd Conference on Radar Meteorology*, Zurich, Switzerland, pp. 352-357.

Goddard, J.W.F., and S.M. Cherry (1984), "The ability of dual-polarization radar (copolar linear) to predict rainfall rate and microwave attenuation," *Radio Sci.*, Volume 19, Number 1, January-February.

Jameson, A.R., and K.V. Beard (1982), "Raindrop axial ratios," *J. Appl. Meteorol.*, 21, 257-59.

Leitai, M.J., and P.A. Watson (1984), "Application of Dual Linearly Folarized Radar Data to Prediction of Microwave Path Attenuation,", *Radio Science*, 19(1), pp. 209-220.

Leitao, M.J., P.A. Watson (1983), "A New Method for Prediction of Slant-Path Attenuation at 10-30 GH_z Using Detailed Knowledge of the Micro-Physical Structure of Rainstorms," *ICAP*, pp. 73-78.

Marshall, J.S., and W.M.K. Palmer (1948), "The Distribution of Raindrops with Size," *J. Atmos. Sci.*, 5, 165-166.

Olsen, R.L. (1982), "A Review of Theories of Coherent Radio Wave Propagation Through Precipitation Media of Randomly Oriented Scattering, and the Role of Multiple Scattering," *Radio Science*, 17(5), pp. 913-928.

Pratt, T., and Sweeney, D. (1986), "A Multiple Polarization Radar Experiment to Predict Slant Path Attenuation and Depolarization," Commission F Open Symposium, URSI, Paper 10-2, August 1.

Pruppacher, H.R., and R.L. Pitter (1971), "A Semi-empirical Determination of the Shape of Cloud and Rain-drops," *J. Atmos. Sci.*, 28, pp. 16-94.

Runyon, D.L., and W.L. Stutzman (1983), "A Simple Model for the Depolarizatius Effects of Rain and Ice on Earthspace Limits in the 10 to 30 GH_z frequency range," Interim. Rep. under JPL Contract 955954, June.

Seliga, T.A., V.N. Bringi, and E.A. Mueller (1982), "First Comparisons of rainfall rates derived from radar differential reflectivity and distrometer measurements," *Trans. IEEE Geosci. Remote Sensing*, GE-20(2), 201-204,1.

Stapor, D.P. (1982) "Dual-polarization meteorlogical radar: Theory and Design," M.S. Thesis, Electrical Engineering Department, Virginia Polytechnic Institute and State University, Blacksburg, Virginia, May.

Stapor, D.P. and Pratt, T. (1984), "A Generalized Analysis of Dual-polarization Radar Measurements of Rain," *Radio Science*, Vol. 19, Number 1, pp. 90-98, Jan.-Feb.

Stutzman, W.L. and K.M. Yon (1986), "A simple Rain Attenuation Model for Earth-Space Radio Links Operating at 10-35 GH_z," *Radio Science*, Volume 21, Number 1, pp. 65-72, Jan.-Feb.

Stutzman, W.L. and D.L. Runyon (1984), "The Relationship of Rain-Induced Cross-Polarization Discrimination to Attenuation for IV to 30 GH_z Earth-Space Radio Links," *IEE Transactions on Antennas and Propagation*, Vol. AP-32, No. 7, July.

Stutzman, W.L. and W.K. Dishman (1982), "A simple Model for the Estimation of Rain-Induced Attenuation Along Earth-Space Paths at Millimeter Wavelenghts," *Radio Science*, Volume 17, Number 6, pp. 1465-1479, Nov.-Dec.

Sweeney, D., (1986), "Measurement and Validation of Rainstorm Parameters with the VPI Radar," M.S. Thesis, August, 1986.

Tsolakis, A., and Stutzman, W.L. (1982), "Multiple Scattering of Electromagnetic Waves by Rain," *Radio Science*, 17(6), pp. 1495-1502.

Ulbrich, C.W., (1981), "Effect of Size Distribution Variations on Precipitation Parameters Determined by Dual-Measurement Techniques," *Proceedings 20th Conference on Radar Meteorology*, pp. 276-281, American Meteorological Society, Boston, Mass.

Ulbrich, C.W. and Atlas, D., "Assessment of the Contribution of Differential Polarization to Improved Rainfall Measurements," *Radio Science*, 19(1), 49-97.

Ulbrich, C.W. and Atlas, D. (1977), "A Method for Measuring Precipitaion Parameters Using Radar Reflectivity and Optical Extinction," *Ann. Telecommun.*, 32, pp. 415-471.

The vita has been removed from the scanned document